TECHNICAL UNIVERSITY OF MUNICH

TUM SCHOOL OF NATURAL SCIENCES

DEPARTMENT OF PHYSICS

Bachelor's Thesis in Physics

Study of $K^-\pi^+$ and $\pi^-\pi^+$ Amplitudes in $K^-\pi^-\pi^+$ Data from the COMPASS Experiment

Godo Kurten

TECHNICAL UNIVERSITY OF MUNICH

TUM SCHOOL OF NATURAL SCIENCES

DEPARTMENT OF PHYSICS

Bachelor's Thesis in Physics

Study of $K^-\pi^+$ and $\pi^-\pi^+$ Amplitudes in $K^-\pi^-\pi^+$ Data from the COMPASS Experiment

Analyse von $K^-\pi^+$ und $\pi^-\pi^+$ Amplituden in $K^-\pi^-\pi^+$ Daten vom COMPASS Experiment

Author:	Godo Kurten
1st Examiner and Supervisor:	Prof. Dr. Stephan Paul
2nd Examiner:	Prof. Dr. Lothar Oberauer
Advisor:	Dr. Stefan Wallner
Submission Date:	December 9, 2023
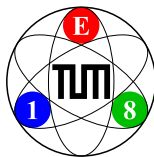
I confirm that this bachelor's thesis in physics is my own work and I have documented all sources and material used.

Munich, December 9, 2023   Godo Kurten

Abstract

The understanding of the strong interaction can be deepened by a complete knowledge of the strange-meson excitation spectrum. Since it is not yet fully known, we analyze the largest $K^- + p \to K^-\pi^-\pi^+ + p$ diffractive scattering data sample to date from the COMPASS experiment.

In a previous analysis of this data sample, resonances appearing in the $K^-\pi^-\pi^+$ final-state have been analyzed with a partial-wave analysis (PWA). A novel approach called the freed-isobar analysis allows us to study in principle also resonances in the $K^-\pi^+$ and $\pi^-\pi^+$ subsystems of the $K^-\pi^-\pi^+$ final-state. We have studied and proved the applicability of the freed-isobar approach to our data sample by measuring well known resonances, such as the $K^*(892)$, $\rho(770)$ and $K_2^*(1430)$. We found potential signals from excited strange-meson states which we cannot clearly assign to a known resonance. We studied the $K^-\pi^+$ subsystem that contains the $K_0^*(700)$ resonance, which shows evidence of not being a pure $q\bar{q}$ state. Due to its unusual shape, multiple parameterizations were compared, and the Palano-Pennington parameterization was determined to perform best. Also, we investigated the applicability of Wilks' theorem to the calculations of the significance of a resonant component. Lastly, we determined possible analysis effects resulting from a final-state particle-identification that does not cover the full kinematic range of the final-state particles.

Contents

1 Introduction

The strong interaction is the force that binds quarks together to form protons, neutrons, or other hadronic particles. The strong interaction is carried by gluons, and acts only on quarks, who cannot be observed individually because of the confinement. The quantum field theory that describes the strong interaction is the quantum chromodynamics (QCD). At high energies, QCD can be solved perturbatively, leading to precise, verified predictions. At low energies, around the mass of hadrons, QCD cannot be solved perturbatively. The measurement of the excitation spectrum of the simplest strongly bound states, called mesons, provides information about QCD at low energies. Mesons consist of a constituent quark-antiquark pair $q\bar{q}$ bound by the strong interaction [1]. Mesons composed of an (anti-)strange and an (anti-)up/down quark are called strange-mesons. Our goal is to measure the strange-meson excitation spectrum and to compare our values with previous measurements listed in the PDG [2].

One of the goals of the hadron spectroscopy program, of the COMPASS experiment, is the measurement of excited strange-mesons via diffractively scattering[1] of a beam of K^- off a liquid hydrogen target. At the high center-of-momentum energy of $19\,\text{GeV}/c^2$ of the beam-target system, the strong interaction scattering process can be effectively modeled in Regge theory by a Pomeron $\mathbb{P}$ exchange [3, 4]. The reaction studied in this analysis is illustrated in fig. 1.1. The incoming K^- beam scatters off the proton, creating an excited intermediate state X^-. The intermediate state decays into the three final-state particles $K^-\pi^-\pi^+$. The decay process is known to be dominated by two-body resonances, so-called isobars, which is why the isobar-model is

(a)   (b)
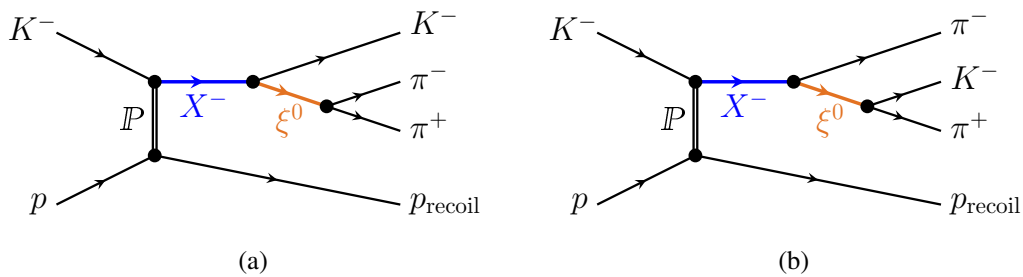
Figure 1.1: Schematic view of the reaction $K^- + p \rightarrow K^-\pi^-\pi^+ + p$ in the isobar-model. In (a) the bachelor particle is the K^- and the isobar ξ^0 decays into $\pi^-\pi^+$. In (b) the bachelor particle is the π^- and the isobar ξ^0 decays into $K^-\pi^+$.

---

[1]Diffractive scattering reactions are of inelastic nature with a comparably low exchange of energy between the beam and target. One or both the hadrons get excited and then dissociate into a multi-particle final-state.

employed. The isobar-model models the decay of the intermediate state X^- in two steps. First, the intermediate state decays into an isobar ξ^0 and a bachelor-particle b^-, which can be either a K^- or a π^-. Then, the isobar decays into the two remaining final-state particles $\pi^- \pi^+$ or $K^- \pi^+$. The target proton remains intact.

The kinematics of the process are given by the center-of-momentum energy s, the invariant mass of the $K^- \pi^- \pi^+$ system $m_{K\pi\pi}$, the invariant masses of the $K^- \pi^+$ and $\pi^- \pi^+$ subsystems $m_{K^- \pi^+}$ and $m_{\pi^- \pi^+}$ (or generally $m_{h^- h^+}$), respectively, and the squared-four-momentum transfer t between the K^- and the proton. Instead of t, the reduced squared four-momentum transfer is used for convenience

$$t' \equiv |t| - |t|_{\min}, \tag{1.1}$$

where $|t|_{\min}$ is the minimum squared four-momentum transfer[2] required to produce an intermediate state X^- of mass $m_{K\pi\pi}$. The dependence of the process on these kinematic factors is analyzed.

To determine the spin J and parity P of the intermediate states, as well as their nominal masses and widths, a Partial-Wave Analysis (PWA) must be performed. We have performed the PWA in two steps. First, in the so-called Partial-Wave Decomposition (PWD) we disentangled the contributions from different partial-waves, that describe the decay chain of a given intermediate state X^- with certain J^P quantum numbers. In the conventional PWD, the amplitudes of the three-body systems are measured. In this work, we employ an extended version of the PWD, the so-called freed-isobar PWD, where in addition the amplitude of the resonances in the isobar subsystems is measured. In the second step called Resonance-Model Fit (RMF), the $m_{h^- h^+}$ dependence of the amplitude is modeled explicitly to extract the mass and width parameters of the appearing meson resonances.

The freed-isobar PWD is a novel method in the PWA. It has already been successfully applied in the analysis of the $\pi^- \pi^- \pi^+$ final-state from the same data taking campaign [6–8]. The data sample of the $\pi^- \pi^- \pi^+$ final-state has about 100 times more measured events than our $K^- \pi^- \pi^+$ data sample. The PWA of the $K^- \pi^- \pi^+$ final-state for three-body states was developed and performed in ref. [5]. We refer to this analysis as the $K^- \pi^- \pi^+$ three-body analysis in the rest of the text. In addition, the freed-isobar PWD for the $[K\pi]_P$, $[\pi\pi]_P$, $[K\pi]_D$ and $[K\pi]_S$ isobar subsystems was performed in ref. [5]. The two letters in the square brackets symbolize the two particles in the subsystem. The subscript of the brackets indicate the angular momentum between the isobar ξ^0 and the bachelor particle b^-. A first few simple studies were already performed in ref. [5]. The $K^- \pi^- \pi^+$ three-body analysis also had to account for higher background contributions than the $\pi^- \pi^- \pi^+$ data sample analysis due to a more demanding identification of the final-state particles. Therefore, methods to deal with the effects of the demanding particle identifications were developed and applied.

In the RMFs, we model meson resonances by resonant components such as a Breit-Wigner amplitude. To determine the statistical significance of such a component, likelihood-ratio hypothesis tests are performed. Since the true Probability Density Function (PDF) of the

---

[2]$|t|_{\min}$ is given in eq. (2.3) in ref. [5].

test statistic is not known, it is approximated by a χ^2-distribution using Wilks' theorem [9]. However, the RMFs violate a precondition of Wilks' theorem. To investigate whether Wilks' theorem still provides a sufficient approximation of the true PDF, we studied the applicability of Wilks' theorem with extensive toy Monte Carlo studies of RMFs.

Due to the small number of events and higher background contributions in the $K^-\pi^-\pi^+$ data sample compared to the $\pi^-\pi^-\pi^+$ data sample, the freed-isobar PWD is more challenging for the $K^-\pi^-\pi^+$ data sample than in the $\pi^-\pi^-\pi^+$ data sample. One of the objectives of this work is to determine whether the freed-isobar method is still applicable to the $K^-\pi^-\pi^+$ data sample, which we studied with an extensive amount of RMFs. With the RMFs we also look for indications of excited states in the four amplitudes. To find out which resonances contribute to our measured amplitudes, the results of the RMFs are compared with previous measurements listed in the PDG [2].

The methods to deal with the demanding particle identification developed for the $K^-\pi^-\pi^+$ three-body analysis cannot be directly applied in the freed-isobar analysis. Therefore, another scope of this work is to determine if and how the background contributions affect the measured amplitude.

In most amplitudes we used a Breit-Wigner component to model resonant signals in our data. In the $[\pi\pi]_P$ and $[K\pi]_S$ amplitudes different parameterizations for the resonant signals are available. For example in the $[K\pi]_S$ amplitude, which contains very broad signals, four parameterizations specifically designed for the $[K\pi]_S$ amplitude are compared. We want to determine the parameterization that gives the best description of the measured $[K\pi]_S$ amplitude up to about $m_{h^-h^+} = 2.2\,\mathrm{GeV}/c^2$.

Chapter 2 discusses the COMPASS experiment setup and the event selection. In chapter 3, we discuss the concept of the partial-wave decomposition and the caveats, resulting from the demanding particle identification. Chapter 4 explains the resonance-model fits. In chapter 5, we discuss the calculation of the statistical significance of resonant components in the RMF. To this end, we show extensive toy Monte Carlo studies of the applicability of Wilks' theorem for the significance calculation. In chapter 6, we show and discuss the results obtained in the RMFs of the four subsystems we studied. In chapter 7, the results are concluded and an outlook to further possible analysis steps is given.

2 Strange-Meson Spectroscopy

2.1 COMPASS Experiment

The data for this analysis were collected in 2008 and 2009 as part of the hadron spectroscopy program at the COMPASS experiment (COmmon Muon Proton Apparatus for Structure and Spectroscopy). COMPASS has measured an unprecedented amount of data in high-energy π^- and K^- diffractive scattering allowing high precision spectroscopy of light mesons. A brief description of the COMPASS experimental setup is given below. A more detailed description can be found in refs. [10, 11].

Figure 2.1 shows the COMPASS fixed-target experiment setup. COMPASS is located at CERN's M2 beam. Protons from the Super Proton Synchrotron (SPS), with a momentum of about $400\,\mathrm{GeV}/c$, are impinging a beryllium production target (not shown), producing a shower of secondary hadrons, such as pions, kaons and (anti-)protons. From these, a negative hadron beam at about $190\,\mathrm{GeV}/c$ is selected using magnets and collimators along the M2 beamline. To separate the kaons from the other hadrons, two CEDAR detectors (ChErenkov Differential counters with Achromatic Ring focus) are placed about $30\,\mathrm{m}$ upstream of the COMPASS target.
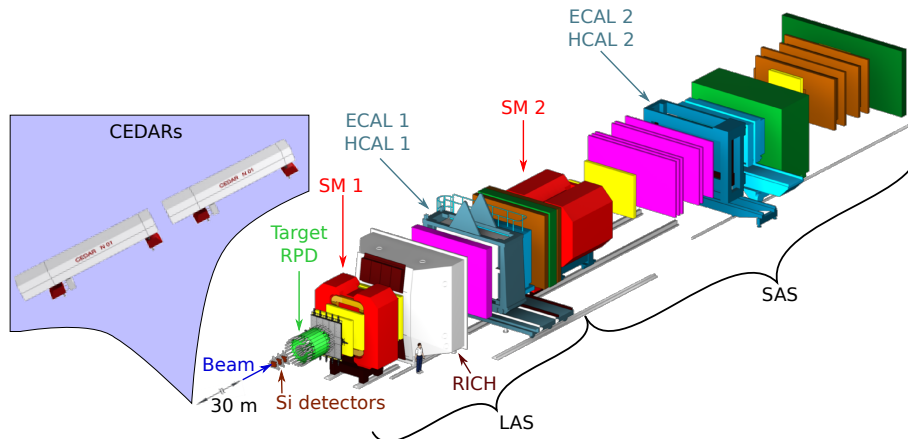
Figure 2.1: Schematic representation of the COMPASS experiment. The hadron beam passes two CEDAR detectors before hitting the recoil-proton detector (RPD). The final-state particles are then measured by a Large-Angle (LAS) and a Small-Angle (SAS) magnetic spectrometer. Both spectrometers consist of an array of detectors shown in different colors. The figure is taken from ref. [5] and adapted from ref. [10].

The negative kaon beam then hits the cylindrical liquid hydrogen target. High-precision silicon microstrip detectors are used to measure the hadron beam and final-state particles both upstream and downstream of the target, respectively. This enables the precise reconstruction of the interaction point between the beam particle and the target proton. Downstream of the silicon microstrip detectors, two detector sections measure the momenta of the final-state particles produced in the reaction. The first section is the Large-Angle magnetic spectrometer (LAS). The LAS is built around the SM1 dipole magnet and detects particles with a polar angle of ±180 mrad with respect to the beam axis. The second section is the Small-Angle magnetic spectrometer (SAS), which is built around the stronger SM2 dipole magnet. It detects particles with a polar angle of ±30 mrad extending the precision of the spectrometers in this region. The SAS can therefore detect particles with higher momentum. Both sections are equipped with different types of detectors, such as Gas Electron Multipliers (GEM), micromesh gaseous structure detectors (microgems), Scintillating Fibre counters (SciFi), Drift Chambers (DC) and Multi-Wire Proportional Chambers (MWPC), which measure the position of the final state particles. The species of the final-state particles is identified by a Ring-Imaging CHerenkov detector (RICH). The Electromagnetic (ECAL) and Hadronic (HCAL) CALorimeter, which measure the energy of the particles, were not used in this analysis.

2.2 Event Selection

During the 2008 and 2009 data taking campaigns COMPASS recorded a total of approximately 13.4 billion events [5]. A number of data cuts were performed to select only those events of the reaction $K^- + p \rightarrow K^- \pi^- \pi^+ + p$. The event selection process is inspired by refs. [12, 13], but was refined for the three-body analysis [5]. A more detailed description of the data selection
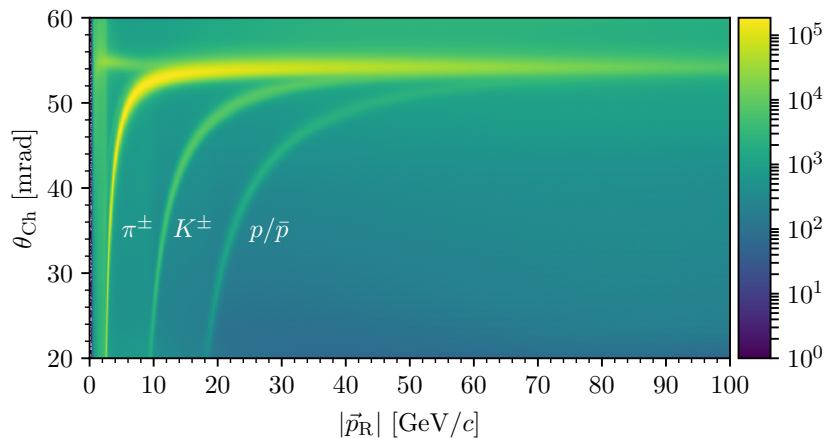
Figure 2.2: Distribution of Cherenkov angles as a function of the final-state particle momentum $|\vec{p}_R|$. Figure taken from [5].
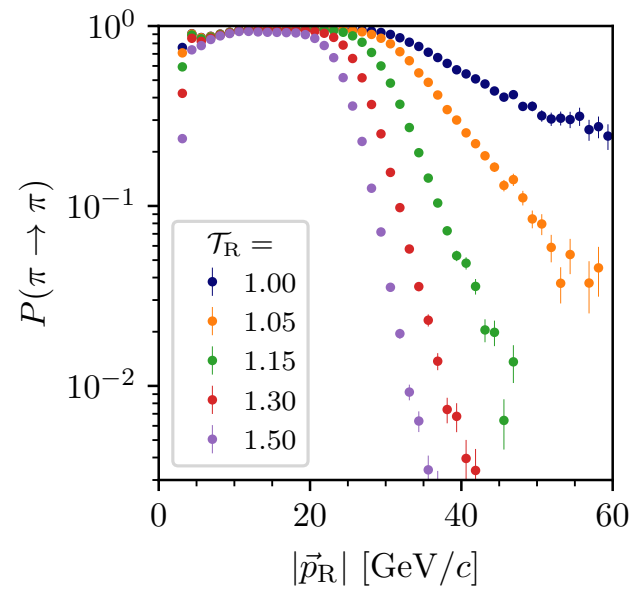
Figure 2.3: RICH efficiency to identify a π^- as a function of the momentum. For this analysis only the green data points with $\mathcal{T}_R = 1.15$ are of interest. Figure taken from ref. [5].
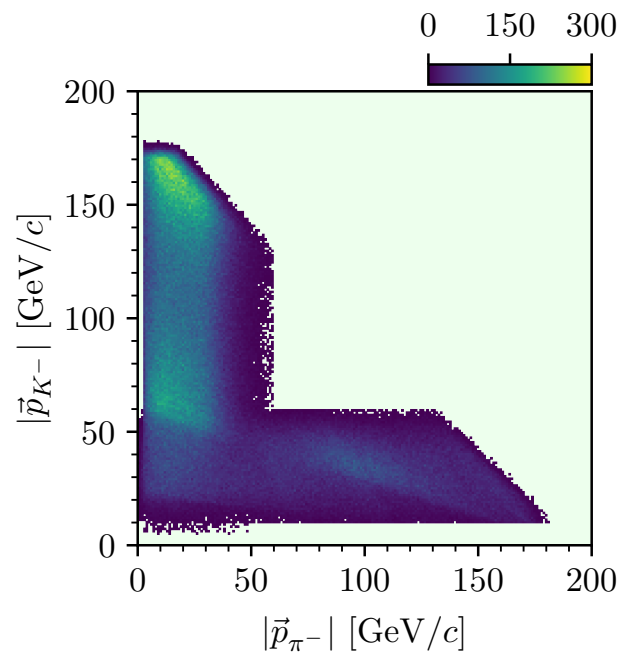
Figure 2.4: Distribution of the momenta of the identified π^- and K^-. The figure is taken from ref. [5].

process for this analysis can be found in ref. [5] and is summarized in the following. First, we require the event to contain three charged final-state particles, and a single interaction vertex of the beam particle and the target proton in the target region. Then, we require that the CEDAR detectors identified the beam particle as a kaon.

The species of the three final-state particles must also be identified, for which the RICH detector is used for. The measurement of the emission angle of the Cherenkov light produced when a particles passes through the RICH detector, together with the measured particle momentum, allows the particle species to be identified. At increasing momenta of the final-state particles the distinction between kaons and pions becomes increasingly difficult, because the Cherenkov angles of kaons and pions become more similar. Figure 2.2 illustrates this effect. Figure 2.3 shows the efficiency[1] of correctly identifying pions as determined in ref. [5]. The efficiency is high up to about $30\,\mathrm{GeV}/c$, where the efficiency drops. For particles with momenta above $40\,\mathrm{GeV}/c$ the efficiency is nearly zero. Thus, pions with momenta over $40\,\mathrm{GeV}/c$ are not differentiable from other particles. Since the final-state particles have momenta up to $190\,\mathrm{GeV}/c$, this leaves a blind spot in the phase-space distribution of the particles as illustrated in fig. 2.4, by the $|\vec{p}_{\pi^-}| \gtrsim 60\,\mathrm{GeV}/c$, $|\vec{p}_{K^-}| \gtrsim 60\,\mathrm{GeV}/c$ square where no pions and kaons were identified.

We also require energy and momentum conservation by comparing the measured energy sum and momenta of the final-state particle to the known initial state kinematics. This suppresses events with at least one extra final-state particles that was not measured. Finally, we made cuts
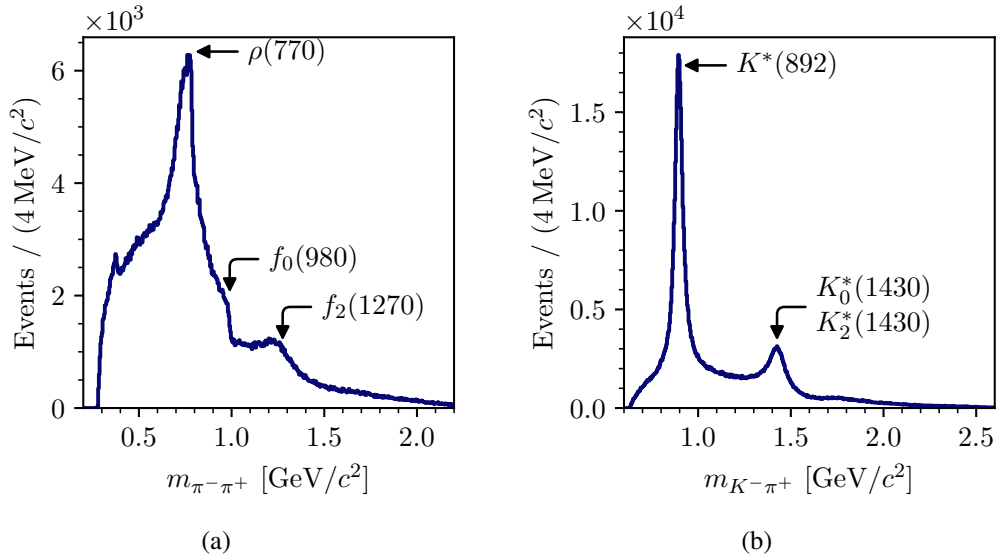
Figure 2.5: Invariant mass spectra of the $\pi^-\pi^+$ (a) and $K^-\pi^+$ (b) subsystems in the $K^-\pi^-\pi^+$ final-state. The arrows indicate well known resonances in the spectra according to the PDG [2].

---

[1] $\mathscr{T}_R$ refers to the RICH threshold for the particle identification decision.

on the kinematic region of interest, i.e. $0.1 \leq t' < 1.0 \, (\text{GeV}/c)^2$ and $1.0 \leq m_{K\pi\pi} < 3.0 \, \text{GeV}/c^2$. After all these cuts, a data set of about 720,000 events was obtained. This work deals with the resonances in the $K^-\pi^+$ and $\pi^-\pi^+$ subsystems of the process $K^- + p \rightarrow K^-\pi^-\pi^+ + p$. The invariant mass spectra of these two subsystems are shown in fig. 2.5, which also show the isobar resonances that could contribute to the spectra. In order to disentangle the resonant structure of the subsystems, a freed-isobar partial-wave analysis was performed. The formalism of the freed-isobar partial-wave analysis is discussed in chapters 3 and 4. The results are discussed in chapter 6.

3 Partial-Wave-Decomposition

Figure 3.1 shows the reaction $K^- + p \rightarrow K^- \pi^- \pi^+ + p$ in the isobar model [14, 15], where the intermediate state X^-, with spin J, parity P and spin projection M^ε, first decays into a bachelor particle b^-, either a K^- or a π^-, and an isobar resonance ξ^0 with spin J_ξ and helicity λ_ξ. L denotes the angular momentum between the bachelor particle b^- and the isobar ξ^0. Then the isobar ξ^0 decays into the two final-state particles $h^- h^+$, which can be $\pi^- \pi^+$ or $K^- \pi^+$. In order to extract the resonances and measure their J^P quantum numbers a Partial-Wave Analysis (PWA) was performed. We took a two-step approach to the PWA. The first step is called the Partial-Wave Decomposition (PWD), where the dependence of t', $m_{K\pi\pi}$ and $m_{h^- h^+}$ is not modeled explicitly, but the amplitudes is measured independently in narrow t' and $m_{K\pi\pi}$ bins. In the second step, called Resonance-Model Fit (RMF), the goal is to extract the isobar resonances with their resonance components, as discussed in chapter 4. Therefore, the $m_{h^- h^+}$ dependence is modeled explicitly.

In the conventional PWD, discussed in section 3.1, the data are decomposed into contributions from various partial-waves, which are given by the quantum numbers $J^P M^\varepsilon$ of the intermediate state X^-, and their decay path given by the isobar resonance ξ^0, the bachelor particle b^- and the relative orbital angular momentum L between the bachelor particle and the isobar. The name of a partial-wave is given by its partial-wave-label:

$$a = J^P M^\varepsilon \xi b L. \tag{3.1}$$

To measure the amplitude of the isobar-systems, a so-called freed-isobar PWD was performed, as discussed in section 3.2. Both the conventional and the freed-isobar PWD were performed in ref. [5]. A more detailed explanation of the PWD used in this analysis can be found there.
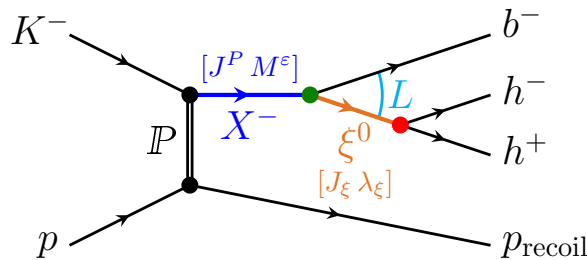
Figure 3.1: Schematic view of the reaction $K^- + p \rightarrow K^- \pi^- \pi^+$ in the isobar model, where an intermediate state X^- decays into the $K^- \pi^- \pi^+$ final-state via an isobar ξ^0.

3.1 Conventional Partial-Wave-Decomposition

The reaction $K^- + p \rightarrow X^- + p$ is characterized by the center-of-momentum energy s of the beam K^- and the target proton system, the reduced squared four-momentum transfer t' (see eq. (1.1)) and the invariant mass $m_{K\pi\pi}$ of the $K^-\pi^-\pi^+$ system. The decay of the intermediate state X^- at fixed $m_{K\pi\pi}$ is described by five phase-space variables, the angular dependence of the X^--decay Ω_X, the angular dependence of the isobar decay Ω_ξ and the invariant two-body mass $m_{h^-h^+}$, which are summarized by τ. The total measured intensity distribution is modeled by:

$$\mathcal{I}(\tau, m_{K\pi\pi}, t') = \left| \sum_{a \in \mathbb{W}(m_{K\pi\pi}, t')} \mathcal{T}_a(m_{K\pi\pi}, t') \Psi_a(\tau, m_{K\pi\pi}) \right|^2, \tag{3.2}$$

which is the number of counts as a function of the kinematic variables. The model intensity sums the amplitudes of the partial-waves included in the considered set of waves $\mathbb{W}$[1]. Assuming factorization of the production and decay of the X^- system, we model these amplitudes as a product of transition amplitudes $\mathcal{T}_a(m_{K\pi\pi}, t')$, modeling the production and propagation of X^-, and decay amplitudes $\Psi_a(\tau, m_{K\pi\pi})$, which model the decay of X^-.

Decay Amplitude

The decay amplitude can be written as

$$\Psi_a(\tau, m_{K\pi\pi}) = \frac{\tilde{\Psi}_a(\tau, m_{K\pi\pi})}{\sqrt{\Re_a(m_{K\pi\pi})}}, \tag{3.3}$$

where $\Re_a(m_{K\pi\pi})$ is the normalization integral:

$$\Re_a(m_{K\pi\pi}) = \int\limits_{(m_{K\pi\pi}, t')} \mathrm{d}\tilde{m}_{K\pi\pi} \mathrm{d}\tilde{t}' \int \mathrm{d}\Phi_3(\tau) \left| \tilde{\Psi}_a(\tau, m_{K\pi\pi}) \right|^2, \tag{3.4}$$

where the squared absolute value of $\tilde{\Psi}_a$ is integrated over a $(m_{K\pi\pi}, t')$ cell and the phase-space Φ_3. The total decay amplitude:

$$\tilde{\Psi}_a(\tau, m_{K\pi\pi}) = \mathcal{Z}(\Omega_X, \Omega_\xi) \Delta(m_{h^-h^+}, m_{K\pi\pi}), \tag{3.5}$$

is written as a product of two parts: $\mathcal{Z}$ describes the angular dependence of the decay amplitude, Δ describes the dependence on the invariant two-body mass $m_{K^-\pi^+}$ or $m_{\pi^-\pi^+}$ [16]. This term is from a product

$$\Delta(m_{h^-h^+}, m_{K\pi\pi}) = \mathcal{D}_\xi(m_{h^-h^+}) F_L(m_{K\pi\pi}) F_{J_\xi}(m_{h^-h^+}), \tag{3.6}$$

of two parts: (i) a dynamic amplitude $\mathcal{D}_\xi$, which encodes the amplitude of an isobar resonance; and (ii) centrifugal-barrier factors $F_{L/J_\xi}(m_{K\pi\pi}/m_{h^-h^+})$, which account for the energy required to produce an orbital angular momentum L/J_ξ. For $F_{L/J_\xi}(m_{K\pi\pi}/m_{h^-h^+})$ the parameterization of von Hippel and Quigg was used [17].

---

[1] The set of considered partial-waves was determined in a so-called wave-set selection fit. The method and its results can be found in chapter 5.2 of ref. [5].

To model the decay amplitude, the dynamic amplitude $\mathcal{D}_\xi$ must be explicitly parameterized. For the dynamic amplitude at most isobars, a relativistic Breit-Wigner amplitude is used [4, 18]:

$$\mathcal{D}_{BW}(m) = \frac{m_0 \Gamma_0}{m_0^2 - m^2 - im_0\Gamma(m)},\qquad(3.7)$$

where m_0 and Γ_0 refer to the nominal mass and width of the resonance, respectively. The dynamic width $\Gamma(m)$ is given by:

$$\Gamma(m) = \Gamma_0 \frac{m_0}{\sqrt{m^2}} \frac{q(m)}{q(m_0)} \frac{F_{L_\xi}(Rq(m))}{F_{L_\xi}(Rq(m_0))},\qquad(3.8)$$

where $q(m)$ is the two-body break-up momentum[2]

$$q(m, m_1, m_2) = \frac{\lambda^{1/2}(m^2, m_1^2, m_2^2)}{2m},\qquad(3.9)$$

with m_1 and m_2 being the masses of the daughter particles. Finally, $F_L(Rq(m^2))$ is the Hippel-Quigg [17] angular-momentum barrier factor, where R is the momentum scale parameter related to the potential radius, that defines the angular-momentum barrier. $L = J_\xi$ for decays of two pseudoscalars.

Not all resonances are well approximated by the Breit-Wigner amplitude. In our analysis the $f_0(980)$ is parameterized by the so-called Flatté parameterization [19] with formulas and parameters determined in ref. [20]. The so-called broad $[\pi\pi]_S$ amplitude, which is dominated by the $f_0(500)$, is parameterized with an ansatz proposed by the VES collaboration [21], with parameters determined from $\pi\pi \to \pi\pi$ scattering data [22]. The $[K\pi]_S$ amplitude is parameterized by the so-called Palano-Pennington parameterization, which is discussed in section 6.4.3.

With these parameterizations, the decay amplitudes in the isobar model are known and contain no free parameters. A more detailed description of the decay amplitude used in the three-body analysis can be found in ref. [5].

Transition Amplitude

The transition amplitudes are independent of τ, unknown, and binned into narrow $(m_{K\pi\pi}, t')$ cells, that were chosen to be narrow enough that the transition amplitude can be assumed to be constant within a $(m_{K\pi\pi}, t')$ cell. This means that the transition amplitude is parameterized by step-wise constant functions, which allows the measurement of the transition amplitudes to be without model dependence.

The $m_{K\pi\pi}$ bins have a width of $20\,\mathrm{MeV}/c^2$ for $m_{K\pi\pi} < 2.0\,\mathrm{GeV}/c^2$ and $40\,\mathrm{MeV}/c^2$ for $m_{K\pi\pi} > 2.0\,\mathrm{GeV}/c^2$. The borders of the four t' bins are summarized in table 3.1.

---

[2]λ is the Källèn function.

Fit Procedure

The intensity model is proportional to the product of the probabilities of an event. This allows to formulate a likelihood function that also takes into account various acceptance effects that deform the measured distribution of events. An extended maximum likelihood function is then formulated, which is fit to the data.

3.2 Freed-Isobar Partial-Wave-Decomposition

To extract the amplitude of the isobar systems, a freed-isobar PWD was performed in ref. [5]. This section gives only a brief introduction to the freed-isobar PWD. A more detailed

Table 3.1: Borders of the four t' bins used in the PWD fit. Taken from ref. [5]

$[(\mathrm{GeV}/c)^2]$	0.10	0.15	0.24	0.34	1.00
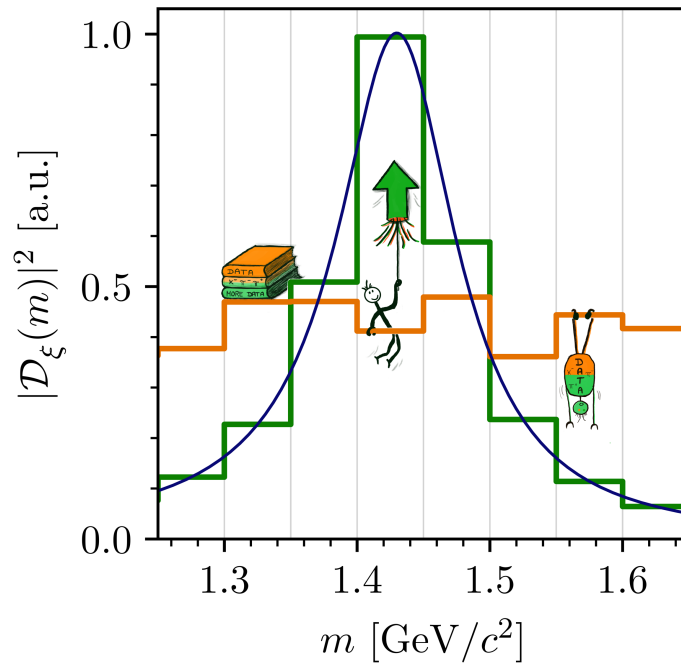
Figure 3.2: Schematic illustration of the freed-isobar PWD fit. The blue curve shows a Breit-Wigner amplitude in an isobar. The orange line represents the piecewise constant function before the freed-isobar PWD fit is performed. The green curve represents the fitted amplitude of the isobar system, which describes the Breit-Wigner amplitude in the isobar. The figure is taken from ref. [5].

explanation can be found in refs. [6, 7, 12]. The ansatz of the conventional PWD requires fixed parameterizations for the dynamic amplitudes. In contrast to the angular dependence of the decay amplitudes, which is known a priori, the dynamic amplitudes must be parameterized explicitly and may therefore introduce a bias from the choice of the used parameterization. The goal of the freed-isobar PWD is to measure this amplitude without the need for any model dependence, hence the same approach is taken for the isobars as for the X^-. To this end, the fixed parameterization (blue curve in fig. 3.2) of a dynamic amplitude (see eq. (3.5)) is replaced by piecewise constant functions (orange lines in fig. 3.2):

$$\mathcal{D}_\xi^{\text{free}}(m_{h^-h^+}) = \sum_i \mathcal{D}_\xi^{\text{free}}(m_{h^-h^+}^i)\Theta(m_{h^-h^+}; m_{h^-h^+}^i), \tag{3.10}$$

where the entire $m_{h^-h^+}$ range is binned into narrow bins $m_{h^-h^+}^i$. The choices of $m_{h^-h^+}$ bin widths are summarized in section 3.2.1. Similar to the conventional PWD, an intensity model of the form

$$\mathcal{I}^{\text{free}}(\tau, m_{K\pi\pi}, t') = \left| \sum_{a,i} \mathcal{T}_{a,i}(m_{K\pi\pi}, t')\Psi_{a,i}(\tau, m_{K\pi\pi}) \right|^2 \tag{3.11}$$

is formulated. The decay amplitude $\Psi_{a,i}(\tau, m_{K\pi\pi})$ is the normalized total decay amplitude $\tilde{\Psi}_{a,i}(\tau, m_{K\pi\pi})$, which is defined analogously to eq. (3.5), where the dynamic amplitude in eq. (3.6) is exchanged by the free amplitude in eq. (3.10). The normalization is given by:

$$\mathfrak{R}_a(m_{K\pi\pi}; m_{h^-h^+}^i) = \int\limits_{(m_{K\pi\pi}, t')} \mathrm{d}\tilde{m}_{K\pi\pi}\mathrm{d}\tilde{t}' \int \mathrm{d}\Phi_3(\tau) \left| \frac{\tilde{\Psi}_a(\tau, \tilde{m}_{K\pi\pi}; m_{h^-h^+}^i)}{\mathcal{D}_\xi^{\text{free}}(m_{h^-h^+}^i)} \right|^2. \tag{3.12}$$

It is important to note that the freed-isobar transition amplitudes $\mathcal{T}_{a,i}$

$$\mathcal{T}_{a,i}(m_{K\pi\pi}, t') \propto \mathcal{T}_a(m_{K\pi\pi}, t')\mathcal{D}_\xi^{\text{free}}(m_{h^-h^+}) \tag{3.13}$$

are a product of the $\mathcal{T}_a$ of the X^- and the freed dynamic amplitude $\mathcal{D}_\xi^{\text{free}}$ and is proportional[3] to the conventional transition amplitudes. Therefore, the transition amplitudes also depend on the mass $m_{h^-h^+}$ of the two-body system and models its $m_{h^-h^+}$ mass dependence for fixed $m_{K\pi\pi}$ and t'. The intensity model is very similar to the intensity model in the conventional PWD. Thus the freed-isobar intensity model is fitted with respect to the freed-isobar transition amplitudes $\mathcal{T}_{a,i}$ (green line in fig. 3.2), by an extended log-likelihood formalism.

Unlike in the conventional PWD, where the amplitudes in different ($m_{K\pi\pi}$, t') cells do not interfere, in the freed-isobar PWD, interference between subsystems is possible at given $m_{h^-h^+}$. For example, the $K^-\pi^+$ subsystem at a given $m_{K^-\pi^+}$ interferes with the $\pi^-\pi^+$ subsystem at all $m_{\pi^-\pi^+}$, since fixing the $m_{K^-\pi^+}$ does not fix the $m_{\pi^-\pi^+}$. This is also true for the $\pi^-\pi^+$ and $K^-\pi^+$ subsystems at fixed $m_{K^-\pi^+}$. This means that we measure the absolute $m_{h^-h^+}$ dependence of the amplitude, i.e. the phase dependence, and not just the relative phase, as in the conventional PWD of the three-body system. For more details on the freed-isobar PWD and how the fit was performed, see ef. [5].

In this analysis only a single partial-wave was freed per freed-isobar PWD, because the freed-isobar PWD introduces many additional parameters to the PWD fit. Freeing multiple

---

[3]Up to the normalization integral. For the full proportionality see eq. F.7 in ref. [5]

partial-waves in one freed-isobar PWD fit introduces too many free parameters to be determined by our limited amount of data. The freed-isobar PWD fit was performed in four subsystems, the $[K\pi]_P$, $[\pi\pi]_P$, $[K\pi]_D$, and $[K\pi]_S$. Each subsystem is defined by the two particles into which the subsystem decays and the orbital angular momentum between the two exiting particles, denoted by the subscript letter.

3.2.1 Bin Widths

Table 3.2 lists the bin widths for the $m_{h^-h^+}$ two-body mass in the freed-isobar PWD. The lowest and highest bins are always slightly wider than the other bins to accommodate the full $m_{h^-h^+}$ spectrum. The lower limit of the mass bins is given by the phase-space barrier, i.e. the minimum $m_{h^-h^+}$ that can decay to $K^-\pi^+$ or $\pi^-\pi^+$. It is given by $m_{\min} = m_{K^-/\pi^-} + m_{\pi^+}$. The upper limit is given by the highest $m_{h^-h^+}$ we can observe in the highest $m_{K\pi\pi}$ bin, i.e. $m_{\max} = 3.0\,\mathrm{GeV}/c^2 - m_{K^-/\pi^-}$.

3.2.2 Zero Modes

The amplitude measured with the freed-isobar PWD is not well defined and mathematical ambiguities may arise, the so-called zero modes. We will only briefly introduce zero modes. A more detailed description can be found in ref. [7]. There may exist $\mathcal{T}_{a,i}$ and $\tilde{\mathcal{T}}_{a,i}$ such that both yield the same model intensity, i.e.

$$\sum_{a,i} \mathcal{T}_{a,i}(m_{K\pi\pi}t')\Psi_{a,i}(\tau, m_{K\pi\pi}) = \sum_{a,i} \tilde{\mathcal{T}}^z_{a,i}(m_{K\pi\pi}, t')\Psi_{a,i}(\tau, m_{K\pi\pi}), \qquad (3.14)$$

where $\tilde{\mathcal{T}}_{a,i} = \mathcal{T}_{a,i} + \Delta\mathcal{T}$. The $\Delta\mathcal{T}$ is responsible for the ambiguities and is called zero-mode. Typically, the ambiguities can only occur if at least two waves are freed. Then the zero mode in one wave is figuratively compensated by a zero-mode in the other wave. Therefore, the mathematical ambiguity can be avoided by fixing the amplitude of one wave, since this also fixes the zero-mode and thereby the amplitude in the other wave. Since only one amplitude was freed in each freed-isobar PWD fits, in this work no zero modes are expected in our results.

3.3 Limitations of Our Data Sample

In section 2.2, we discussed the limitations in identifying the final-state particles, which leads to about 10 % of background data. In the three-body analysis, this background was accounted for by additional parameters in the conventional PWD [5]. This is not possible in the freed-isobar analysis, because the fit would have too many parameters to be determined by the data. This leads to overfitting and the fit results do not represent the reality.

Table 3.2: Summary of the $m_{h^-h^+}$ two-body mass bin widths in the freed-isobar PWD for **a** the $[K\pi]_P$, **b** the $[\pi\pi]_P$, **c** the $[K\pi]_D$ and **d** the $[K\pi]_S$ amplitudes. Both $m_{\min}$ and $m_{\max}$ are rounded to three decimal places. Section 3.2.1 explains the reason why the lowest and highest bins are wider. Table adapted from ref. [5].

(a) $[K\pi]_P$

$m_{K^-\pi^+}$ Range	$m_{K^-\pi^+}$ Bin width
$\{0.633; 0.800\,\text{GeV}/c^2\}$	$20\,\text{MeV}/c^2$
$\{0.800; 1.000\,\text{GeV}/c^2\}$	$10\,\text{MeV}/c^2$
$\{1.000; 1.720\,\text{GeV}/c^2\}$	$20\,\text{MeV}/c^2$
$\{1.720; 2.861\,\text{GeV}/c^2\}$	$40\,\text{MeV}/c^2$

(b) $[\pi\pi]_P$

$m_{\pi^-\pi^+}$ Range	$m_{\pi^-\pi^+}$ Bin width
$\{0.279; 0.640\,\text{GeV}/c^2\}$	$40\,\text{MeV}/c^2$
$\{0.640; 0.920\,\text{GeV}/c^2\}$	$20\,\text{MeV}/c^2$
$\{0.920; 2.506\,\text{GeV}/c^2\}$	$40\,\text{MeV}/c^2$

(c) $[K\pi]_D$

$m_{K^-\pi^+}$ Range	$m_{K^-\pi^+}$ Bin width
$\{0.633; 1.120\,\text{GeV}/c^2\}$	$40\,\text{MeV}/c^2$
$\{1.120; 1.720\,\text{GeV}/c^2\}$	$20\,\text{MeV}/c^2$
$\{1.720; 2.861\,\text{GeV}/c^2\}$	$40\,\text{MeV}/c^2$

(d) $[K\pi]_S$

$m_{K^-\pi^+}$ Range	$m_{K^-\pi^+}$ Bin width
$\{0.633; 2.861\,\text{GeV}/c^2\}$	$40\,\text{MeV}/c^2$

Another analysis artifact in the three-body analysis is the so-called leakage-effect. Partial-waves affected by the leakage-effect show analysis artifacts in the form of an artificial intensity at $m_{K\pi\pi} \lesssim 1.6\,\text{GeV}/c^2$. The leakage artifacts occur due to the RICH detector not covering the full momentum range of the final-state particles, as mentioned in section 2.2.

As discussed in section 3.2.2, zero-modes are mathematical ambiguities of the measured amplitude. The mathematical ambiguity can be resolved by fixing the amplitude of one partial-wave, since then the ambiguity is avoided as the partner amplitude gets a fixed shape. If the chosen parameterization for the fixed amplitude is not a good representation of the subsystem, this may lead to deformations in the measured amplitude, and thus analysis artifacts. These effects are by definition no zero-modes, since they do not represent a mathematical ambiguity. We will refer to these effects as zero-mode-like effects. It is still unclear if and how these possible analysis artifacts appear in this analysis. One of the objectives of this work is to investigate the effects by these possible analysis artifacts as discussed in chapter 6.

4 Resonance-Model Fit

As discussed in chapter 3, in the first step of the PWA, the amplitude of an isobar system with given quantum numbers was measured in narrow bins of $m_{K\pi\pi}$ and t' using the freed-isobar PWD fit. The goal of the second step of the PWA, the Resonance-Model Fit (RMF), is to identify and measure the mesonic resonances that appear in the freed-isobar amplitudes. To this end, the $m_{h^-h^+}$ dependence of the freed-isobar amplitude is modeled explicitly. In addition, all four t' bins and a selected range of $m_{K\pi\pi}$ bins are fitted simultaneously in an RMF, to provide as much data as possible for the fit. Also, we include only a limited $m_{h^-h^+}$ range in the fit, in order to study only the signals of interest, e.g. the ground-state resonance, while higher excited resonances are excluded from the fit. We use the implementation of the RMF formalism as used in ref. [5].

4.1 RMF Formalism

To identify the resonances that occur in the two-body systems, the $m_{h^-h^+}$ dependence of the measured amplitude of a two-body system must be modeled by the RMF. Therefore, we constructed a model[1] of the form:

$$\hat{\mathcal{T}}(m_{K\pi\pi}, t'; m_{h^-h^+}^i) = \sqrt{\mathfrak{R}(m_{K\pi\pi}; m_{h^-h^+}^i) m_{K\pi\pi}} \, \mathcal{P}(m_{K\pi\pi}, t') \sum_{k\in\mathbb{S}} {}^k C(m_{K\pi\pi}, t') \mathcal{D}_k(m_{h^-h^+}^i; \zeta_k),$$

(4.1)

i.e. as a coherent sum over model components k, which we assume to contribute to the modeled amplitude. The two terms $\mathfrak{R}$ and $\mathcal{P}$ describe the kinematic effects. $\mathfrak{R}$ is the wave-normalization integral defined in eq. (3.12), and contains the centrifugal barrier factors and therefore depends on $m_{h^-h^+}$. The factor $\mathcal{P}$ encodes the production factor[2], which does not depend on $m_{h^-h^+}$. The factor $\mathcal{D}$ is the dynamic amplitude of the model component. It depends on the invariant two-body mass $m_{h^-h^+}$ and the shape parameters ζ. Depending on the parameterization used for the dynamic amplitude, the shape parameters ζ can consist, e.g. for a Breit-Wigner amplitude of the nominal mass m_0 and the nominal width Γ_0 of the resonance, which is modeled by component k. The coupling parameter C encodes the strength and phase with which a model component appears in the total amplitude. There is a coupling for each ($m_{K\pi\pi}$, t') cell. Hence, we do not model the ($m_{K\pi\pi}$, t') dependence, but measure the piecewise-constant Coupling.

---

[1]The partial-wave label a has been dropped for simplicity, because only one partial-wave was freed per freed-isobar PWD.

[2]The production factor is an effective model of the of the scattering process via Pomeron exchange (see eq. (6.12) in ref. [5]).

4.2 Dynamic Amplitudes

As discussed in section 4.1, the model contains a sum over model components k, that we assume contribute to the modeled amplitude. Each component k is modeled by, among others, the dynamic amplitude. In this work, we have most often used the Breit-Wigner amplitude as the dynamic amplitude (see section 3.1). Parameterizations for special cases are discussed in sections 6.2 and 6.4.

So far we have introduced some dynamic amplitudes. All these dynamic amplitudes model only resonant contributions, but the final-state particles can also be produced without a decay via an isobar ξ^0, e.g. a direct decay of the intermediate state X^- into the final-state particles $K^-\pi^-\pi^+$. This process is called the nonresonant production of the final-state particles. In order to take these contributions into account, a so-called nonresonant component can be added as a dynamic amplitude in the RMF model. There are many different nonresonant processes that can contribute, and there is no generally accepted theory model that parameterizes these contributions. Therefore, an effective parameterization with a flexible shape is used. This parameterization is inspired by ref. [23] and was implemented in previous COMPASS $\pi^-\pi^-\pi^+$ analyses [24, 25]. The parameterization for nonresonant contributions reads:

$$\mathcal{D}_{NR}(q;b) = \exp(-bq(m_{h^-h^+})), \tag{4.2}$$

where q is the two-body break-up momentum (see eq. (3.9)) of the two-body isobar system and b is a shape parameter. The shape parameter b controls the dampening of the amplitude towards higher $m_{h^-h^+}$.

Figure 4.1 outlines the color scheme used in the modeled amplitude plots as an example in an intensity plot, i.e., the squared absolute value of the amplitude as a function of $m_{K^-\pi^+}$. The top right corner shows the subsystem in which the RMF was performed in. Below that is the $(m_{K\pi\pi}, t')$ cell. In the plot itself, the measured amplitude is shown by the blue data points. All components describing resonant contributions are shown as a blue curve. The component describing the nonresonant contribution is shown as a green curve. The model amplitude, which is the sum over all resonant and nonresonant components, is shown as a red curve.

4.3 χ^2 Formalism

The model in eq. (4.1) is fitted to the measured amplitude from the freed-isobar PWD in a χ^2 optimization. There, the modeled amplitude $\hat{\mathcal{T}}$ is directly compared to the measured amplitude $\mathcal{T}$. To this end, the vector $\vec{\mu}$ of the measured freed-isobar amplitude values is constructed. Its elements,

$$\mu_j(m_{K\pi\pi}, t') = \begin{cases} \Re(\mathcal{T}(m_{K\pi\pi}; m_{h^-h^+}^{\lceil j/2 \rceil})) & \text{,if } j \text{ is even} \\ \Im(\mathcal{T}(m_{K\pi\pi}; m_{h^-h^+}^{\lceil j/2 \rceil})) & \text{,if } j \text{ is odd}, \end{cases} \tag{4.3}$$

are the real and imaginary parts of the measured amplitude in different $m_{h^-h^+}$ bins. For example, elements one and two correspond to the real and imaginary parts of the first $m_{h^-h^+}$ bin, respectively, and elements two and three correspond to the real and imaginary parts of the
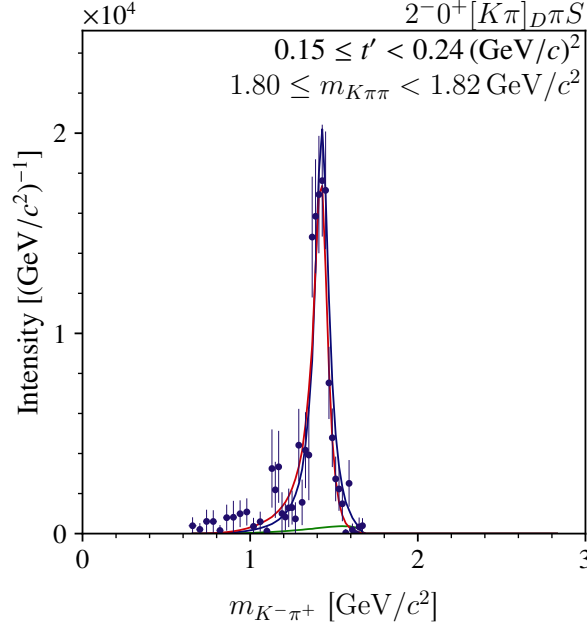
Figure 4.1: Exemplary intensity spectrum of an RMF in the $[K\pi]_D$ subsystem at $m_{K\pi\pi} \approx$ 1.71 GeV/c^2 in the lowest t' bin. The results of the freed-isobar PWD are shown as blue data points. The blue curve represents the resonant component of the RMF. The green curve represents the nonresonant component in the RMF. The red curve represents the model curve.

second $m_{h^-h^+}$ bin, respectively. Analogously, the vector $\vec{\hat{\mu}}$ encodes to the model amplitude:

$$\hat{\mu}_j(m_{K\pi\pi}, t') = \begin{cases} \mathfrak{R}(\hat{\mathcal{T}}(m_{K\pi\pi}; m_{h^-h^+}^{[j/2]})) & \text{,if } j \text{ is even} \\ \mathfrak{I}(\hat{\mathcal{T}}(m_{K\pi\pi}; m_{h^-h^+}^{[j/2]})) & \text{,if } j \text{ is odd.} \end{cases} \tag{4.4}$$

Using these two vectors simplifies the χ^2 function, which reads:

$$\chi^2 = \sum_{t', m_{K\pi\pi}} \sum_{i,j} \Delta\mu_i(m_{K\pi\pi}, t') \text{Prec}\left[\mu_i(m_{K\pi\pi}, t'), \mu_j(m_{K\pi\pi}, t')\right] \Delta\mu_j(m_{K\pi\pi}, t'), \tag{4.5}$$

where

$$\Delta\mu_i(m_{K\pi\pi}, t') = \mu_i(m_{K\pi\pi}, t') - \hat{\mu}_i(m_{K\pi\pi}, t'), \tag{4.6}$$

and $\text{Prec}[\mu_i, \mu_j]$ is the precision matrix, which is the inverse of the covariance matrix obtained from the freed-isobar PWD fit. More details on the covariance matrix can be found in section 4.4. Before a fit is performed, start-parameter values for the free parameters are randomly chosen. The χ^2 optimization then minimizes the χ^2-value of the model with respect to the free parameters, such as the shape parameters ζ and the coupling amplitudes C. To avoid a bias due to the randomly chosen start-parameters, each RMF is fitted 250 times with different start-parameters. The result of the fit with the lowest χ^2-value, that meets our convergence criteria (see section 4.5),

is adopted. The free parameters must stay within predefined boundaries to ensure physical results and stability of the fit, e.g. the boundaries for resonant components are chose so that they do not overlap.

4.4 Statistical Uncertainties of the RMF

The statistical uncertainties of the RMF are represented by the covariance matrix. For a χ^2-fit it is approximated by

$$\left(\mathrm{Cov}^{-1}\right)_{ij} = \frac{1}{2}\left[\frac{\partial^2\chi^2}{\partial\theta_i\partial\theta_j}\right]_{\theta=\hat{\theta}}, \tag{4.7}$$

i.e. by the inverse of the χ^2 Hesse matrix evaluated at the parameters $\hat{\theta}$ [26]. The square-root of the diagonal elements of the covariance matrix give the uncertainty of the parameters, while the off-diagonal elements encode the correlation between the parameters. For more details on the covariance matrix of a log-likelihood function, see ref. z[26].

Our data set consists of about 720,000 events, which yields a small statistical uncertainty of our results. The systematic uncertainties for the freed-isobar PWD have not yet been determined in systematic studies, so we cannot provide systematic uncertainties. Therefore, the results of the RMFs are rounded to a precision of $1\,\mathrm{MeV}/c^2$ and reported without uncertainties, which is enough precision to perform the proof-of-principle studies aimed at in this work.

4.5 Convergence Criteria

Two criteria have to be met to consider an RMF as converged. First of all a χ^2-minimum must be found. This is the case if the covariance matrix is positive definite, i.e. all eigenvalues of the covariance matrix are positive. Second, no parameter has reached its predefined parameter limits. The bounds prevent the fit from finding an unphysical solution, such as negative masses or widths much larger than any known resonance. The configuration of all RMFs performed for this thesis, including the parameter bounds of the dynamic amplitudes, can be found in ref. [27].

5 Applicability of Wilks' Theorem to Resonance-Model Fits

To estimate the statistical significance of model components, a hypothesis test was performed on them. To this end, we performed two RMFs with different models. The so-called null model is a model that does not contain the component for which the significance should be calculated. The null model has h free parameters. The alternative model includes the component of interest. It has m free parameters. The rest, e.g. the included $m_{K\pi\pi}$, t' and $m_{h^-h^+}$ bins, is the same in both RMFs. Due to the smaller number of parameters, the χ^2-value of the null model will be larger than that of the alternative model. The test statistic T is given by the difference in χ^2-values of the two RMFs $\Delta\chi^2$. With the Probability-Density Function (PDF) of the test statistic the p-value can be calculated with the survival function:

$$p(\Delta\chi^2) = \int_{\Delta\chi^2}^{\infty} f(x;\theta)\mathrm{d}x, \tag{5.1}$$

which integrates the PDF from the $\Delta\chi^2$-value from which the p-value is desired of to infinity. The resulting p-value can then be translated into a significance with the inverse survival function of the standard normal distribution ($\mu = 0$, $\sigma = 1$). Wilks' theorem states that the PDF can be approximated by a χ^2-distribution [28]

$$f(x) = \begin{cases} \frac{1}{\Gamma(df/2)2^{(df/2)}}x^{df/2-1}e^{-x/2} & ,0 < x < \infty \\ 0 & ,\text{elsewhere}, \end{cases} \tag{5.2}$$

with $df = h - m$ degrees of freedom [9]. Γ denotes the Gamma function [28]:

$$\Gamma(\alpha) = \int_0^{\infty} y^{\alpha-1}e^{-y}\mathrm{d}y. \tag{5.3}$$

The likelihoods must satisfy regularity conditions in the parameter space for Wilks' theorem to be applicable [28]. The RMF do not satisfy one of the regularity conditions, which states that the PDFs $f(x_i;\theta)$ with parameters θ must be distinct, i.e., if $\theta \neq \theta'$ then $f(x_i;\theta) \neq f(x_i;\theta')$. Our models with parameters $\theta = \{\Re(C), \Im(C), m_0, \Gamma_0, ...\}$, where C is the coupling factor and m_0 and Γ_0 are the nominal mass and width of a Breit-Wigner component, respectively, do not satisfy the regularity condition. If both models have a coupling amplitude of zero and different mass and width parameters, then this implies that both PDFs are the same, as the coupling amplitudes are zero, i.e. as the Breit-Wigner component does not contribute to the total model curve. This condition is automatically fulfilled in our RMFs, since the null model does not contain the Breit-Wigner component and has by default a coupling amplitude of zero. Thus, the regularity condition is violated by RMFs.

5.1 Toy Studies of Applicability of Wilks' Theorem to RMFs

To test for the discrepancy between the results from Wilks' theorem and the actual significance, which we will call the true significance, we performed toy studies. To this end, we randomly generated toy datasets of an amplitude consisting of a single resonance to determine the true significance under the assumption of the null hypothesis. As true amplitude a Breit-Wigner amplitude with resonance parameters from the PDG for the $K^*(892)$ (blue dots in fig. 5.1) was used [2]. In total, 10 data points were evenly distributed in the mass range from 0.7 to 1.5 GeV/c^2. Each data point in the amplitude has the same uncertainty of $\sqrt{3/8}$ GeV/c^2. We know from the previous analysis of the data sample that the uncertainty of the intensity is proportional to its square-root, thus the uncertainty of the real and imaginary parts of the amplitude are expected to be roughly constant. To create a random toy sample from this amplitude, at each mass point, we randomly draw values for the real and imaginary parts from a normal distribution centered around the corresponding true amplitude value with the standard deviation given by the uncertainty (orange crosses in fig. 5.1).

The toy datasets are fitted by models in an RMF. The models contain either one or two Breit-Wigner components, to model the null hypothesis or the alternative hypothesis, respectively. We created four different scenarios to test our method and the discrepancy between Wilks'
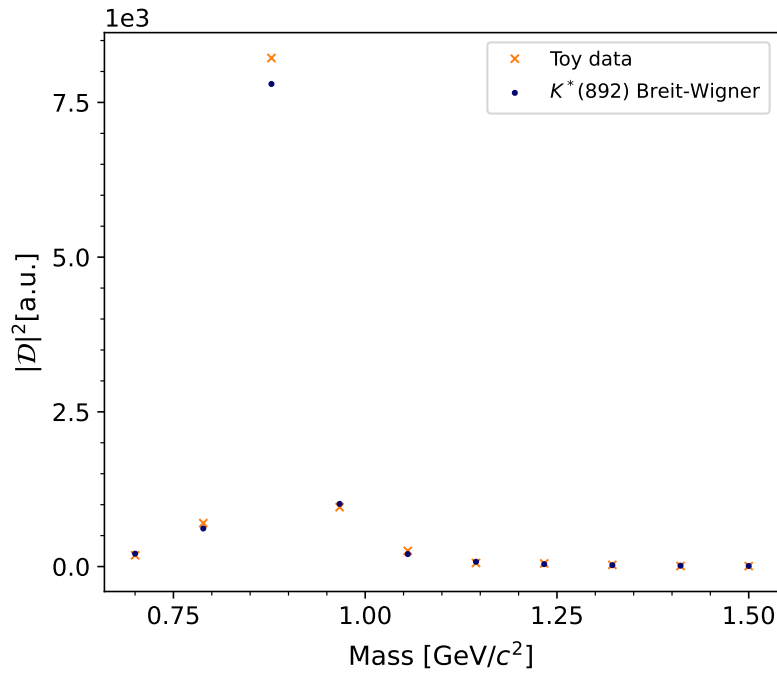
Figure 5.1: Intensity Spectrum with a Breit-Wigner amplitude of the $K^*(892)$ (blue dots). An exemplary toy dataset is shown by the orange crosses.

significance and the true significance. In the first scenario, we compare the distribution of χ^2-values obtained by fitting a Breit-Wigner component with fixed parameters to a real χ^2-PDF with corresponding degrees of freedom (see section 5.1.1). Then, a second fixed-parameter Breit-Wigner component is added, and the difference in χ^2-values of the one and two Breit-Wigner component fits are compared to the corresponding χ^2-PDF (see section 5.1.2). In the next two scenarios, the difference in significance calculated with Wilks' theorem and the real PDF is calculated. Here, the second Breit-Wigner component has free parameters. The toys of the third scenario are performed with one bin (see section 5.1.3), while the toys of the fourth scenario are performed with four bins (see section 5.1.4).

5.1.1 Model with One Breit-Wigner Component

The goal of the first toy study is to compare the real PDF of χ^2-values obtained in fitting several toy samples to a χ^2-PDF. In this step, we actually did not use the full mass range mentioned earlier, but a mass range from 0.7 to 1.1 GeV/c^2 with 10 equally spaced points, as this mass range is enough to cover the single Breit-Wigner component. The toy samples were fitted with a simple model containing only a Breit-Wigner component with resonance parameters fixed to the same values as the Breit-Wigner amplitude. Thus, only the real and imaginary part of the coupling amplitude for this single Breit-Wigner component were fitted. The degrees of freedom are given by difference between the number of data points and the free parameters, i.e., $df = 18$
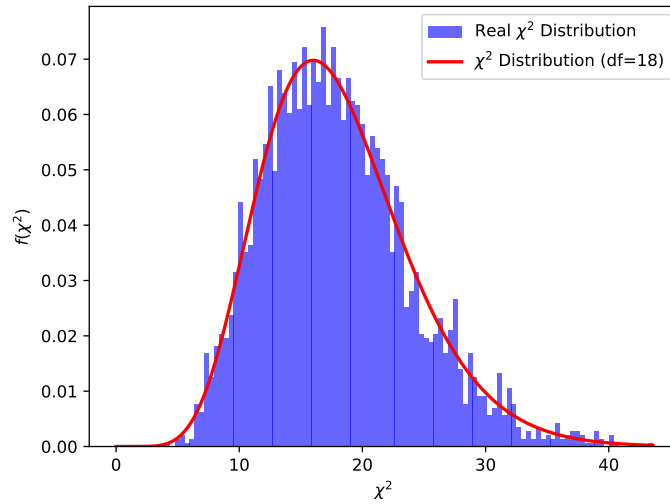
Figure 5.2: Histogram of χ^2-values obtained in toy samples with a single Breit-Wigner component with fixed resonance parameters (blue bars). The χ^2-PDF function with degrees of freedom of 18 is shown by the red curve.

[1]. We created 3600 toy samples with one fit attempt for each toy. The χ^2-value of each fit was collected. Figure 5.2 shows the numerical approximation of the true PDF.

The histogram of the real distribution (blue bars) has a similar shape to the χ^2-PDF (red line). Even though, the bars do not perfectly match the χ^2-distribution due to statistical fluctuations resulting from the limited number of toys created, the real distribution is well approximated by the χ^2-PDF, as expected. This first test was just to proof-the-principle of the further toy studies.

5.1.2 Models with Two Fixed Breit-Wigner Components

In the second set of toy studies, two models were fitted once on the same toy. The first model is the same one used in section 5.1.1. The second model adds an additional Breit-Wigner component with parameters fixed to the values of the $K^*(1410)$[2] [2]. The additional Breit-Wigner component does only fit statistical fluctuations, since the data sample just contains a single Breit-Wigner amplitude. This makes a total of four free parameters all from the two coupling factors. We are now interested in the distribution of the difference of the χ^2-values $\Delta\chi^2$. Wilks' theorem states that $\Delta\chi^2$ is distributed like a χ^2-PDF. In these studies, we want to test this statement in a case where the regularity condition is fulfilled. The regularity condition
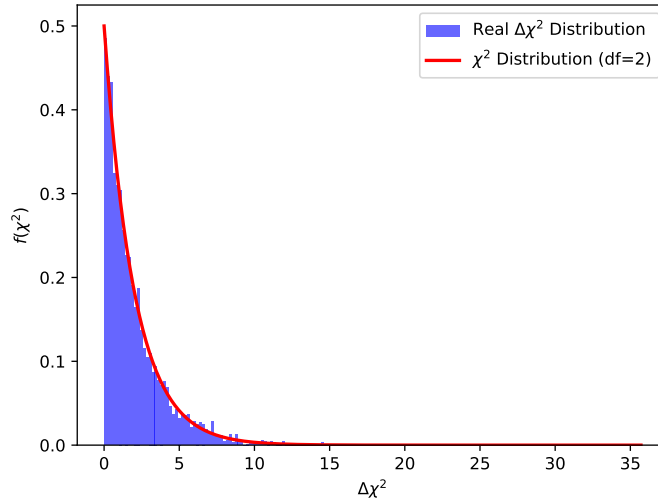
Figure 5.3: Histogram of $\Delta\chi^2$ obtained in toy studies with one Breit-Wigner component and two Breit-Wigner components with fixed resonance parameters (blue bars). The χ^2-PDF with degrees of freedom equal to the difference in parameters of the two models used is shown by the red curve.

---

[1]Note that the real and imaginary parts of the Breit-Wigner amplitude are counted as one degree of freedom each.
[2]Note that from now on all toys will have mass range from 0.7 to 1.5 GeV/c^2 to accommodate the second Breit-Wigner component.

is fulfilled, because the additional Breit-Wigner component has fixed resonance parameters, thus these parameters are not part of the parameter space. Therefore, the PDFs are distinct. The degrees of freedom of the χ^2-PDF are given by the difference in the number of parameters, i.e., $df = 2$. In this toy study, we generated 3600 toy samples to obtain the true distribution.

The true distribution of $\Delta\chi^2$ is very well approximated by the χ^2-PDF as shown in fig. 5.3. These toys do not represent the case we would expect in a normal analysis. There the resonance parameters are not fixed, so in the following two toy studies the second Breit-Wigner component has free resonance parameters.

5.1.3 Models with Two Breit-Wigner Components in One Bin

The goal of the third toy study is to get a first estimate of the discrepancy between the true significance computed with the true distribution and the significance computed under the assumption of Wilks' theorem. To this end, the true distribution must be determined accurately also in the tails of the distribution. Thus, we generated 100,000 toy samples. Each toy sample was fitted by the model with only the $K^*(892)$ Breit-Wigner component, and by the second

Table 5.1: Summary of the boundaries used for the second Breit-Wigner component.

	Limits [GeV/c^2]
m_0	{1.1; 1.8}
Γ_0	{0.100; 0.600}
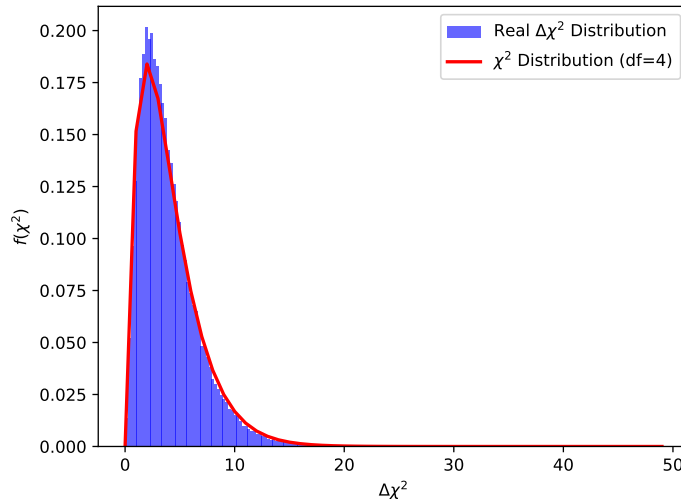
Figure 5.4: Same as fig. 5.3, but the second Breit-Wigner component in the second model has free resonance parameters.
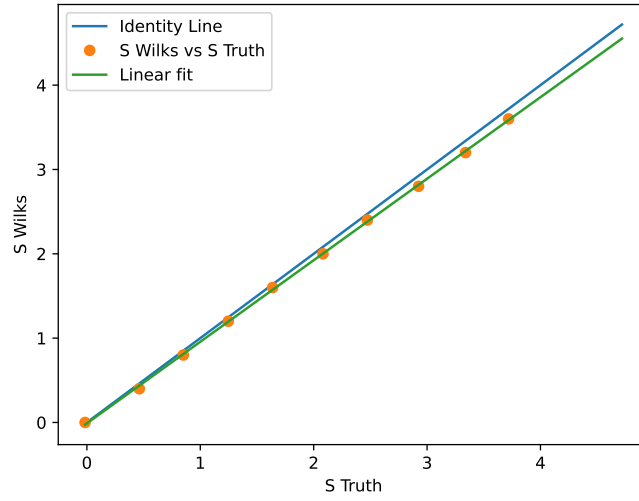
Figure 5.5: Plot of Wilks' approximated (vertical axis) and true (horizontal axis) value for the significance (orange dots). The green line is a linear fit through the orange data points to estimate the trend. The blue line corresponds to the identity line, i.e. the line we would expect to see if the assumptions of Wilks' theorem apply to our system.

model, which is similar to the second model used in section 5.1.2. The only difference being that the second Breit-Wigner component, i.e., not the $K^*(892)$ one, has free resonance parameters. To ensure to find the best minimum, i.e. the lowest χ^2-value for each toy sample, the first model was fitted 10 times and the second model 30 times. Similar to the real RMFs, we limited the values that the parameters could take to be realistic to the real analysis. The boundaries are summarized in table 5.1. This model now has six free parameters in total, four of the coupling amplitudes and one each for the nominal mass and width of the second Breit-Wigner component. This means that the degrees of freedom of the χ^2-PDF are $df = 4$.

The model with two Breit-Wigner components was only able to converge in 8.4 % of the toys. This is due to the lack of a statistically significant structure in the toy samples that the second Breit-Wigner component could describe. Since the second Breit-Wigner is used by the fit to describe statistical fluctuations, the fits often yield resonance parameters at their boundaries. Figure 5.4 shows the resulting distribution of $\Delta\chi^2$-values. Overall, the true distribution is still fairly well approximated by the χ^2-PDF, although the regularity condition is now violated. We just observe that the $\Delta\chi^2$-distribution has a higher peak than the χ^2-PDF, but therefore has lower values towards higher $\Delta\chi^2$ values.

We calculated the significance using the true distribution and the χ^2-PDF, as suggested by Wilks' theorem, and compared the values (see fig. 5.5). Wilks' theorem slightly underestimates the true significance, indicated by the orange points below the blue identity line. This means

that Wilks' theorem is a good approximation for the true significance.

5.1.4 Models with Two Breit-Wigner Components in Four Bins

In the analysis of the freed-isobar amplitudes, the data are binned into many $(m_{K\pi\pi}, t')$ cells, while in the toy studies discussed so far, we fitted to only a single amplitude spectrum, i.e. a single $(m_{K\pi\pi}, t')$ cell. Thus, the fourth toy study uses the same models as in section 5.1.3, but with a toy sample that consists of four t' bins. To this end, we draw four random amplitudes, that are combined into one toy sample with four t' bins, where each amplitude corresponds to one t' bin. All four t' bins are fitted simultaneously, similar to the real RMFs. As a consequence, the ratio of resonance parameters to coupling amplitudes decreases, which is closer to the reality of the RMFs. The first model, which contains only the $K^*(892)$ Breit-Wigner component now has 8 free coupling amplitudes, two for each t' bin. The second model, now has 16 free coupling amplitudes compared to two free resonance parameters. This results in $df = 10$ for the χ^2-distribution. To obtain significances with the true distribution up to 5σ, a total of about three million toy samples, consisting each of four t' bins, were generated and fit, of which 11 % converged.

Figure 5.6 shows the resulting $\Delta\chi^2$-distribution, which shows a slight right shift toward higher $\Delta\chi^2$-values compared to the χ^2-distribution. Nevertheless, the real distribution has a similar shape as the χ^2-distribution. Calculating the significance values allows us to assess whether Wilks' theorem provides a good approximation of the true distribution. Figure 5.7 shows that under the assumptions of Wilks' theorem, the significance of the components is overestimated.
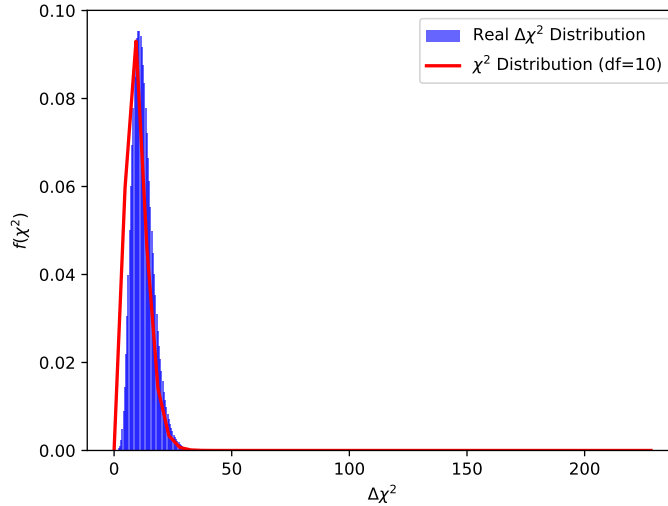
Figure 5.6: Same as fig. 5.3. Here, the second Breit-Wigner component in the second model has free parameters. The toys used contain 4 t' bins.
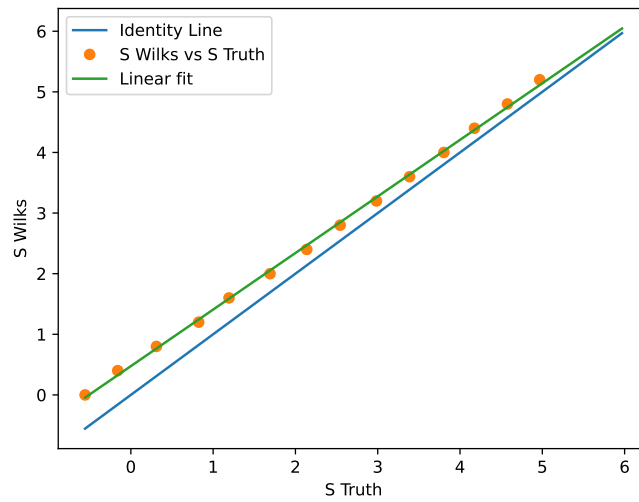
Figure 5.7: Same as fig. 5.5, but with values obtained from toys containing four t' bins.

Table 5.2: Summary of significance values computed with Wilks' theorem and the real distribution.

Wilks' σ	Real σ
0.0	-0.556032
0.4	-0.159442
0.8	0.311158
1.2	0.82477
1.6	1.19313
2.0	1.69158
2.4	2.13746
2.8	2.54311
3.2	2.9848
3.6	3.3869
4.0	3.80363
4.4	4.17549
4.8	4.5764
5.2	4.9682

At higher significance levels, the trend shows an approach of the true and Wilks significance. To quantify the discrepancy between the real and Wilks' theorem the significances are summarized in table 5.2. It shows that the discrepancy between Wilks' and the true significance in the region 3σ to 5σ is at about 0.3σ. In particle-physics there is the terminology that if a result has a significance of 3σ it is considered as an observation and with a significance over 5σ it is

considered as a discovery [29]. In the light of our toy studies, we recommend the significance of components to read about $4\,\sigma$ for an observation and about $6\,\sigma$ for a discovery.

In this chapter, the problems of using of Wilks' theorem in RMFs were discussed. In order to narrow down the impact of the broken regularity condition of the significance calculation, several toy studies were performed. First, we visually confirmed that the true distributions of χ^2 and $\Delta\chi^2$ obtained in the toy studies take a χ^2-PDF form, when the regularity conditions are not violated. Then, when violating the regularity condition as in the RMFs, the discrepancy between the true significance and Wilks' significance was determined. The discrepancy is at about $0.3\,\sigma$ in the interesting range of $3\,\sigma$ to $5\,\sigma$. From our studies, we recommend for our and other analyses to add a buffer of about $1\,\sigma$ to the significance obtained with Wilks' theorem. We cannot give a definitive answer to the size of the buffer, since there are some limitations to the performed toy studies. We have assumed data points that are perfectly normally distributed, which in nature does not have to be the case. And we only performed the toy studies with four t' bins, and not a complete set of $(m_{K\pi\pi}, t')$ cells that we use in the RMFs. Within the limitations of our studies, it appears that violating the regularity condition does not have a major impact on the results obtained using Wilks' theorem.

6 Results of Resonance-Model Fits

6.1 $[K\pi]_P$ Amplitude

The $[K\pi]_P$ amplitude represents the $K^-\pi^+$ subsystem where both particles are in a P-wave configuration. In this subsystem we expect K^* resonances with quantum numbers $J^P = 1^-$, for which the PDG states the $K^*(892)$, $K^*(1410)$ and $K^*(1680)$. The $K^*(892)$ is a well established state. Therefore, this state is used as a standard candle to prove the concept of the freed-isobar method. The measured amplitude is shown in fig. 6.1. The $(m_{K\pi\pi}, t')$ cell for fig. 6.1(a) shows best the structure of two peaks. In most of the other cells, the peak at about $1.5\,\mathrm{GeV}/c^2$ is not as prominent (see fig. 6.1(b)). The peak at about $0.9\,\mathrm{GeV}/c^2$ is clearly present in all cells. Its position agrees with the $K^*(892)$. The peak at about $1.5\,\mathrm{GeV}/c^2$ indicates an excited K^* state, as discussed in section 6.1.2.

(a)   (b)
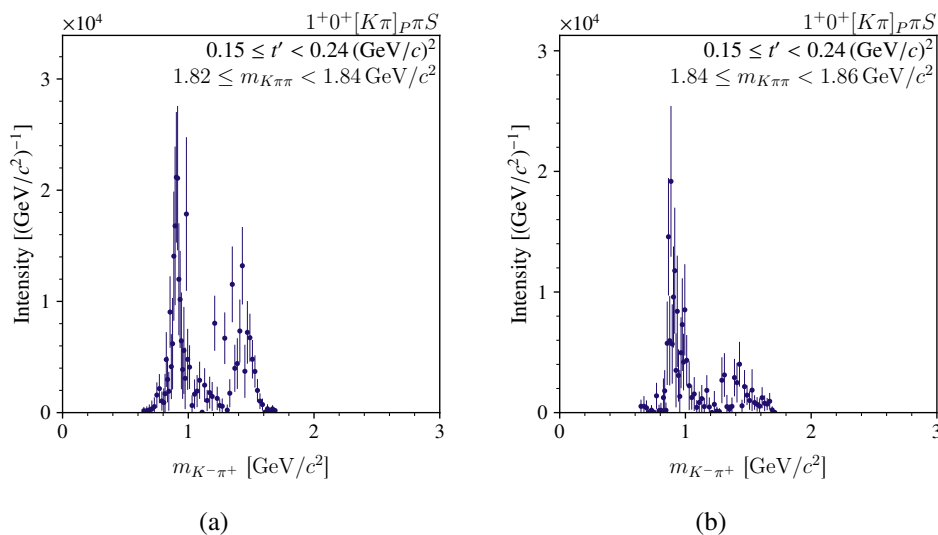
Figure 6.1: Intensity spectra of the $[K\pi]_P$ amplitude as a function of the invariant mass of the $K^-\pi^+$ subsystem. In (a), one $(m_{K\pi\pi}, t')$ cell has been chosen that best represents the structure of two peaks. (b) shows a cell in which the peak at about $1.5\,\mathrm{GeV}/c^2$ is not as prominent.

Table 6.1: Summary of components and data constraints of the performed systematic studies of the RMF at the $1^+0^+[K\pi]_P \pi S$ wave. The first column shows the name of the RMF. The second column shows the $m_{K\pi\pi}$ bins that were included in the RMF. The third column shows the $m_{K^-\pi^+}$ bins that were included in the RMF. The fourth column shows the Resonant components that were used in the RMF. The fifth column shows whether a nonresonant component was used and if so, whether its parameter was fixed to zero or given as a free parameter to the RMF. The last column shows whether the fit converged or not.

	$m_{K\pi\pi}$ range [GeV/c^2]	$m_{K^-\pi^+}$ range [GeV/c^2]	Resonant component	Nonres component	Convergence behavior
main 1	{1.1; 2.5}	{0.0; 1.1}	1 Breit-Wigner	None	converged
study 1.a	{1.1; 2.5}	{0.0; 1.0}	1 Breit-Wigner	None	converged
study 1.b	{1.1; 2.5}	{0.0; 1.1}	1 Breit-Wigner	free	converged
study 1.c	{1.1; 2.5}	{0.0; 1.0}	1 Breit-Wigner	free	converged
study 1.d	{1.1; 2.5}	{0.0; 1.1}	1 Breit-Wigner	fixed	converged
study 1.e	{1.1; 2.5}	{0.0; 1.0}	1 Breit-Wigner	fixed	converged
study 1.f	{1.16; 1.5}	{0.0; 1.1}	1 Breit-Wigner	None	converged
study 1.g	{1.16; 1.5}	{0.0; 1.0}	1 Breit-Wigner	None	converged
study 1.h	{1.16; 1.5}	{0.0; 1.1}	1 Breit-Wigner	fixed	converged
study 1.i	{1.16; 1.5}	{0.0; 1.0}	1 Breit-Wigner	fixed	converged
study 1.j	{1.16; 1.5}	{0.0; 1.1}	1 Breit-Wigner	free	converged
study 1.k	{1.16; 1.5}	{0.0; 1.0}	1 Breit-Wigner	free	converged

6.1.1 Models with One Breit-Wigner Component

To study the peak at about $0.9\,\text{GeV}/c^2$, we include only the region $0 < m_{K^-\pi^+} < 1.1\,\text{GeV}/c^2$ and only $m_{K\pi\pi}$ cells above $1.1\,\text{GeV}/c^2$ in an RMF modeled by a single Breit-Wigner component. The data were chosen to ensure production of the $K^*(892)$, while excluding excited states. Figure 6.2 shows intensity spectra and phase plots of the $[K\pi]_P$ amplitude with the result of the RMF as the red curve of main 1 (see table 6.1). The RMF reproduces well the intensity spectra up to about $m_{K\pi\pi} = 2\,\text{GeV}/c^2$ (see fig. 6.2(a)). For higher $m_{K\pi\pi}$ cells, the RMF cannot produce a curve that appears to pass through the data points (see fig. 6.2(c)). The phase plots (figs. 6.2(b) and 6.2(d)) show a similar picture. In the lower $m_{K\pi\pi}$ bin (fig. 6.2(b)) the RMF phase curve reproduces the phase spectrum very well, while in the higher $m_{K\pi\pi}$ bin (fig. 6.2(d)), the RMF does not reproduce the phase spectrum as well.

To study the stability of the RMF, several studies have been conducted. The conditions of the studies are summarized in table 6.1. First, the effect of different $m_{K^-\pi^+}$ upper limits was studied in study 1.a. This study does not show any significant changes in the intensity spectra nor in the resonance parameters. Next, the contributions of a nonresonant component was investigated in studies 1.b-1.e. Here, we used both $m_{K^-\pi^+}$ bounds and added a nonresonant

(a)

(b)

(c)

(d)
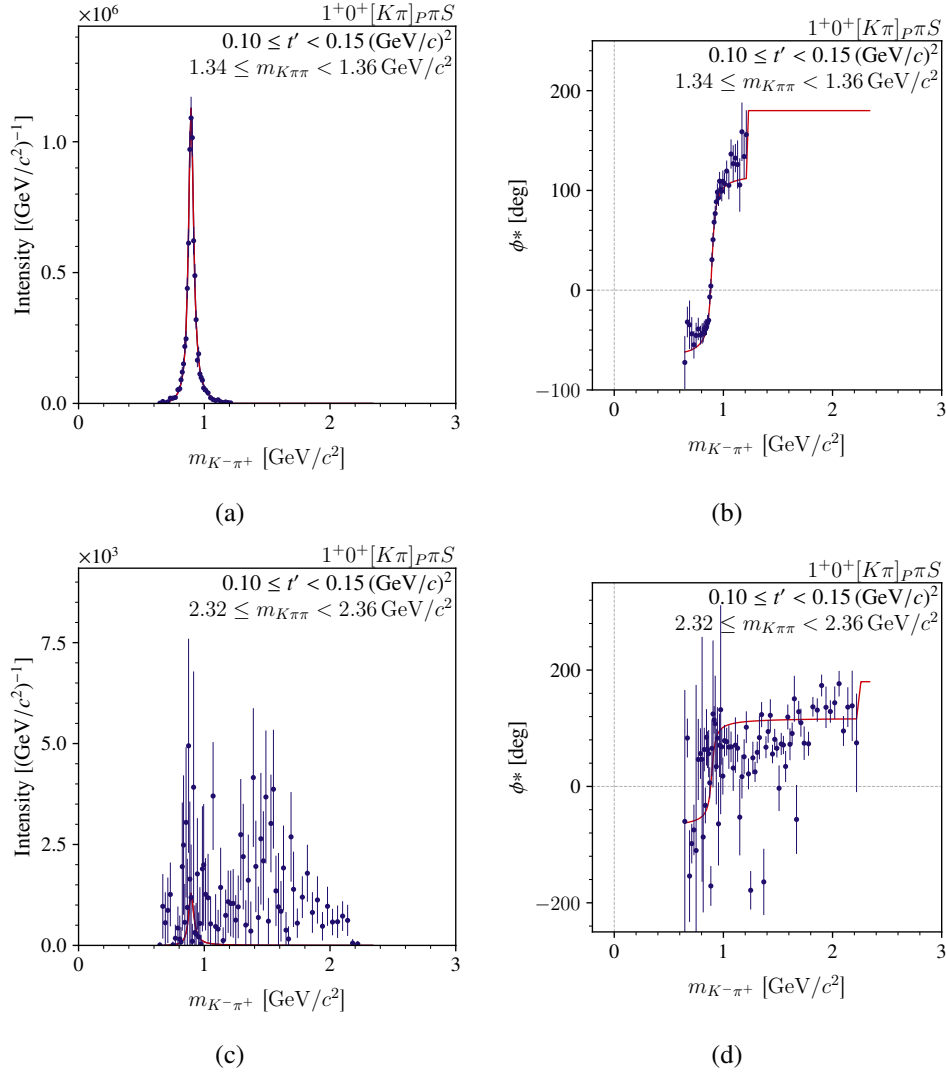
Figure 6.2: Intensity (left column) and phase (right column) diagrams of the $1^+0^+[K\pi]_P\pi S$ wave at $m_{K\pi\pi} \approx 1.31\,\text{GeV}/c^2$ (top row) and at $m_{K\pi\pi} \approx 1.41\,\text{GeV}/c^2$ (bottom row) in the lowest t' bin of main 1. The results of the freed-isobar PWD are shown as blue data points. The red curve is the model curve calculated by the RMF.

component, whose parameter was once fixed to zero[1] and once included as a free parameter to the RMF. Figure 6.3 shows the intensity spectra for study 1.b. They are representative for studies 1.b-1.e. Figure 6.3(a) shows the intensity spectrum of a low $m_{K\pi\pi}$ bin in the lowest t' bin. The nonresonant component does not make a big contribution to the model curve. In higher $m_{K\pi\pi}$ cells, a higher nonresonant background contribution is detected (see fig. 6.3(b)),

---

[1]This way the coupling for a fixed shape is determined to better understand the significance of the nonresonant parameter to the model.

(a)

(b)
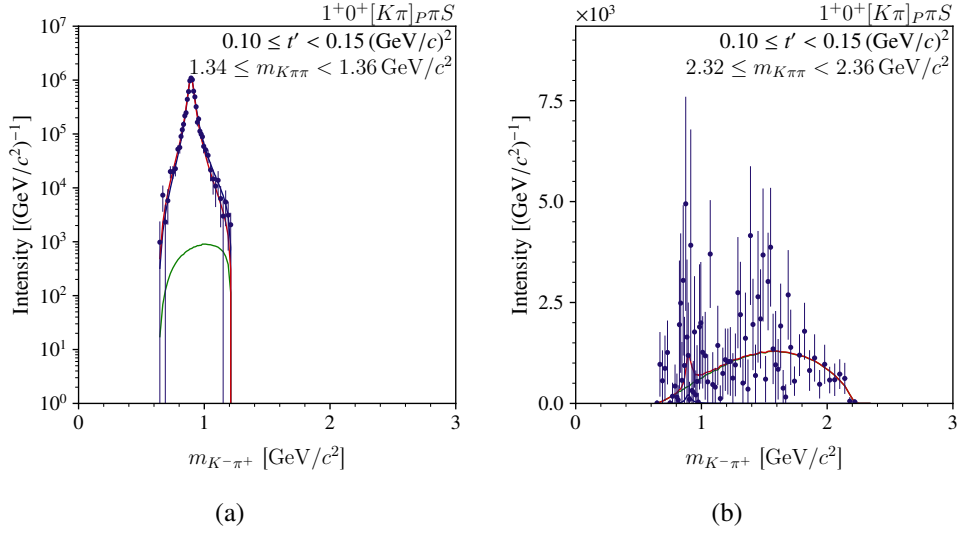
Figure 6.3: Same as in fig. 6.2, but for the intensity of the ($m_{K\pi\pi} \approx 1.35\,\text{GeV}/c^2$, $t' \approx$ $0.125\,\text{GeV}/c^2$) and ($m_{K\pi\pi} \approx 2.34\,\text{GeV}/c^2$, $t' \approx 0.125\,\text{GeV}/c^2$) cell of the RMF for study 1.b from table 6.1. The intensity spectrum (a) is plotted on a logarithmic scale in order to display the nonresonant background curve more visible.

Table 6.2: Same as table 6.1, but for two Breit-Wigner component models in the $[K\pi]_P$. Note that in studies 1.k and 1.m, all availabe $m_{K^-\pi^+}$ bins in a $m_{K\pi\pi}$ cell are fitted.

	$m_{K\pi\pi}$ range [GeV/c^2]	$m_{K^-\pi^+}$ range [GeV/c^2]	Resonant component	Nonres component	Convergence behavior
study 1.k	{1.5; 2.0}	{0.7; 1.9}	2 Breit-Wigner	free	converged
study 1.l	{1.2; 2.36}	{0.7; 2.2}	2 Breit-Wigner	free	not converged
study 1.m	{1.5; 2.0}	{0.7; 2.7}	2 Breit-Wigner	free	not converged
study 1.n	{1.1; 2.5}	{0.0; 1.0}	2 Breit-Wigner	free	not converged

leading to high destructive interference with the Breit-Wigner component. This behavior can be observed in cells with $m_{K\pi\pi} \gtrsim 2\,\text{GeV}/c^2$. Finally the effect of a different set of $m_{K\pi\pi}$ cells was studied. Therefore, main 1 and studies 1.a-1.e were repeated with a $m_{K\pi\pi}$ range of {1.16; 1.5}GeV/c^2 in studies 1.f-1.k. These studies lead to no significant changes, meaning that the $m_{K\pi\pi}$ range has only little effect on the RMF.

6.1.2 Models with Two Breit-Wigner Resonances

To study the peak at about $1.5\,\text{GeV}/c^2$, models with two Breit-Wigner components were investigated. Models with different sets of ($m_{K\pi\pi}$, t') cells, without a nonresonant component and also with one have been tried out. In the end, only four models were able to calculate resonance parameters, of which only one fit converged. The fit conditions are summarized in

table 6.2. In the following two of these models are discussed.

First, we look at the only RMF that converged. This model curve reproduces the peak at about $0.9 \,\mathrm{GeV}/c^2$ very well (see fig. 6.4). Around this mass, the nonresonant component contributes little to the model curve. The peak at about $1.5 \,\mathrm{GeV}/c^2$ is not well reproduced. The RMF is unable to form a second peak and only forms a small plateau at higher energies. This plateau is caused by high destructive interference between the Breit-Wigner and the nonresonant component. Both phase spectra are well reproduced by the RMF. The phase shift of both

(a)

(b)

(c)

(d)
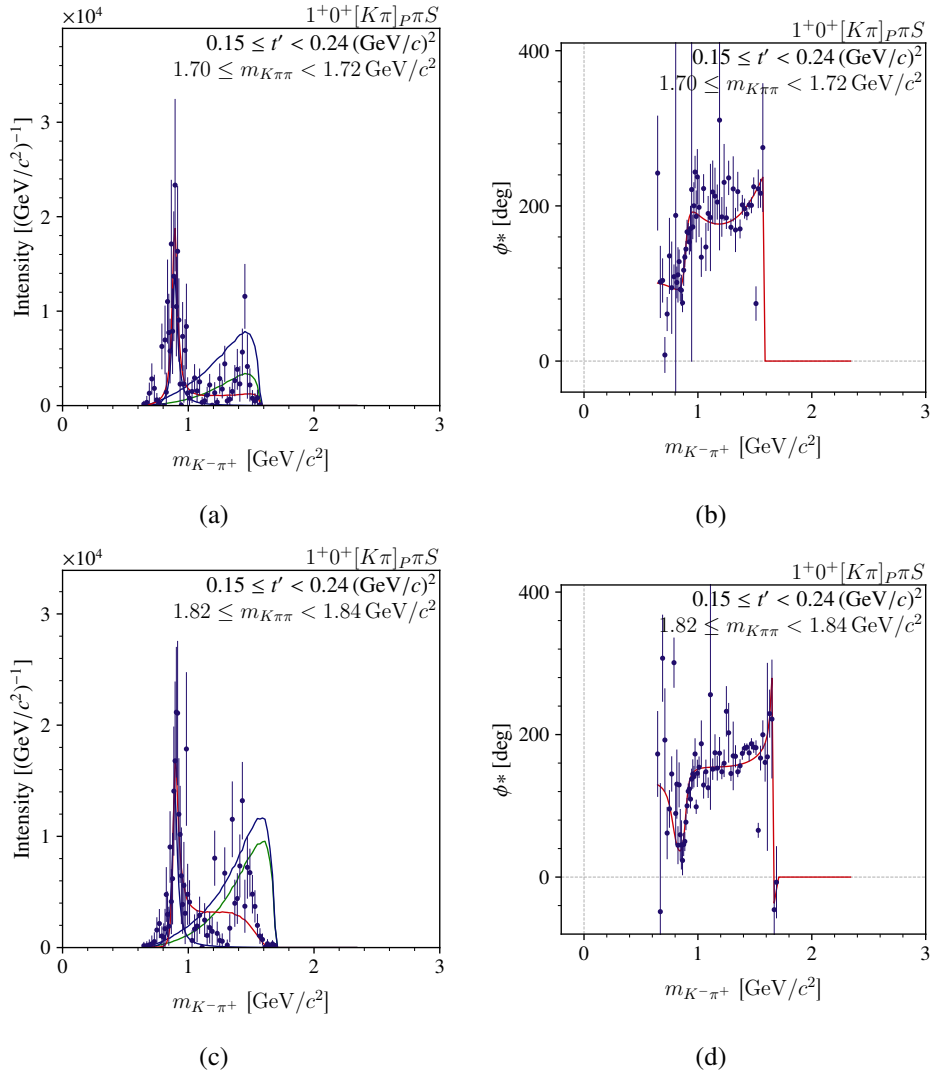
Figure 6.4: Same as in figure fig. 6.2, but for a model with two Breit-Wigner and a nonresonant component (study 1.k). The three body mass bins are at $m_X \approx 1.71 \,\mathrm{GeV}/c^2$ (top row) and $m_X \approx 1.83 \,\mathrm{GeV}/c^2$ (bottom row). Both are in the second t' bin.
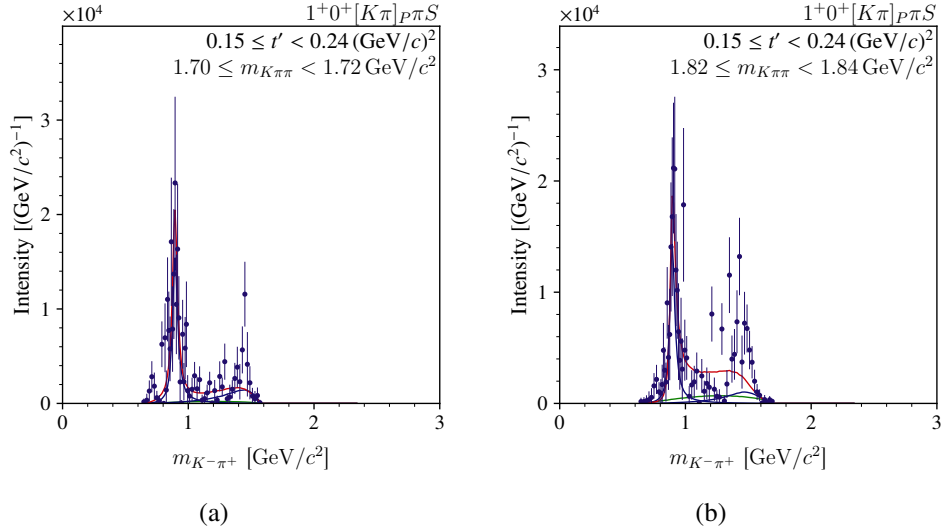
Figure 6.5: Same as fig. 6.2, but for intensity of study 1.l of the $[K\pi]_P$ amplitude. The left plot show the $(m_{K\pi\pi} \approx 1.71\,\text{GeV}/c^2, t' \approx 0.125\,\text{GeV}/c^2)$ cell. The right plot shows the $(m_{K\pi\pi} \approx 1.83\,\text{GeV}/c^2, t' \approx 0.125\,\text{GeV}/c^2)$ cell.

resonances can be observed from the data points and the model curve.

The second RMF we want to present is the model 1.l. This RMF did not converge because a minimum was found that does not meet the requirements for a valid minimum, as at least one parameters from a Breit-Wigner component hit its bounds. The next best minimum that met the requirements was used for this RMF. Here, the model does not use a large destructive interference between the Breit-Wigner and the nonresonant background component to reproduce the intensity spectrum (see fig. 6.5). Overall, the nonresonant component contributes little to the model curve, which is similar to the one Breit-Wigner component fits.

6.1.3 Discussion

The RMF with one Breit-Wigner component yielded a mass of $m = 895\,\text{MeV}/c^2$ and a width of $\Gamma = 49\,\text{MeV}/c^2$[2]. The PDG average lists the $K^*(892)$ resonance at a mass of $m_{\text{PDG, 892}} = (895.55 \pm 0.20)\,\text{MeV}/c^2$ and a width of $\Gamma_{\text{PDG, 892}} = (47.3 \pm 0.5)\,\text{MeV}/c^2$ [2]. The resonance parameters obtained from the studies and the two Breit-Wigner component fits are summarized in fig. 6.6. Although a full set of systematic studies have not been performed, we seem to observe a very clear $K^*(892)$ signal. Not only do we observe a very clear peak in most of the $(m_{K\pi\pi}, t')$ cells, but also most of the RMFs gave resonance parameters, that are well within the range of other measurements. The two outliers that can be seen in fig. 6.6 result from

---

[2]We give the results rounded to $1\,\text{MeV}/c^2$ without uncertainties, because the systematic uncertainties are not determined yet, as discussed in section 4.4.
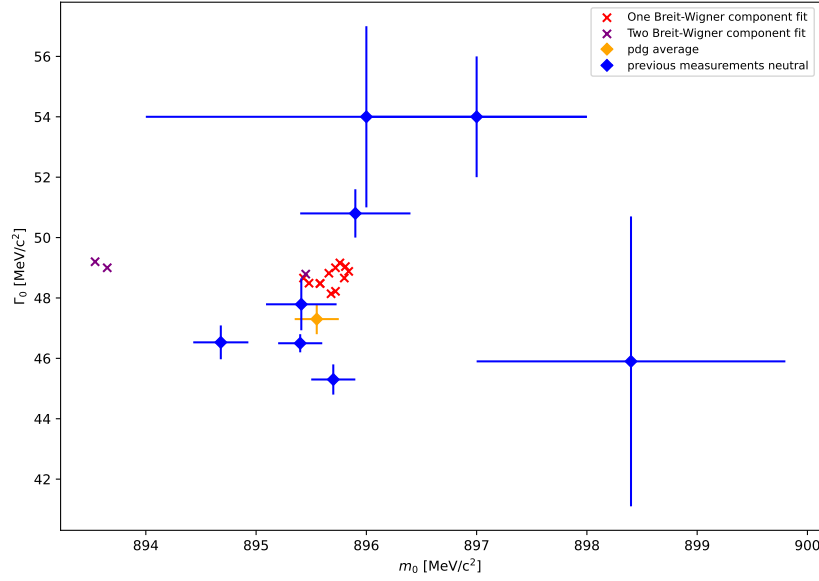
Figure 6.6: Summary of the resonance parameters for the $K^*(892)$ obtained in systematic studies. The horizontal axis represents the mass and the vertical axis represents the width. The plot includes the PDG average for the $K^*(892)$ as well as the last 8 measurements that gave both a value for mass and width [2]. Note no uncertainties are presented, as discussed in section 4.4. The results are rounded to a precision of $0.01\,\mathrm{MeV}/c^2$ to better distinguish the individual points.

studies 1.m and 1.n described in table 6.2. These RMFs did not converge and should be treated with caution.

The first RMF discussed in section 6.1.2 yielded a mass of $m = 1741\,\mathrm{MeV}/c^2$ and a width of $\Gamma = 442\,\mathrm{MeV}/c^2$ for the peak at about $1.5\,\mathrm{GeV}/c^2$. The nearest known resonance, stated by the PDG is the $K^*(1680)$ with a mass of $m_{\mathrm{PDG,\,1680}} = (1718 \pm 18)\,\mathrm{MeV}/c^2$ and a width of $\Gamma_{\mathrm{PDG,\,1680}} = (322 \pm 110)\,\mathrm{MeV}/c^2$ [2]. The second RMF, discussed in section 6.1.2, yielded a mass of $m = 1503\,\mathrm{MeV}/c^2$ and a width of $\Gamma = 353\,\mathrm{MeV}/c^2$. These resonance parameters are closer to the $K^*(1410)$, for which the PDG gives a mass of $m_{\mathrm{PDG,\,1410}} = (1414 \pm 15)\,\mathrm{MeV}/c^2$ and a width of $\Gamma_{\mathrm{PDG,\,1410}} = (232 \pm 21)\,\mathrm{MeV}/c^2$ [2]. The resonance parameters of all RMFs are summarized in fig. 6.7. Using Wilks' theorem on model 1.k (see table 6.2) a significance for the peak at about $1.5\,\mathrm{GeV}/c^2$ of $21.08\,\sigma$ was determined. Therefore, this resonance is not a statistical fluctuation, but may results from a resonance. However, this resonance cannot be further characterized, since different models gave different results, either closer to the $K^*(1410)$ or the $K^*(1680)$. Systematic studies of the two Breit-Wigner component RMF could help to characterize the peak, but a slight change in the fitting conditions have caused the Breit-Wigner
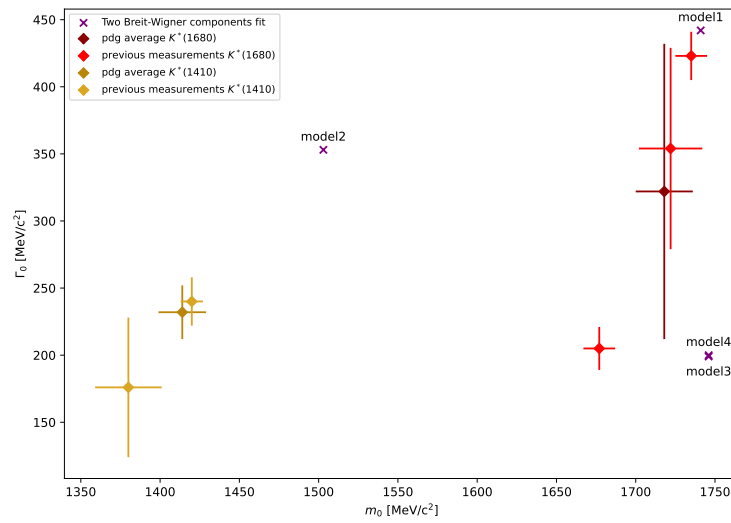
Figure 6.7: Same as fig. 6.6 for the resonance parameters of the $1.5\,\mathrm{GeV}/c^2$ peak. The PDG average for the $K^*(1430)$ and $K^*(1680)$ as well as all their previous measurements, considered by the PDG, are included [2].

parameters to hit their predefined bounds, as seen in section 6.1.2. Regardless of how the bounds were chosen, the same behavior was observed. Overall, the two Breit-Wigner component fits were very unstable and should be treated with caution. Therefore, further characterization of the peak is not possible. Further understanding of the freed-isobar PWD fit systematics could help in its characterization.

6.2 $[\pi\pi]_P$ Amplitude

The $[\pi\pi]_P$ amplitude represents the $\pi^-\pi^+$ subsystem, where both particles are in a P-wave configuration. We study this amplitude in the $1^+0^+[\pi\pi]_P KS$ wave. We expect ρ resonances to contribute to this amplitude with quantum numbers $J^P = 1^-$, for which the PDG lists the $\rho(770)$, $\rho(1450)$ and higher excited states. Figure 6.8(a) shows the measured intensity spectrum of the $[\pi\pi]_P$ amplitude in a $(m_{K\pi\pi}, t')$ cell. It contains a peak at about $0.8\,\text{GeV}/c^2$, which could correspond to the $\rho(770)$ state. This state is well established and can also be used as a standard candle to further prove the concept of the freed-isobar method. In higher $m_{K\pi\pi}$ bins, starting at about $1.4\,\text{GeV}/c^2$, the intensity spectra exhibit an enhanced intensity in the high-mass tail of the $0.8\,\text{GeV}/c^2$ peak, which we will call from now on enhanced intensity (see fig. 6.8(b)). This enhanced intensity is not a clear peak in any $(m_{K\pi\pi}, t')$ cells. It cannot be assigned to any known excited ρ state.

6.2.1 Models with One Breit-Wigner Component

To study the peak at about $0.8\,\text{GeV}/c^2$, an RMF with fit ranges $0 \leq m_{\pi^-\pi^+} \leq 0.9\,\text{GeV}/c^2$ and $1.1 \leq m_{K\pi\pi} \leq 1.6\,\text{GeV}/c^2$ containing a single Breit-Wigner component was fitted. These fit ranges yielded the lowest reduced χ^2-value of all RMFs with a single Breit-Wigner component. Hence, these fit ranges are selected as the main 2 RMF. This main 2 RMF (red curve) reproduces the measured intensity spectra (blue points) well for $m_{K\pi\pi} \lesssim 1.4\,\text{GeV}/c^2$ (see fig. 6.9(a)). The phase exhibits a clear rise of about $180°$, typical for a Breit-Wigner resonance, which is also well reproduced by the RMF (see fig. 6.9(b)). For higher $m_{K\pi\pi}$, in some $(m_{K\pi\pi}, t')$ cells the
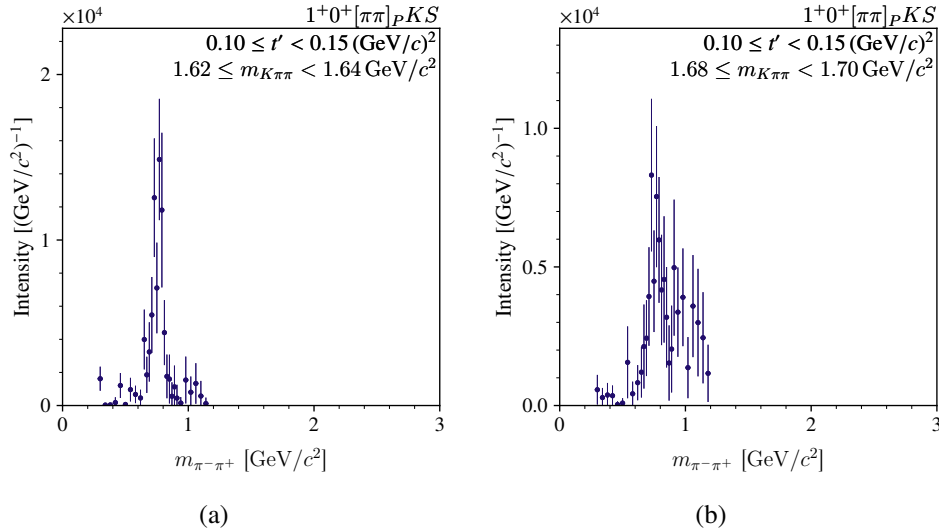
Figure 6.8: Same as fig. 6.1, but for the $[\pi\pi]_P$ amplitude in the $1^+0^+[\pi\pi]_P KS$ wave in two selected $m_{K\pi\pi}$ bins in the lowest t' bin.

(a)

(b)

(c)

(d)

(e)
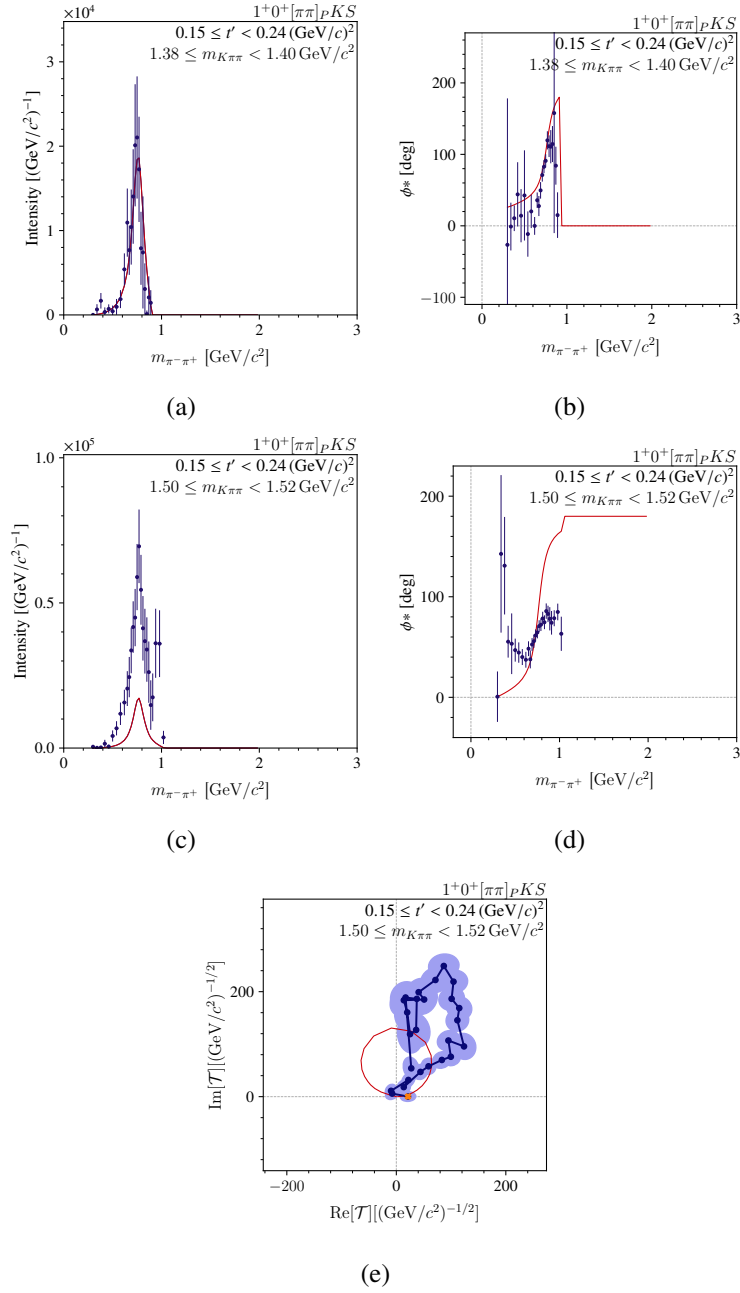
Figure 6.9: The first two rows are same as fig. 6.2, but showing the main 2 RMF of the $[\pi\pi]_P$ amplitude in the $1^+0^+[\pi\pi]_P KS$ wave at $m_{K\pi\pi} \approx 1.39\,\mathrm{GeV}/c^2$ (top row) and at $m_{K\pi\pi} \approx 1.51\,\mathrm{GeV}/c^2$ (middle row) in the second t' bin. (e) shows the Argand diagram, i.e. the real and imaginary parts of the amplitude, at $m_{K\pi\pi} \approx 1.51\,\mathrm{GeV}/c^2$ in the second t' bin. The orange cross indicates the data point of the lowest $m_{\pi^-\pi^+}$ bin and the blue shaded area represents the uncertainty ellipse.

Table 6.3: Same as table 6.1 for the one resonance component RMFs in the $[\pi\pi]_P$ amplitude.

	$m_{K\pi\pi}$ range [GeV/c^2]	$m_{\pi^-\pi^+}$ range [GeV/c^2]	Resonant component	Nonres component	Convergence behavior
main 2	{1.1; 1.6}	{0; 0.9}	1 Breit-Wigner	None	converged
study 2.a	{1.1; 1.6}	{0; 0.9}	1 Breit-Wigner	free	converged
study 2.b	{1.1; 1.6}	{0; 0.9}	1 Breit-Wigner	fixed	converged
study 2.c	{1.1; 1.6}	{0; 0.8}	1 Breit-Wigner	None	converged
study 2.d	{1.1; 1.6}	{0; 0.8}	1 Breit-Wigner	free	converged
study 2.e	{1.1; 1.6}	{0; 0.8}	1 Breit-Wigner	fixed	converged
study 2.f	{1.3; 2.48}	{0; 0.8}	1 Breit-Wigner	None	converged
study 2.g	{1.3; 2.48}	{0; 0.8}	1 Breit-Wigner	free	converged
study 2.h	{1.3; 2.48}	{0; 0.8}	1 Breit-Wigner	fixed	converged
study 2.i	{1.3; 2.48}	{0; 0.9}	1 Breit-Wigner	None	converged
study 2.j	{1.3; 2.48}	{0; 0.9}	1 Breit-Wigner	free	converged
study 2.k	{1.3; 2.48}	{0; 0.9}	1 Breit-Wigner	fixed	converged
study 2.l	{1.1; 1.6}	{0; 0.8}	1 Gounaris-Sakurai	None	converged
study 2.m	{1.1; 1.6}	{0; 0.8}	1 Gounaris-Sakurai	free	converged
study 2.n	{1.1; 1.6}	{0; 0.8}	1 Gounaris-Sakurai	fixed	converged
study 2.o	{1.1; 1.6}	{0; 0.9}	1 Gounaris-Sakurai	None	converged
study 2.p	{1.1; 1.6}	{0; 0.9}	1 Gounaris-Sakurai	free	converged
study 2.q	{1.1; 1.6}	{0; 0.9}	1 Gounaris-Sakurai	fixed	converged

RMF underestimates the measured intensity. These ($m_{K\pi\pi}$, t') cells also show a very small phase motion of only about $50°$ (see fig. 6.9(d)). The RMF cannot reproduce this small phase motion as the RMF contains only one Breit-Wigner component, which by construction has a phase motion of $180°$. The corresponding Argand diagram explains the low intensity (see fig. 6.9(e)). The Breit-Wigner amplitude forms a circle by construction, but the data does not have a circular shape. This makes it impossible for the fit to reproduce the data. A larger circle radius would result in a higher intensity of the model curve, but the amplitude would be less well described. This pattern happens discontinuously, i.e. one ($m_{K\pi\pi}$, t') cell contains this pattern, while its neighboring cell does not. A possible explanation for this enhanced intentisy is discussed in section 6.2.4.

To further study the peak at about 0.8 GeV/c^2, we performed systematic studies listed in table 6.3. The studies can be divided into groups of three: (i) RMFs without a nonresonant component, (ii) RMFs with a phase-space shaped nonresonant component, and (iii) with a nonresonant component with a free shape parameter. This set of studies was then repeated for different fit ranges in $m_{K\pi\pi}$ and $m_{\pi^-\pi^+}$ and for different parameterizations of the resonant component. The RMFs with a wider $m_{K\pi\pi}$ range yield similar results to the main 2 RMF. Up to $m_{K\pi\pi} \approx 2.0$ GeV/c^2 a clear peak at about 0.8 GeV/c^2 is visible and reproduced well by the RMF. At

(a)

(b)

(c)

(d)

(e)

(f)
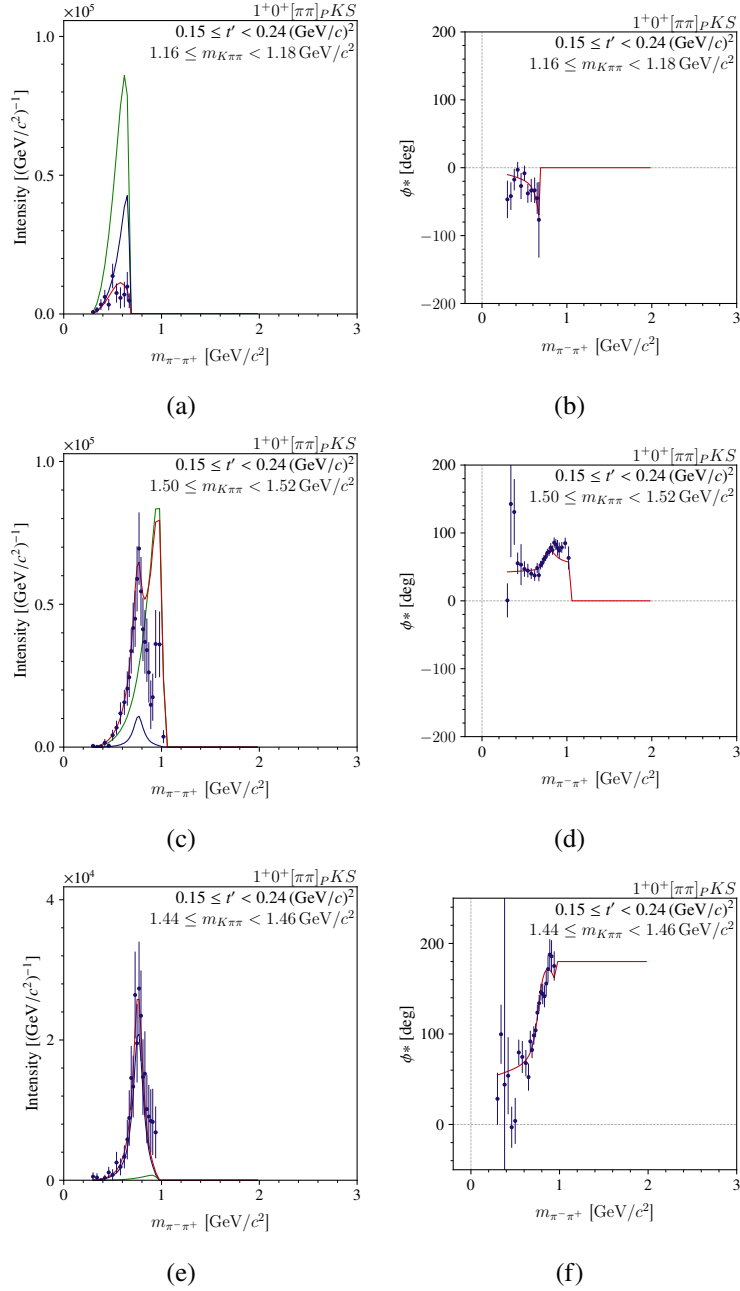
Figure 6.10: Same as fig. 6.1 for study 2.d (see table 6.3) at $m_{K\pi\pi} \approx 1.17\,\text{GeV}/c^2$ (top row), at $m_{K\pi\pi} \approx 1.51\,\text{GeV}/c^2$ (center row) and at $m_{K\pi\pi} \approx 1.45\,\text{GeV}/c^2$ (bottom row) in the second t' bin.

higher $m_{K\pi\pi}$ bins, the noise in the data becomes so large that a clear peak is not visible in the intensity spectrum. In these $m_{K\pi\pi}$ bins, the RMFs yield a model curve of very small intensity.

Table 6.4: Same as table 6.1 for the RMFs with a Gounaris-Sakurai amplitude without angular momentum barrier factors in the $[\pi\pi]_P$ amplitude.

	$m_{K\pi\pi}$ range [GeV/c^2]	$m_{\pi^-\pi^+}$ range [GeV/c^2]	Resonant component	Nonres component	Convergence behavior
study 2.r	{1.1; 1.6}	{0; 0.8}	1 Gounaris-Sakurai	None	converged
study 2.s	{1.1; 1.6}	{0; 0.8}	1 Gounaris-Sakurai	free	converged
study 2.t	{1.1; 1.6}	{0; 0.8}	1 Gounaris-Sakurai	fixed	converged
study 2.u	{1.3; 2.48}	{0; 0.8}	1 Gounaris-Sakurai	None	converged
study 2.v	{1.3; 2.48}	{0; 0.9}	1 Gounaris-Sakurai	None	converged
study 2.w	{1.3; 2.48}	{0; 0.9}	1 Gounaris-Sakurai	free	converged
study 2.x	{1.3; 2.48}	{0; 1.1}	1 Gounaris-Sakurai	None	converged

Also, changing the $m_{\pi^-\pi^+}$ range does not strongly influence the result of the RMFs. The inclusion of a nonresonant component has a significant effect on the RMFs. We observe high destructive interference between the Breit-Wigner and the nonresonant component for $m_{K\pi\pi} \lesssim 1.3\,\text{GeV}/c^2$ (see fig. 6.10(a)), which we do not consider to be a physical solution. At higher $m_{K\pi\pi}$, the RMF develops a second peak that is driven by the nonresonant component. This peak is in the extrapolation of the RMF model since the data points with $m_{\pi^-\pi^+} > 0.9\,\text{GeV}/c^2$ were excluded from the RMF. It is only observed in the $(m_{K\pi\pi}, t')$ cells mentioned above where the phase motion is very small (c.f. figs. 6.9(c) and 6.9(d)). In $(m_{K\pi\pi}, t')$ cells with a phase motion of about $180\,°$ a small contribution of the nonresonant component is observed, and therefore a small interference between the nonresonant and Breit-Wigner component (see figs. 6.10(e) and 6.10(f)).

6.2.2 Models with One Gounaris-Sakurai Component

We also studied the influence of the employed parameterization of the $\rho(770)$ amplitude. To this end, we performed studies where we have used a Gounaris-Sakurai amplitude [30–32] instead of a Breit-Wigner amplitude. The Gounaris-Sakurai amplitude used is of the form

$$\mathcal{D}_{GS}(m_{\pi\pi}) = \frac{m_0\Gamma_0}{m_0^2 - m_{\pi\pi}^2 + f(m_{\pi\pi}) - im_0\Gamma(m_{\pi\pi})} \tag{6.1}$$

where m_0 and Γ_0 are the nominal mass and width of the resonance. The dynamic width is the same used in the Breit-Wigner amplitude (see eq. (3.8)). The Breit-Wigner and Gounaris-Sakurai amplitudes differ only in the parameterization of $f(m_{\pi\pi})$. While the Breit-Wigner amplitude uses $f(m_{\pi\pi}) = 0\,(\text{GeV}/c^2)^2$, the Gounaris-Sakurai amplitude parametrizes it as

$$f_{GS}(m) = \frac{\Gamma_0 m_0^2}{q(m_0^2)^3}[q(m)^2(h(m) - h(m_0^2)) + q(m_0^2)^2 h'(m_0^2)(m_0^2 - m^2)], \tag{6.2}$$

with the two-body break-up momentum $q(m)$ (see eq. (3.9)) and

$$h(m) = \frac{2}{\pi}\frac{q(m)}{m}\ln\left(\frac{m + 2q(m)}{2m_\pi}\right). \tag{6.3}$$

It is important to note that previous measurements used the Gounaris-Sakurai amplitude in two different configurations to measure the resonance parameters of the $\rho(770)$. Some measurements used the Gounaris-Sakurai amplitude without the angular momentum barrier compensation factors and some with. We have tested both configurations. The studies 2.l through 2.q summarized in table 6.3 are RMFs with the angular momentum barrier compensation factors, while the RMFs described in table 6.4 do not.
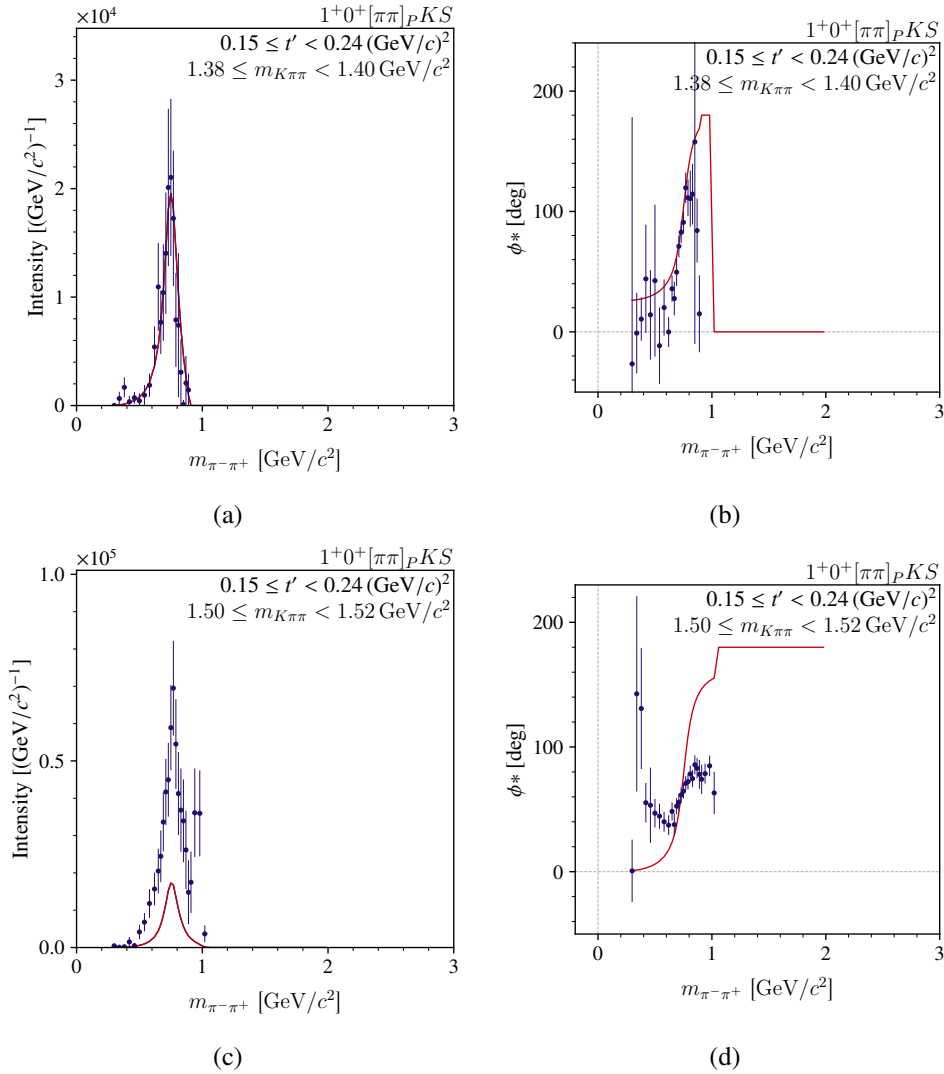
Figure 6.11: Same as fig. 6.1, but for study 2.o (see table 6.3) in the $[\pi\pi]_P$ amplitude. The $(m_{K\pi\pi}, t')$ cells were chosen to be same as in fig. 6.9.

Overall, the RMFs with a Gounaris-Sakurai amplitude give very similar results to those with a Breit-Wigner component. Figure 6.11 shows the same ($m_{K\pi\pi}$, t') cells as fig. 6.9 demonstrating the similarity between the two amplitudes. The model curve of an RMF with a Breit-Wigner component is indistinguishable from that of a Gounaris-Sakurai component. The obtained resonance parameters are also very similar as discussed in section 6.2.4.

6.2.3 Models with Two Breit-Wigner Components

In section 6.2.1, it was discussed that the RMFs with a single resonant component do not describe the data well in some ($m_{K\pi\pi}$, t') cells. Giving the RMF more freedom to model the amplitude, i.e. adding a nonresonant component, improved the amplitude modeling. These RMFs still raise the question whether or not they are very physical, as described in section 6.2.1. In order to model a potential excited resonance an additional Breit-Wigner component was added to the RMFs. Performing RMFs with two Breit-Wigner components may also help to resolve the question of the origin of the enhanced intensity visible in the intensity spectra (see fig. 6.8(b)). In total, 7 RMFs with different $m_{K\pi\pi}$ and $m_{\pi^-\pi^+}$ ranges were performed. All RMFs consisted of two Breit-Wigner components and a free nonresonant component (see table 6.5). All RMF did not converge, thus we did not achieve a stable fit of the enhanced intensity with a Breit-Wigner component. We will still briefly discuss the results of study 2.ag, as they are used to calculate the significance of the resonant component that describes the enhanced intensity. The peak at about $0.8\,\text{GeV}/c^2$ is mostly described by the $\rho(770)$ component (see fig. 6.12). The second Breit-Wigner and the nonresonant component appear to contribute little to the
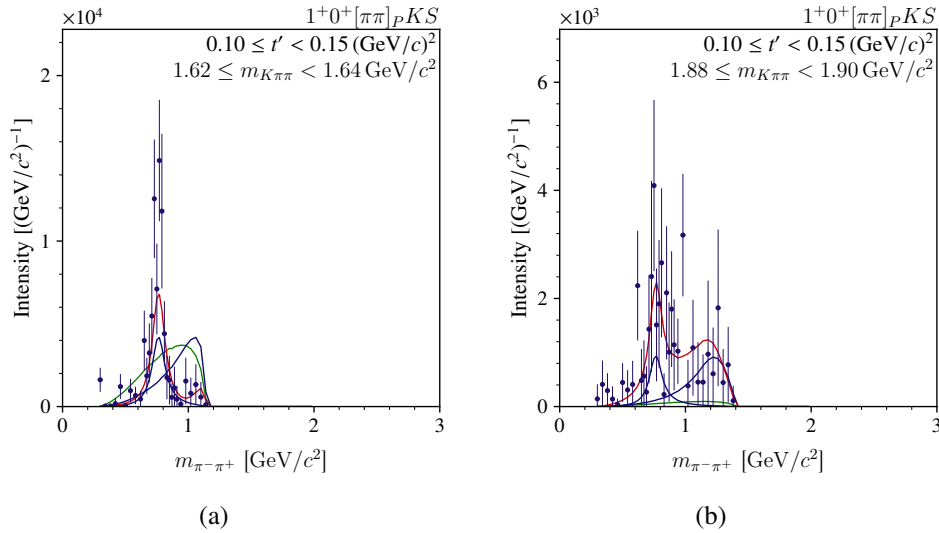
Figure 6.12: Same as fig. 6.1, but for the intensity of the $[\pi\pi]_P$ amplitude in the $1^+0^+[\pi\pi]_P KS$ wave at $m_{K\pi\pi} \approx 1.63\,\text{GeV}/c^2$ (left) and at $m_{K\pi\pi} \approx 1.89\,\text{GeV}/c^2$ (right) in the lowest t' bin. The curves show the results of study 2.ag

Table 6.5: Same as in table 6.1 for the two Breit-Wigner component RMFs in the $[\pi\pi]_P$ amplitude. Note that in studies 2.y to 2.ac, all availabe $m_{K^-\pi^+}$ bins in a $m_{K\pi\pi}$ cell are fitted.

	$m_{K\pi\pi}$ range [GeV/c^2]	$m_{\pi^-\pi^+}$ range [GeV/c^2]	Resonant component	Nonres component	Convergence behavior
study 2.y	{1.1; 1.8}	{0; 1.4}	2 Breit-Wigner	free	not converged
study 2.z	{1.4; 1.8}	{0; 1.4}	2 Breit-Wigner	free	not converged
study 2.aa	{1.1; 1.8}	{0; 1.4}	2 Breit-Wigner	free	not converged
study 2.ab	{1.2; 1.8}	{0; 1.4}	2 Breit-Wigner	free	not converged
study 2.ac	{1.4; 1.8}	{0; 1.4}	2 Breit-Wigner	free	not converged
study 2.ad	{1.1; 2.48}	{0; 1.4}	2 Breit-Wigner	free	not converged
study 2.ae	{1.2; 2.48}	{0; 1.4}	2 Breit-Wigner	free	not converged
study 2.af	{1.1; 2.48}	{0; 3.0}	2 Breit-Wigner	free	not converged
study 2.ag	{1.2; 2.48}	{0; 3.0}	2 Breit-Wigner	free	not converged

peak at about $0.8\,\text{GeV}/c^2$, as expected. They are used by the RMF to describe the enhanced intensity. Some ($m_{K\pi\pi}$, t') cells show destructive interference between these two components (see fig. 6.12(a)), while other cells show a second peak in the intensity spectrum driven by the second Breit-Wigner component with overall a very small nonresonant component contribution (see fig. 6.12(b)).

6.2.4 Discussion

The main 2 RMF with a single Breit-Wigner component (see section 6.2.1) yielded a mass of $m = 766\,\text{MeV}/c^2$ and a width of $\Gamma = 138\,\text{MeV}/c^2$[3]. The PDG lists the neutral $\rho(770)$ determined for "other reactions" with a mass of $m_{\text{PDG, 770}} = (769.0 \pm 0.9)\,\text{MeV}/c^2$ and a width of $\Gamma_{\text{PDG, 770}} = (150.9 \pm 1.7)\,\text{MeV}/c^2$ [2]. The resonance parameters determined in the main 2 RMF are both slighlty smaller than the PDG average. Overall, the systematic studies gave very similar results, all in a close range, except for three outliers from studies 2.c, 2.f, and 2.l, which yielded a larger mass of $m > 775\,\text{MeV}/c^2$ (see fig. 6.13). The Breit-Wigner and Gounaris-Sakurai amplitudes with angular momentum barrier compensation factors not only give very similar model curves, but also similar resonance parameters. They both describe the $[\pi\pi]_P$ amplitude equally well. The resonance parameters of the $\rho(770)$ Breit-Wigner component in the two Breit-Wigner component fits are stable, although the RMFs did not converge. Overall, the peak at about $0.8\,\text{GeV}/c^2$ is well described in all performed RMFs and very stable. This suggests a clear $\rho(770)$ signal in our data. However, it must be kept in mind that not a complete set of systematic studies have been performed yet and that the origin of the enhanced intensity in some ($m_{K\pi\pi}$, t') cells is unclear.

---

[3]We give the results rounded to $1\,\text{MeV}/c^2$ without uncertainties, because the systematic uncertainties are not determined yet, as discussed in section 4.4.
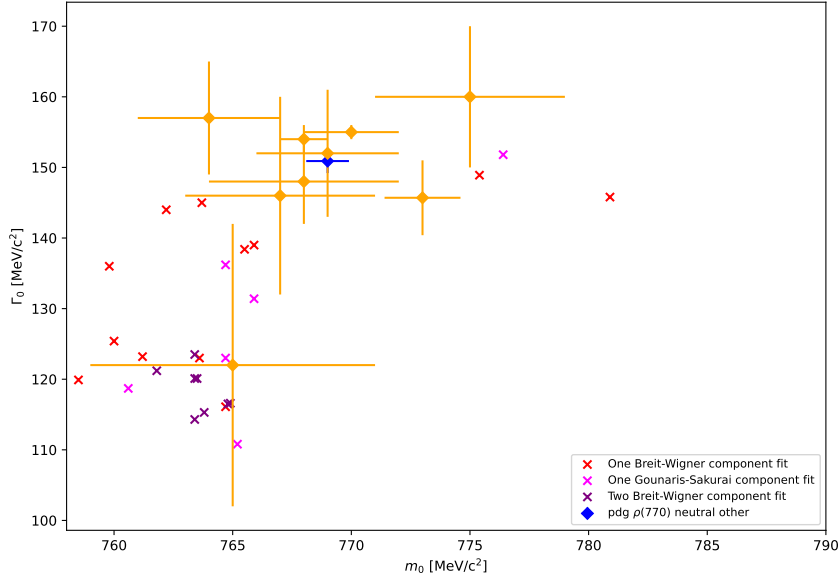
Figure 6.13: Same as fig. 6.6, but for the RMFs of the $\rho(770)$ in the $[\pi\pi]_P$ amplitude. As reference the PDG average and its previous 9 measurements [4] are included [2].

For better comparability, we compared the Gounaris-Sakurai amplitude with angular momentum barrier compensation factors to the Breit-Wigner amplitude, since the Breit-Wigner amplitude parameterization contains these compensation factors. Due to the small uncertainty of the $\rho(770)$ parameters, the results of RMFs with a Gounaris-Sakurai amplitude with angular momentum barrier compensation factors are compared to results that also use these compensation factors. The measurements in the PDG average "neutral only, e^+e^-", did not use these compensation factors, thus we can compare our results from the RMFs of table 6.4 we these values. Since the resonance parameters obtained in our fits have a large spread, only the upper and lower limits of our resonance parameters are presented. The RMFs yielded masses of $769\,\text{MeV}/c^2 \leq m \leq 794\,\text{MeV}/c^2$ and widths of $111\,\text{MeV}/c^2 \leq \Gamma \leq 151\,\text{MeV}/c^2$. We could not find any systematic within the values and their fit environment. The PDG calculated an average mass of $m_{\text{PDG},770,e^+e^-} = (775.26 \pm 0.23)\,\text{MeV}/c^2$ and a width of $\Gamma_{\text{PDG},770,e^+e^-} = (147.4 \pm 0.7)\,\text{MeV}/c^2$ [2]. Overall, our results for the $\rho(770)$ are comparable to the PDG average. Since both Gounaris-Sakurai amplitudes with and without the angular-momentum barrier compensation factors yield similar resonance parameters, the question remains whether one of the two parameterizations performs better than the other. To this, we cannot give a clear answer. The Gounaris-Sakurai amplitude with and without the angular momentum barrier compensation factors performed equally well on average.

---

[4]Only values with both a mass and width from the PDG list "neutral only, other reaction" was used.
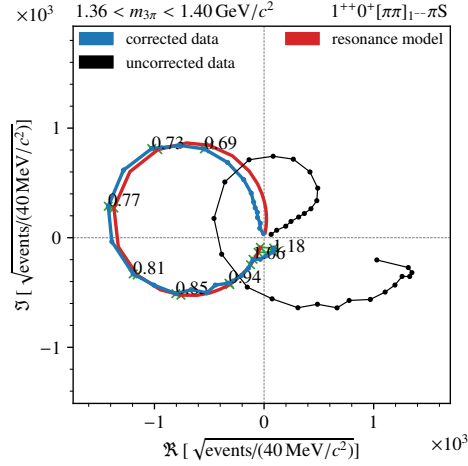
Figure 6.14: Argand diagram of the $1^{++}0^+[\pi\pi]_{1^{--}}\pi S$ wave at $m_{3\pi} \approx 1.38\,\mathrm{GeV}/c^2$, which is affected by zero modes. The black data points show the measured amplitude without any corrections. The blue data points show the amplitude with a correction for the zero modes. And red is the RMF of a single relativistic Breit-Wigner [33].

With the two Breit-Wigner component fits, we searched for possible signals from an excited ρ state. The RMFs do not provide resonance components and there is no known excited ρ state in this mass range. Using Wilks' theorem, we calculated a significance of 26.41 σ, which means that the second Breit-Wigner component in the RMF is not of statistical origin. However, its true nature remains hidden. The structure is most likely due to some analysis artifacts, maybe also related to zero-mode-like effects.

As discussed in section 3.3, our amplitudes could be affected by zero-mode-like effects. The Argand diagram of the amplitude in $(m_{K\pi\pi}, t')$ cells exhibiting the enhanced intensity looks similar to Argand diagrams known from the $\pi\pi\pi$ analysis, which are affected by zero-modes. For reference, such an Argand diagram is shown in fig. 6.14 (see black data points). In addition, the $[\pi\pi]_S$ amplitude, which is a partner wave of the $[\pi\pi]_P$ amplitude, is not perfectly modeled because it is not well known. These two points suggest that our amplitude may be affected by the zero-mode-like effects. This has to be investigated in further systematic studies of the freed-isobar fit.

The $[\pi\pi]_P$ and $[K\pi]_P$ amplitudes contain well established ground states of the resonances that have been used as standard candles to prove the freed-isobar method. So far, the ground states have always appeared as clear signals in the amplitude as expected and were reproduced well by the RMFs. This means that the freed-isobar method works in general, allowing us to study excited states and not well known amplitudes. Thereby, we not only valiate the conventional PWD in the freed-isobar analysis, but can also measure the amplitude of states that need further confirmation and are in the focus of many current studies such as the $[K\pi]_S$ amplitude. However, also possible analysis artifacts were discovered to contribute in our analysis.

6.3 $[K\pi]_D$ **Amplitude**

The $[K\pi]_D$ amplitude represents the $K^-\pi^+$ subsystem where both particles are in a D-wave configuration. We study this amplitude in the $2^-0^+[K\pi]_D\pi S$ wave. In this subsystem we expect K_2^* resonances with quantum numbers $J^P = 2^+$, for which the PDG lists the $K_2^*(1430)$ and $K_2^*(1980)$. Figure 6.15 shows the intensity spectrum of a representative $(m_{K\pi\pi}, t')$ cells of the $[K\pi]_D$ amplitude. In the spectrum two peaks at about $1.4\,\text{GeV}/c^2$ and at about $2.0\,\text{GeV}/c^2$ are visible. The peak at about $1.4\,\text{GeV}/c^2$ could correspond to the well-known $K_2^*(1430)$. The peak at about $2.0\,\text{GeV}/c^2$ is interesting to study because the PDG lists only the $K_2^*(1980)$, but quark-model calculations of ref. [34] suggest two excited states in this mass range.

6.3.1 Models with One Breit-Wigner Component

To study the peak at about $1.4\,\text{GeV}/c^2$, we include only the region $0 < m_{K^-\pi^+} < 1.6\,\text{GeV}/c^2$ and all possible $(m_{K\pi\pi}, t')$ cells [5] in an RMF with a single Breit-Wigner component. With these boundaries the peak at about $2.0\,\text{GeV}/c^2$ is excluded from the fit. The RMF reproduces well the intensity spectra for $1.6 \lesssim m_{K\pi\pi} \lesssim 2.4\,\text{GeV}/c^2$ (see fig. 6.16(a)). The corresponding phase plot exhibits large statistical fluctuations (see fig. 6.16(b)). Starting at around $1.2\,\text{GeV}/c^2$, a clear rising phase motion is observed. This phase is well reproduced by the RMF. For intensity spectra outside the $1.6 \lesssim m_{K\pi\pi} \lesssim 2.4\,\text{GeV}/c^2$ range, the RMF underestimates the intensity of the data points (see fig. 6.16(c)). Figure 6.16(d) shows that this happens due to the shape of the amplitude. To increase the intensity in that $(m_{K\pi\pi}, t')$ cell the model curve circle would have to have a larger radius, resulting in less well described data.
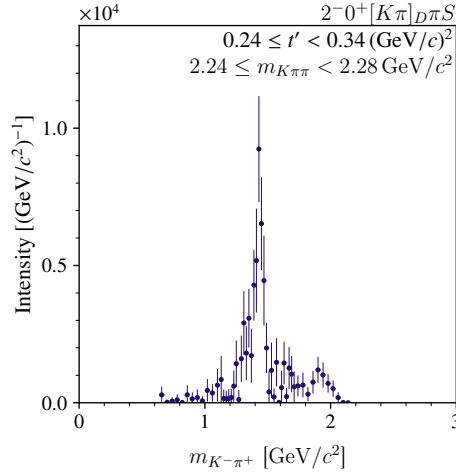
Figure 6.15: Same as fig. 6.1 for the $[K\pi]_D$ amplitude. The plot showcases the two peaks at $1.4\,\text{GeV}/c^2$ and $2.0\,\text{GeV}/c^2$.

---

[5] $1.4 \leq m_{K\pi\pi} \leq 3.0\,\text{GeV}/c^2$
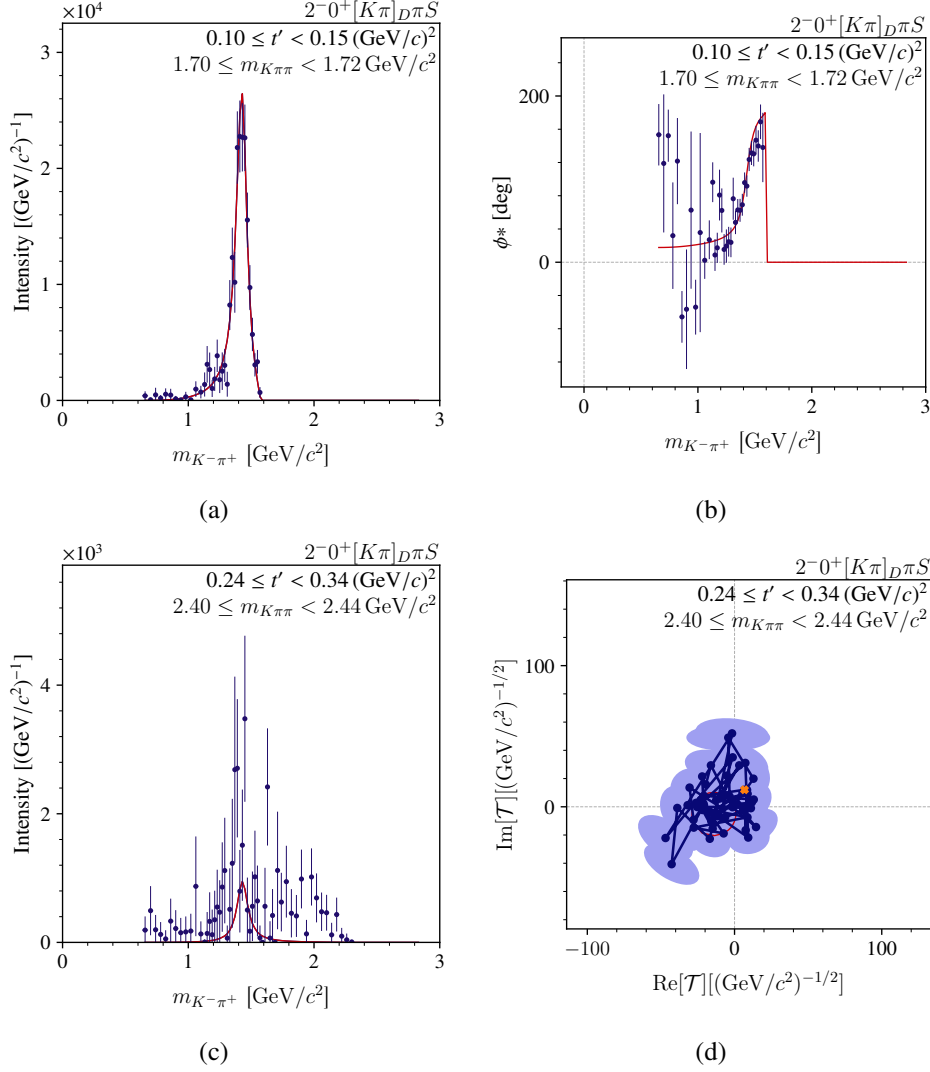
Figure 6.16: Same as fig. 6.9, but showing the intensity (left column), phase (upper right) and Argand (lower right) diagram of the $2^-0^+[K\pi]_D\pi S$ wave at $m_{K\pi\pi} \approx 1.71\,\text{GeV}/c^2$ (top row) and $m_{K\pi\pi} \approx 2.41\,\text{GeV}/c^2$ (bottom row) in the third t' bin.

Also in the $[K\pi]_D$ amplitude, we study the stability of the RMF in several studies (see Table 6.6). Three different types of systematics have been studied: different $m_{K\pi\pi}$ fit ranges, different $m_{K^-\pi^+}$ fit ranges, and contributions from a nonresonant component, whose shape parameter was either fixed to zero or given as a free parameter. Varying the $m_{K\pi\pi}$ range does not strongly influence the results. The resulting resonance parameters are very close to the main 3.1 fit (see section 6.3.3) and the intensity spectra are reproduced equally well. The only difference from the RMF is the absence of the high $m_{K\pi\pi}$ cells in the fit. Therefore, all $(m_{K\pi\pi}, t')$ cells are well reproduced by this RMF as long as $m_{K^-\pi^+} \lesssim 1.6\,\text{GeV}/c^2$. Similarly different $m_{K^-\pi^+}$

Table 6.6: Same as table 6.1 for one Breit-Wigner component fits for $[K\pi]_D$ amplitude.

	$m_{K\pi\pi}$ range [GeV/c^2]	$m_{K^-\pi^+}$ range [GeV/c^2]	Resonant component	Nonres component	Convergence behavior
main 3.1	{1.4; 3.0}	{0.0; 1.6}	1 Breit-Wigner	None	converged
study 3.a	{1.4; 3.0}	{0.0; 1.8}	1 Breit-Wigner	None	converged
study 3.b	{1.4; 3.0}	{0.0; 1.6}	1 Breit-Wigner	free	converged
study 3.c	{1.4; 3.0}	{0.0; 1.8}	1 Breit-Wigner	free	converged
study 3.d	{1.4; 3.0}	{0.0; 1.6}	1 Breit-Wigner	fixed	converged
study 3.e	{1.4; 3.0}	{0.0; 1.8}	1 Breit-Wigner	fixed	converged
study 3.f	{1.4; 2.2}	{0.0; 1.6}	1 Breit-Wigner	None	converged
study 3.g	{1.4; 2.2}	{0.0; 1.8}	1 Breit-Wigner	None	converged
study 3.h	{1.4; 2.2}	{0.0; 1.6}	1 Breit-Wigner	fixed	converged
study 3.i	{1.4; 2.2}	{0.0; 1.8}	1 Breit-Wigner	fixed	converged
study 3.j	{1.4; 2.2}	{0.0; 1.6}	1 Breit-Wigner	free	converged
study 3.k	{1.4; 2.2}	{0.0; 1.8}	1 Breit-Wigner	free	converged

(a) (b)
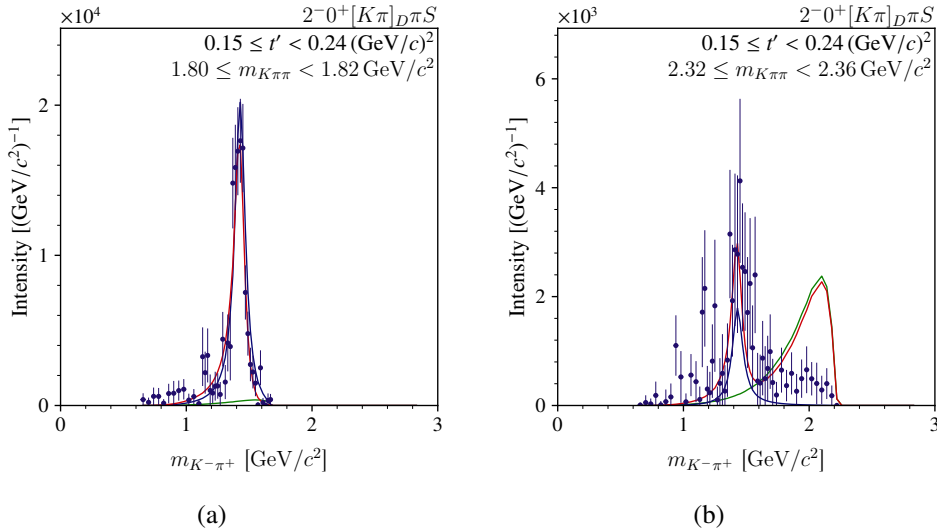
Figure 6.17: Same as fig. 6.1, but for intensity of model 3.b in the $[K\pi]_D$ amplitude. The left side shows the results of $m_{K\pi\pi} \approx 1.81 \, \text{GeV}/c^2$ in the lowest t' bin. The right side shows the results of $m_{K\pi\pi} \approx 2.34 \, \text{GeV}/c^2$ in the lowest t' bin.

ranges do not lead to significant changes. Figure 6.17 shows the results from study 3.b. All studies with a nonresonant component yielded similar results. The RMF reproduced the data well for $1.6 \lesssim m_{K\pi\pi} \lesssim 2.2 \, \text{GeV}/c^2$ (see fig. 6.17(a)). The Breit-Wigner component is the main contributor to the model curve, the nonresonant contribution is negligible. Figure 6.17(b) shows an example of an intensity spectrum outside the $1.6 \lesssim m_{K\pi\pi} \lesssim 2.2 \, \text{GeV}/c^2$ region. Around

Table 6.7: Same as table 6.1 for two Breit-Wigner component fits for $[K\pi]_D$ amplitude. Note that in studies 3.k, all availabe $m_{K^-\pi^+}$ bins in a $m_{K\pi\pi}$ cell are fitted.

	$m_{K\pi\pi}$ range [GeV/c^2]	$m_{K^-\pi^+}$ range [GeV/c^2]	Resonant component	Nonres component	Convergence behavior
main 3.2	{1.7; 2.48}	{0.0; 2.1}	2 Breit-Wigner	free	converged
study 3.k	{1.7; 2.48}	{0.0; 2.6}	2 Breit-Wigner	free	converged
study 3.l	{1.6; 2.8}	{0.0; 2.1}	2 Breit-Wigner	free	converged
study 3.m	{1.6; 2.8}	{0.0; 2.6}	2 Breit-Wigner	free	converged
study 3.n	{2.0; 2.8}	{0.0; 2.1}	2 Breit-Wigner	free	converged
study 3.o	{2.0; 2.8}	{0.0; 2.6}	2 Breit-Wigner	free	converged

the $1.4\,\text{GeV}/c^2$ peak region, there is only a small nonresonant contribution. At higher $m_{K^-\pi^+}$ the nonresonant curve creates a second peak in the model curve, which does not reproduce the measured intensity spectrum. This second peak stems from an extrapolation of the data points, since the $m_{K^-\pi^+}$ region of said peak is not included in the fit range. The $m_{K^-\pi^+}$ region included in this RMF is still well reproduced.

6.3.2 Models with Two Breit-Wigner Components

To study the peak at about $2.0\,\text{GeV}/c^2$, we include the region $1.7 < m_{K\pi\pi} < 2.48\,\text{GeV}/c^2$ and $0.0 < m_{K^-\pi^+} < 2.1\,\text{GeV}/c^2$ in an RMF (main 3.2 in table 6.7) with two Breit-Wigner components and a nonresonant component[6]. Also this RMF reproduces the peak at about $1.4\,\text{GeV}/c^2$ well (see fig. 6.18(a)). Around this peak, the nonresonant component contributes little to the model curve. The peak at about $2.0\,\text{GeV}/c^2$ is mostly reproduced by the nonresonant component. In fact, the intensity of the second Breit-Wigner component is so small that it is not visible in the shown intensity spectrum. A very different picture is shown in fig. 6.18(c), where there is overall a very low nonresonant contribution. The structure at about $1.4\,\text{GeV}/c^2$ is still very well reproduced, and the main component contributing to the structure at about $2.0\,\text{GeV}/c^2$ is the second Breit-Wigner component. In the $m_{K\pi\pi}$ bin shown in fig. 6.18(b), the phase plot of the $[K\pi]_D$ amplitude does not show a clear rise in the $m_{K^-\pi^+}$ region of the second peak. Figure 6.18(d) shows a clear rising phase in the $m_{K^-\pi^+}$ region of the second peak. The RMF with the second Breit-Wigner component reproduces this rising phase well.

To study the stability of the two Breit-Wigner component fits, 5 systematic studies were performed. First, the presence of a nonresonant component were investigated. Models without a nonresonant component failed to converge and yielded resonance parameters that hit their bounds. The minima found by the fit are not of physical nature and therefore we did not consider these results. Also, the effect of different $m_{K\pi\pi}$ fit ranges were investigated with studies 3.l and 3.n. These RMFs result large destructive interferences between the Breit-Wigner

---

[6]These $m_{K\pi\pi}$ and $m_{K^-\pi^+}$ ranges were chosen as the main 3.2 fit as it had the lowest reduced χ^2-value of all tried RMFs.

(a)

(b)

(c)

(d)
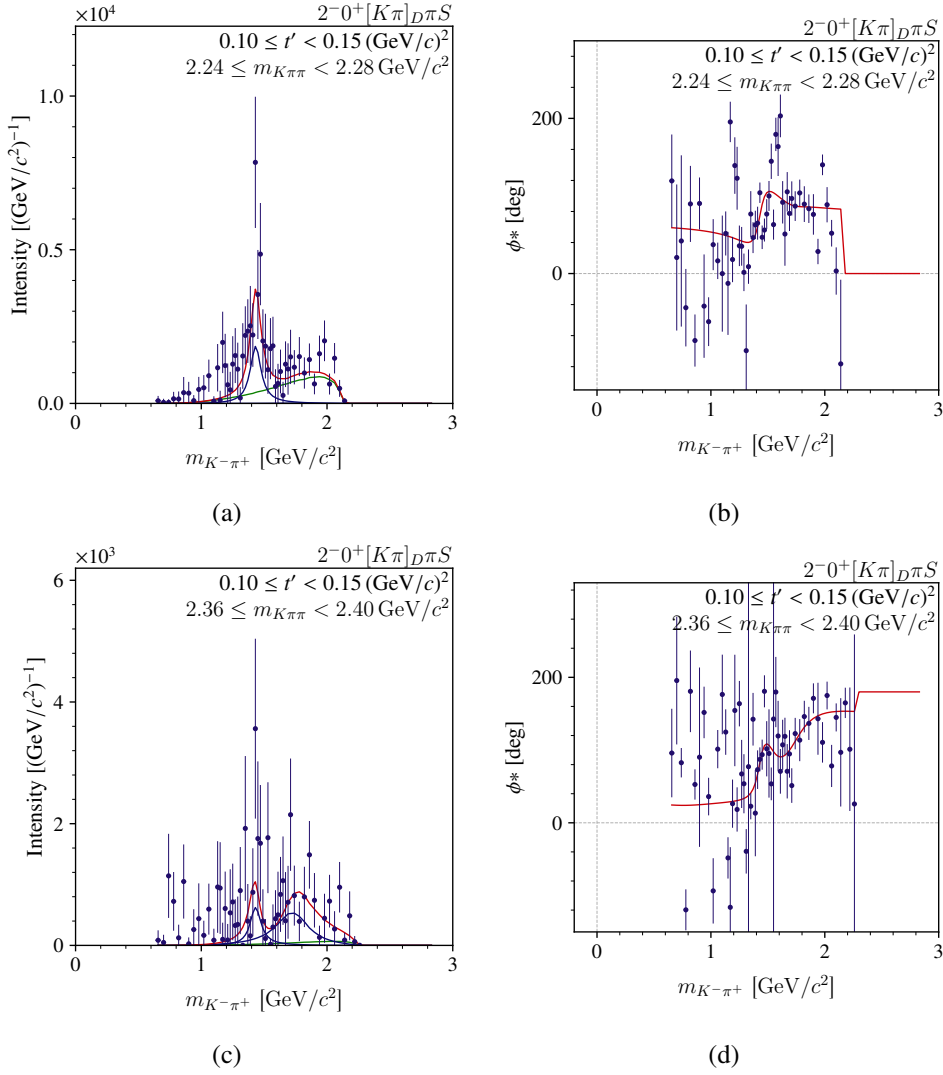
Figure 6.18: Same as in fig. 6.1. Intensitiy (left) and phase (right) plots at $m_{K\pi\pi} \approx 2.26\,\mathrm{GeV}/c^2$ (top row) and $m_{K\pi\pi} \approx 2.38\,\mathrm{GeV}/c^2$ (bottom row) in the lowest t' bin of main 3.2 in $[K\pi]_D$ amplitude.

and nonresonant components. The individual components had an intensity 100 times higher than the resulting total model curve. We do not consider such large destructive interferences physical. Hence, these solutions are not further discussed. Finally, the effect of a higher fit range in $m_{K^-\pi^+}$ was studied with studies 3.k, 3.m and 3.o. In study 3.k, the model curve is similar to all other RMFs. Models 3.m and 3.o yielded very broad structures for the peak at about $2.0\,\mathrm{GeV}/c^2$. This is discussed further in section 6.3.3.

6.3.3 Discussion

The peak at about $1.4\,\mathrm{GeV}/c^2$ is so dominant in the $(m_{K\pi\pi}\,,\,t')$ cells that our data contain a clear $K_2^*(1430)^0$ signal. The one Breit-Wigner component RMF yielded a mass of $m = 1430\,\mathrm{MeV}/c^2$ and a width of $\Gamma = 106\,\mathrm{MeV}/c^{2\,27}$ for the $K_2^*(1430)^0$. The PDG average lists the $K_2^*(1430)^0$ at a mass of $m_{\mathrm{PDG,1430,neutral}} = (1432.4 \pm 1.3)\,\mathrm{MeV}/c^2$ and a width of $\Gamma_{\mathrm{PDG,1430,neutral}} = (109 \pm 5)\,\mathrm{MeV}/c^2$ [2]. Our estimate agrees well with previous measurements and with the PDG average (see fig. 6.19). From the stability of the $K_2^*(1430)^0$ in all studies we conclude that the fit is very stable, thus confirming the resonance parameters from the main 3.1 RMF. However, it is important to keep in mind that the systematics of the freed-isobar fits have not yet been determined.

The $K^-\pi^-\pi^+$ sample is particularly interesting because it allows us to study the $K_2^*(1430)$
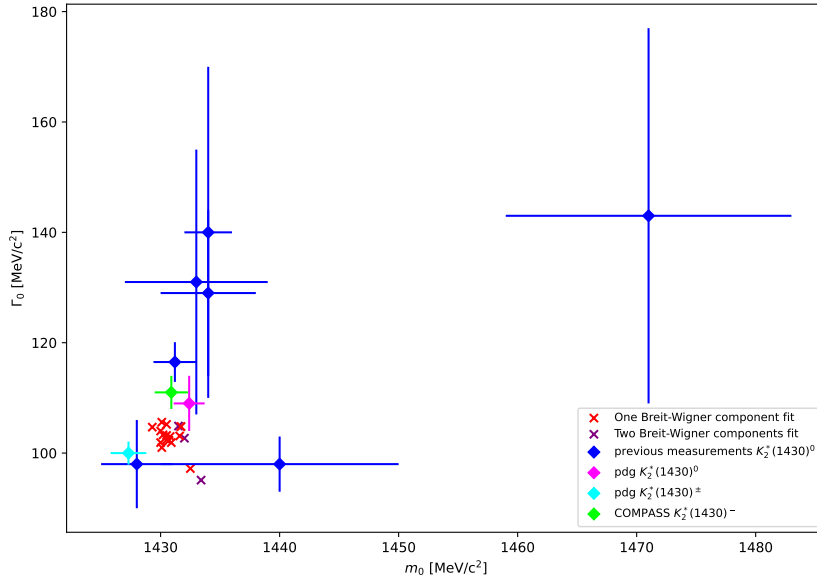
Figure 6.19: Same as fig. 6.6. The results from this analysis for the neutral $K_2^*(1430)^0$ are shown by the red and violet crosses for the one and two Breit-Wigner fits, respectively. The blue diamond shaped data points represent the resonance parameters from other experiments. The PDG [2] average for the $K_2^*(1430)^0$ is shown in magenta, its last 7 measurements in blue. The PDG average for the charged $K_2^*(1430)^\pm$ is shown in cyan. The COMPASS value, determined in the three body-analysis, in lime [35].

---

[7]We give the results rounded to $1\,\mathrm{MeV}/c^2$ without uncertainties, because the systematic uncertainties are not determined yet, as discussed in section 4.4.
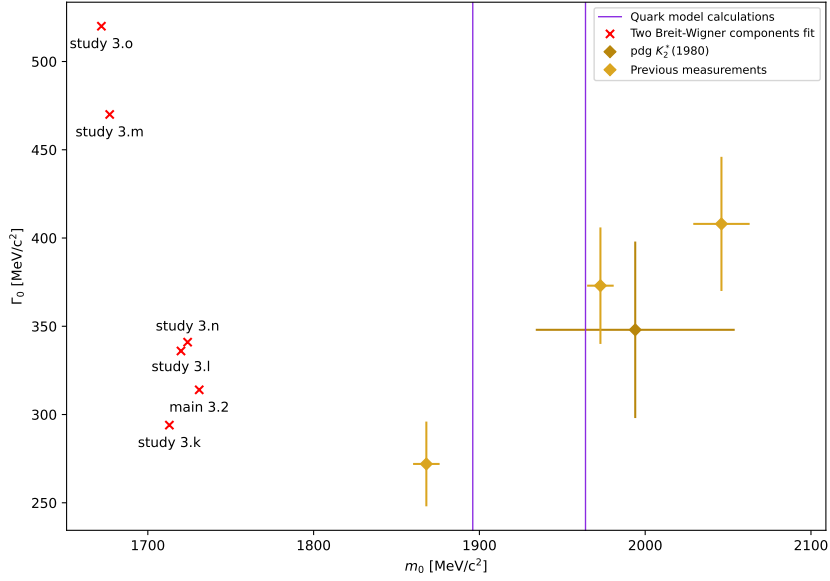
Figure 6.20: Same as fig. 6.19 for the peak at about $2.0\,\text{GeV}/c^2$. The PDG average for the $K_2^*(1980)$, their previous measurements and quark-model predictions are included [2, 34].

in its neutral state in the $K^-\pi^+$ subsystem and in its charged states in the $K^-\pi^-\pi^+$ system. The PDG lists different resonance parameters for the charged and uncharged states. The $K_2^*(1430)^\pm$ is listed with a mass of $m_{\text{PDG,1430,charged}} = (1427.3 \pm 1.5)\,\text{MeV}/c^2$ and a width of $\Gamma_{\text{PDG,1430,charged}} = (100.0 \pm 2.1)\,\text{MeV}/c^2$ [2]. In the COMPASS three-body analysis a mass of $m_{\text{COMPASS,1430,charged}} = (1430.9 \pm 1.4)\,\text{MeV}/c^2$ and a width of $\Gamma_{\text{PDG,1430,charged}} = (111 \pm 3)\,\text{MeV}/c^2$ was determined for the charged state [35]. These parameters are similar to the PDG average of the neutral state, not the charged state. Our resonance parameters are also close to the PDG average of the nuetral state as well as to the COMPASS three-body measurement. This does not confirm the mass difference that the PDG states for the $K_2^*(1430)$.

The main 3.2 two Breit-Wigner component RMF yielded a mass of $m = 1713\,\text{MeV}/c^2$ and a width of $\Gamma = 294\,\text{MeV}/c^2$ for the higher-lying resonance component (see fig. 6.20). The only known excited state with quantum numbers $J^P = 2^+$ is the $K_2^*(1980)$ with a mass of $m_{\text{PDG,1980,neutral}} = 1994^{+60}_{-50}\,\text{MeV}/c^2$ and a width of $\Gamma_{\text{PDG,1430,neutral}} = 348^{+50}_{-30}\,\text{MeV}/c^2$ [2]. Our RMF yielded a mass much smaller than the PDG average. Using Wilks' theorem, a significance of $20.46\,\sigma$ is determined for the second Breit-Wigner component. Thus, this component is statistically significant and does not describe only statistical fluctuation. However the RMFs are not giving very consistent results. The main 3.2 RMF and models 3.k, 3.l, 3.n gave close resonance parameters, while models 3.m and 3.o yield much larger widths. Hence, we cannot

57

clearly state that our data contain an excited K_2^* signal. Quark-model calculations suggest two exited states with quantum numbers $J^P = 2^+$, which could explain the difference between our measurement and the previous measurements. The first predicted state is the $n^{2S+1}L_J = 2^3P_2$[8] with a mass at about $m_{2^3P_2} = 1896\,\text{MeV}/c^2$ and the second state is the 1^3F_2 with a mass at about $m_{1^3F_2} = 1964\,\text{MeV}/c^2$ [34]. The PDG listing of the $K_2^*(1980)$ agrees best with the 1^3F_2 state. Although our analysis yielded a mass much smaller than the predicted mass value for the 2^3P_2, our signal could originate from this state. Further systematic studies of the freed-isobar fit and the RMF are needed to clarify the origin of this peak.

---

[8]n is the principal quantum number, S is the total spin, L refers to the angular momentum of the $q\bar{q}$ system and J is the total angular momentum of the $q\bar{q}$ system.

6.4 [Kπ]$_S$ Amplitude

The $[K\pi]_S$ amplitude represents the $K^-\pi^+$ subsystem where both particles are in an S-wave configuration. We study this amplitude in the $0^-0^+[K\pi]_S\pi S$ wave. In this subsystem we expect K_0^* resonances with quantum numbers $J^P = 0^+$, for which the PDG lists the $\kappa/K_0^*(700)$, $K_0^*(1430)$ and $K_0^*(1950)$. The analysis of the $K_0^*(700)$ is of particular interest, since this state cannot be assigned to a pure $q\bar{q}$ state [36]. The $K_0^*(700)$ resonance is a very broad state with a width at about $\Gamma \approx 500\,\text{MeV}/c^2$. This resonance overlaps with the excited $K_0^*(1430)$ state, which makes the modeling of the $[K\pi]_S$ amplitude challenging. We observe two peaks in the intensity spectra of the $[K\pi]_S$ amplitude (see fig. 6.21). The first very broad peak is at about $1.2\,\text{GeV}/c^2$. It covers the mass region of both the $K_0^*(700)$ and the $K_0^*(1430)$. The second peak is at about $1.9\,\text{GeV}/c^2$ and could correspond to the $K_0^*(1950)$ state. In this section we describe RMFs to the $[K\pi]_S$ amplitude using four different parameterizations: Breit-Wigner amplitudes, LASS amplitude, Palano-Pennington amplitude and Pelaez-Rodas amplitude. These amplitudes except the Breit-Wigner amplitude are special parameterizations for the $[K\pi]_S$ amplitude. Most of them have so many free parameters that we cannot fit all of them, thus we will measure resonance parameters only for parameterizations with few parameters. Also not all parameterizations cover the entire $m_{K^-\pi^+}$ range. To model also a possible $K_0^*(1950)$ with these, an additional Breit-Wigner component was added. In section 6.4.5, all the parameterizations are compared in their ability to describe the measured $[K\pi]_S$ amplitude to find the best parameterization for the $[K\pi]_S$ amplitude.
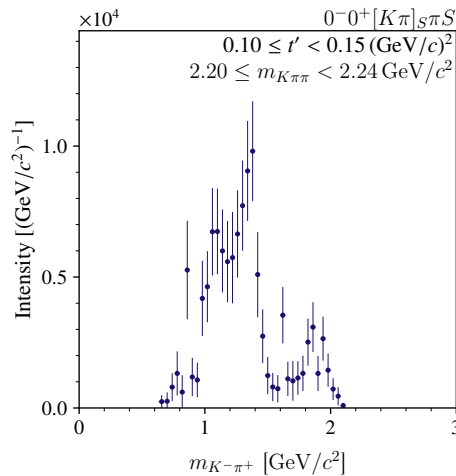
Figure 6.21: Same as fig. 6.1, but for the $[K\pi]_S$ amplitude in the $0^-0^+[K\pi]_S\pi S$ wave in a selected $(m_{K\pi\pi}, t')$ cell.

Table 6.8: Same as table 6.1 for two and three Breit-Wigner component fits for $[K\pi]_S$ amplitude. Note that in studies 4.a, 4.c, 4.e, 4.f, 4.g and 4.h, all availabe $m_{K^-\pi^+}$ bins in a $m_{K\pi\pi}$ cell are fitted.

	$m_{K\pi\pi}$ range [GeV/c^2]	$m_{K^-\pi^+}$ range [GeV/c^2]	Resonant component	Nonres component	Convergence behavior
study 4.a	{1.60; 2.36}	{0.0; 10.0}	2 Breit-Wigner	None	not converged
study 4.b	{1.60; 2.20}	{0.0; 1.8}	2 Breit-Wigner	None	not converged
study 4.c	{1.60; 2.36}	{0.0; 10.0}	2 Breit-Wigner	free	not converged
study 4.d	{1.60; 2.20}	{0.0; 1.8}	2 Breit-Wigner	free	not converged
study 4.e	{1.60; 2.40}	{0.0; 10.0}	3 Breit-Wigner	None	not converged
study 4.f	{1.60; 2.40}	{0.0; 10.0}	3 Breit-Wigner	free	not converged
study 4.g	{1.60; 2.20}	{0.0; 10.0}	3 Breit-Wigner	None	not converged
study 4.h	{1.60; 2.20}	{0.0; 10.0}	3 Breit-Wigner	free	not converged

6.4.1 Parameterization with Breit-Wigner Components

In order to test whether an RMF with Breit-Wigner components could possibly describe the $[K\pi]_S$ amplitude, models with two and three Breit-Wigner components were fit to the data (see table 6.8). All RMFs did not converge. Models consisting of only two Breit-Wigner components are not able to represent well the shape of the intensity spectrum in any ($m_{K\pi\pi}$, t') cell (see fig. 6.22(a)). For example, the total model curve underestimates the intensity of the data for $m_{K^-\pi^+} \approx 1.1\,\text{GeV}/c^2$. For $m_{K^-\pi^+} \approx 1.5\,\text{GeV}/c^2$ the total model curve yields a peak dominated by the $K_0^*(1430)$ Breit-Wigner component. The Breit-Wigner amplitude is an approximation for narrow states. Since the $K_0^*(700)$ state is not very narrow, a Breit-Wigner amplitude alone is not able to describe the intensity spectra of the $[K\pi]_S$ amplitude. Although the RMF does not converge and the intensity spectra are poorly reproduced, the phase motion of the system is well modeled by the total model curve (see fig. 6.22(b)). The inclusion of a nonresonant component results in the total model curve describing the intensity spectrum much better (see fig. 6.22(c)). The RMF uses interference between the Breit-Wigner component and the nonresonant component at the lower $m_{K^-\pi^+}$, to better describe the low $m_{K^-\pi^+}$ shoulder of the peak at about $1.4\,\text{GeV}/c^2$. The RMF yields a Breit-Wigner component similar to that in the model without the nonresonant component. As expected, the addition of the nonresonant component also leads to a slightly better description of the phase spectrum (see fig. 6.22(d)).

As no RMF consisting of two Breit-Wigner components converged, we decided to test RMFs with three Breit-Wigner components, aiming for more stable results. None of these studies converged either. The $m_{K\pi\pi} \lesssim 2.0\,\text{GeV}/c^2$ region does not exhibit a clear second peak at about $1.9\,\text{GeV}/c^2$ and is similar to those in fig. 6.22(a). The third Breit-Wigner component at the highest $m_{K^-\pi^+}$ does not contribute strongly for $m_{K\pi\pi} \lesssim 2.0\,\text{GeV}/c^2$. For $m_{K\pi\pi} \gtrsim 2.0\,\text{GeV}/c^2$ the model curve describes the intensity spectrum very well (see fig. 6.23(a)). The peak at about $1.9\,\text{GeV}/c^2$ is mostly reproduced by the third Breit-Wigner component. The corresponding
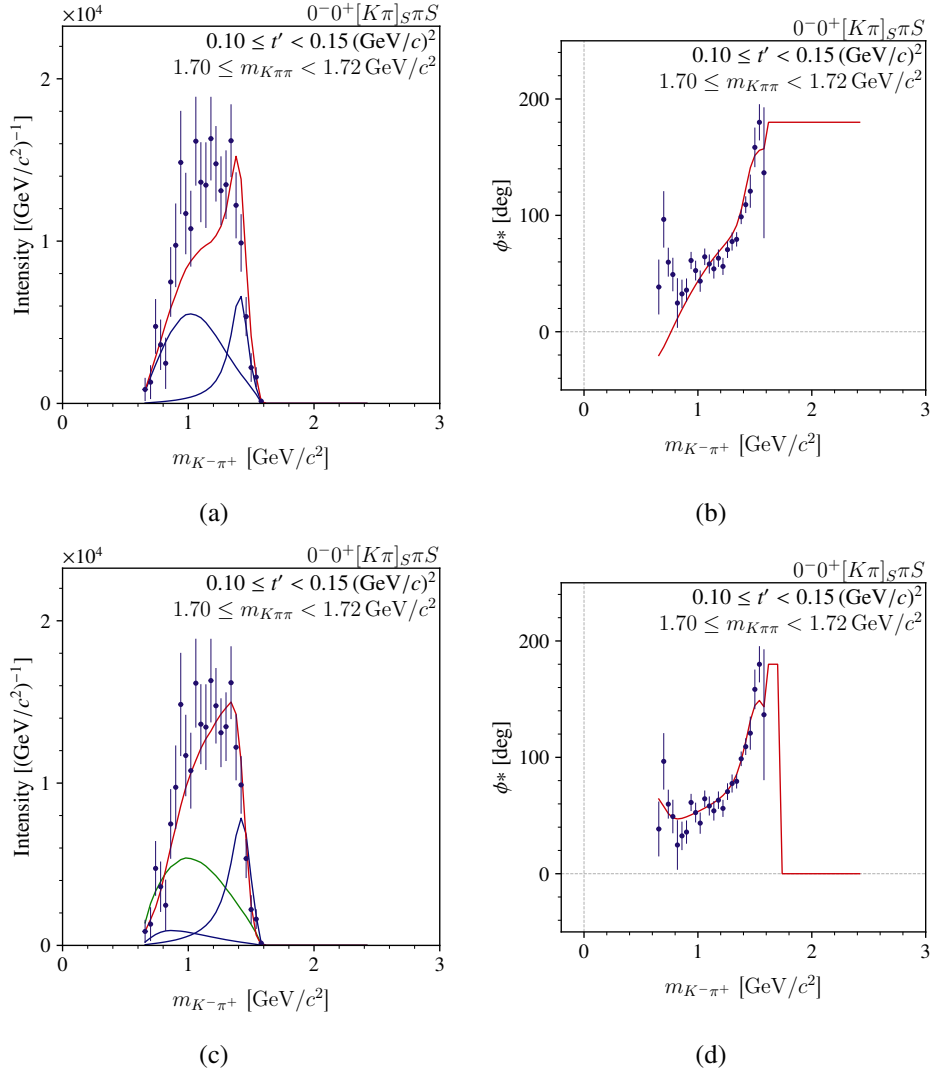
Figure 6.22: Same as fig. 6.1, but for the intensity (left) and phase (right) of the $[K\pi]_S$ amplitude at $m_{K\pi\pi} \approx 1.71\,\mathrm{GeV}/c^2$ in the lowest t'. The top row shows the results of study 4.b. The bottom row shows the results of study 4.d.

phase exhibits two rising phase motions, the main features of which are reproduced by the RMF (see fig. 6.23(b)). In studies 4.f and 4.h, we added a nonresonant component to the RMF. The nonresonant component picks up a large intensity (see fig. 6.23(c)). For $m_{K^-\pi^+} \lesssim 1.1\,\mathrm{GeV}/c^2$, it describes almost all of the measured intensity. There is nearly no contribution from the $K_0^*(700)$ component. With the interference between the nonresonant and Breit-Wigner components, the RMF reproduces the measured intensity spectrum for $m_{K^-\pi^+} \lesssim 1.6\,\mathrm{GeV}/c^2$ better than the RMF without the nonresonant component. However, for $m_{K^-\pi^+} \gtrsim 1.6\,\mathrm{GeV}/c^2$, the RMF with the nonresonant component yields a model curve that is slightly worse. The corresponding

(a)

(b)

(c)

(d)
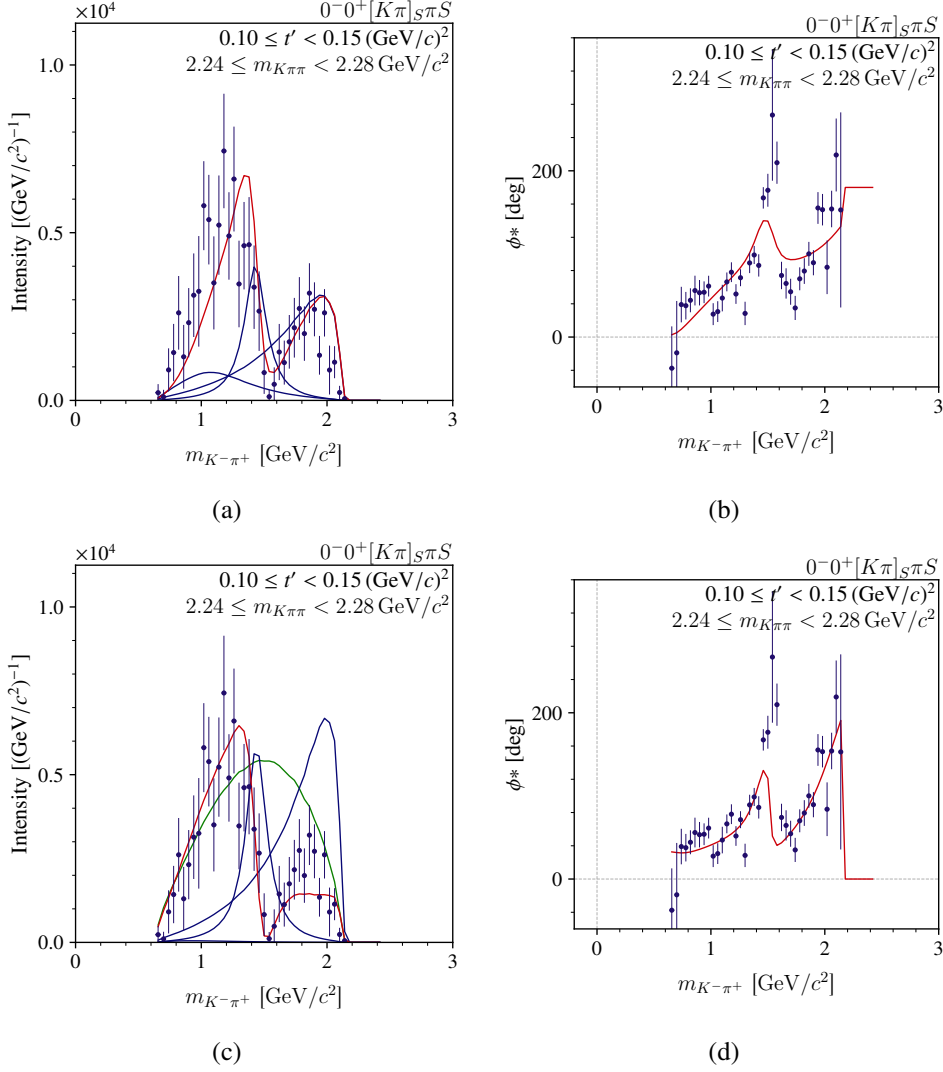
Figure 6.23: Same as fig. 6.1, but for the intensity (left) and phase (right) of the $[K\pi]_S$ amplitude at $m_{K\pi\pi} \approx 2.26\,\mathrm{GeV}/c^2$ in the lowest t' bin. The top row shows the results of study 4.g. The bottom row shows the results of study 4.h.

phase is also well reproduced (see fig. 6.23(d)). Since none of the RMFs in table 6.8 converge and all of them have high interferences between their components, which we do not consider to be physical solutions. Therefore, these models will not be discussed further.

6.4.2 LASS Parameterization

A parameterization specifically constructed for the $[K\pi]_S$ amplitude is the so-called LASS parameterization [37]. This parameterization basically takes a $K_0^*(1430)$ Breit-Wigner compo-

nent and adds an effective-range nonresonant component such that the total amplitude fulfill the
unitarity constraint. The LASS amplitude reads:

$$\mathcal{D}_{Lass}(m_{K^-\pi^+}) = \frac{\sin \delta_B(m_{K^-\pi^+}) e^{i\delta_B(m_{K^-\pi^+})} + \sin \delta_R(m_{K^-\pi^+}) e^{i(\delta_R(m_{K^-\pi^+})+2\delta_B(m_{K^-\pi^+}))}}{\rho(m_{K^-\pi^+})}, \quad (6.4)$$

where $\rho(m) = 2q(m)/m^2$ is the $K\pi$ phase-space with the two-body break-up momentum $q(m)$
(see eq. (3.9)) of the $K\pi$ system. The phases of the resonance δ_R and the effective range
background δ_B read:

$$\tan \delta_R(m) = \frac{m_0\Gamma(m)}{(m_0^2 - m^2)}, \quad \cot \delta_B(m) = \frac{1}{aq(m)} + \frac{rq(m)}{2}. \quad (6.5)$$

The dynamic width $\Gamma(m)$ is defined in eq. (3.8). Figure 6.24 illustrates the intensity as well as
the real and imaginary part of the Lass amplitude.

6.4.2.1 Fixed Parameters

The LASS parameterization was developed to describe the $[K\pi]_S$ amplitude. To see how well the
parameterization performs, a number of RMFs were performed (see table 6.9), where we fixed the
parameters to those taken from ref. [38]. The parameters were measured with LASS scattering
data from ref. [39] and read: $m_{0,\text{fix}} = 1435 \, \text{MeV}/c^2$, $\Gamma_{\text{fix}} = 279 \, \text{MeV}/c^2$, $a_{\text{fix}} = 1.95 \, \text{MeV}/c^2$
and $r_{\text{fix}} = 1.76 \, \text{MeV}/c^2$. First, we tested if the parameterization with fixed parameters can
represent our data. In some $(m_{K\pi\pi}, t')$ cells, the RMF is able to provide an accurate description

(a)   (b)
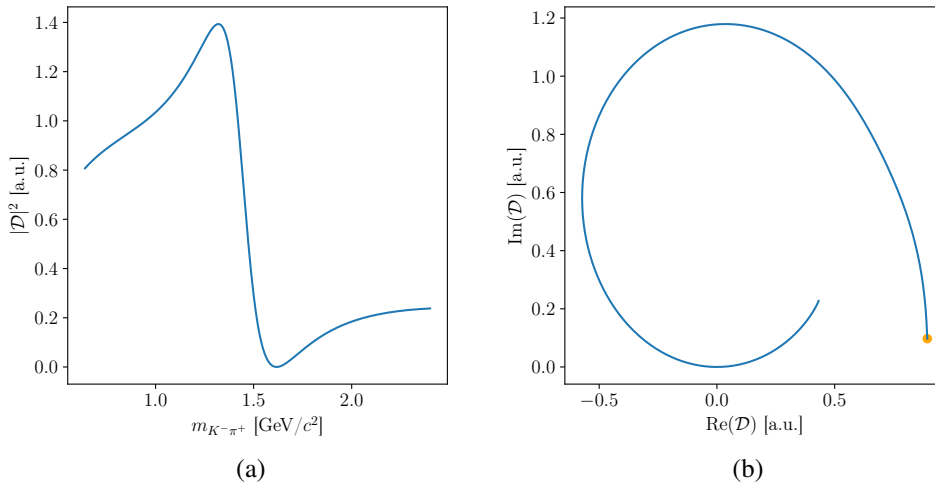
Figure 6.24: Dynamic amplitude of the LASS parameterization. (a) shows the intensity as a
function of $m_{K^-\pi^+}$. (b) shows the Argand diagram, i.e. real vs. imaginary part of
the amplitude. The orange dot corresponds to the point with the lowest $m_{K^-\pi^+}$ in
the intensity plot.

(a)

(b)

(c)

(d)
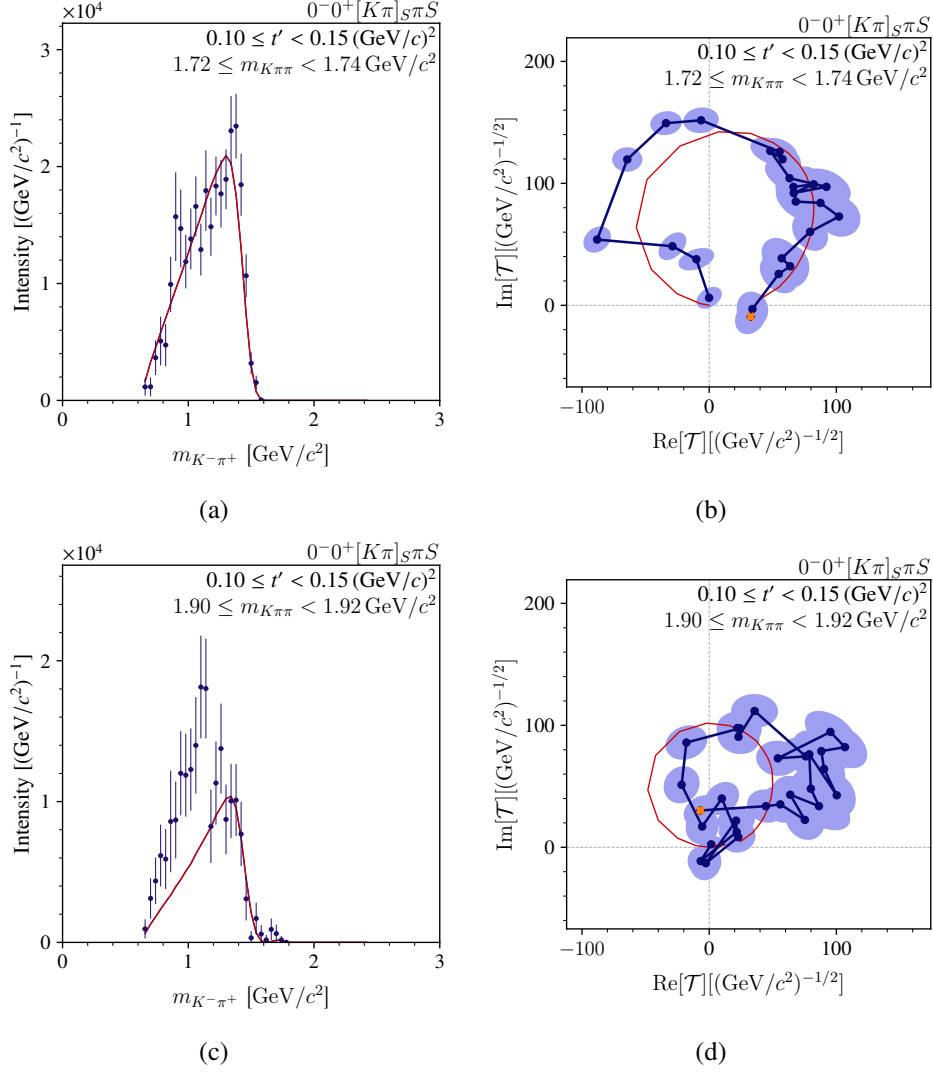
Figure 6.25: Same as fig. 6.9, but for the intensity (left) and Argand (right) of study 4.i of the $[K\pi]_S$ amplitude. The top row shows the results at $m_{K\pi\pi} \approx 1.73\,\mathrm{GeV}/c^2$ in the lowest t' bin. The bottom row shows the results at $m_{K\pi\pi} \approx 1.91\,\mathrm{GeV}/c^2$ in the lowest t' bin.

of the measured intensity spectrum and amplitude (see figs. 6.25(a) and 6.25(b)). In the other approximately 30 ($m_{K\pi\pi}$, t') cells, this is not the case. There, the data exhibit a bump at about $1.0\,\mathrm{GeV}/c^2$, which is not reproduced by the LASS amplitude (see fig. 6.25(c)). In the same ($m_{K\pi\pi}$, t') cells the data in the Argands diagram always exhibit an oval bulge, which correspond to the bump in the data and which are not well reproduced by the RMF (see fig. 6.25(d)). This bulge is not continuous in t' or $m_{K\pi\pi}$. This behavior is very similar to the enhanced intensity in the $[\pi\pi]_P$ amplitude described in section 6.2. We will call this behavior in the $[K\pi]_S$ amplitude

Table 6.9: Same as table 6.1, but for RMFs with the LASS parameterization in $[K\pi]_S$ amplitude. In the fourth row the parameters given in brackets lists the free parameters. If a parameter is not listed, its value was fixed to the value from ref. [38]. Note that in studies 4.k, 4.l and 4.p, all availabe $m_{K^-\pi^+}$ bins in a $m_{K\pi\pi}$ cell are fitted.

	$m_{K\pi\pi}$ range [GeV/c^2]	$m_{K^-\pi^+}$ range [GeV/c^2]	Resonant component	Nonres component	Convergence behavior
study 4.i	{1.6; 2.32}	{0.0; 1.4}	Lass	None	converged
study 4.j	{1.6; 2.32}	{0.0; 1.4}	Lass	free	converged
study 4.k	{1.6; 2.32}	{0.0; 2.4}	Lass 1 Breit-Wigner	None	converged
study 4.l	{1.6; 2.32}	{0.0; 2.4}	Lass 1 Breit-Wigner	free	converged
study 4.m	{1.6; 2.32}	{0.0; 1.4}	Lass(m_0, Γ_0)	None	converged
study 4.n	{1.6; 2.32}	{0.0; 1.4}	Lass(a, r)	None	converged
study 4.o	{1.6; 2.32}	{0.0; 1.4}	Lass(m_0, Γ_0, a)	None	converged
study 4.p	{1.6; 2.32}	{0.0; 2.4}	Lass(m_0, Γ_0, a, r) 1 Breit-Wigner	None	converged

the bulgy amplitude.

Also, we performed RMFs with an additional nonresonant component (studies 4.j and 4.l). The measured intensity spectra are well reproduced in all ($m_{K\pi\pi}$, t') cells (see figs. 6.26(a) and 6.26(c)). The intensity of the nonresonant component is small in ($m_{K\pi\pi}$, t') cells that do not exhibit the bulgy amplitude (see fig. 6.26(a)). In the corresponding Argand diagram, we observe a model curve similar to that in the RMF without the nonresonant component (c.f. figs. 6.25(a) and 6.26(a)). The contribution of the nonresonant component is large in ($m_{K\pi\pi}$, t') cells exhibiting the bulgy amplitude (see fig. 6.26(c)). The total model curve in the corresponding Argand diagram has a non-circular shape that does not perfectly match the shape of the measured amplitude (see fig. 6.26(d)). It appears that the nonresonant component is only used to compensate for the effects of the bulgy amplitude. Thus, the $[K\pi]_S$ amplitude does not have a high background from the nonresonant production of the final-state particles.

To search for a signal of the $K_0^*(1950)$, a Breit-Wigner component with parameters fixed to the PDG average of the $K_0^*(1950)$ was added to the RMF in study 4.k. For $m_{K\pi\pi} \lesssim 2\,\text{GeV}/c^2$ the Breit-Wigner component has a very low intensity and contributes very little to the total model curve (see fig. 6.27(a)). The RMF yielded the same features as the RMFs without the $K_0^*(1950)$ Breit-Wigner component (c.f. fig. 6.27(b)). For $m_{K\pi\pi} \gtrsim 2\,\text{GeV}/c^2$, the $K_0^*(1950)$ Breit-Wigner contributes mainly at about $1.9\,\text{GeV}/c^2$ (see fig. 6.27(c)). The corresponding phase exhibits two rising phase motions at about $1.1\,\text{GeV}/c^2$ and at about $2\,\text{GeV}/c^2$ (see fig. 6.27(d)). The RMF reproduces the main features of the phase rises.

In an addition study 4.l, the RMF with the LASS prameterization and a Breit-Wigner component
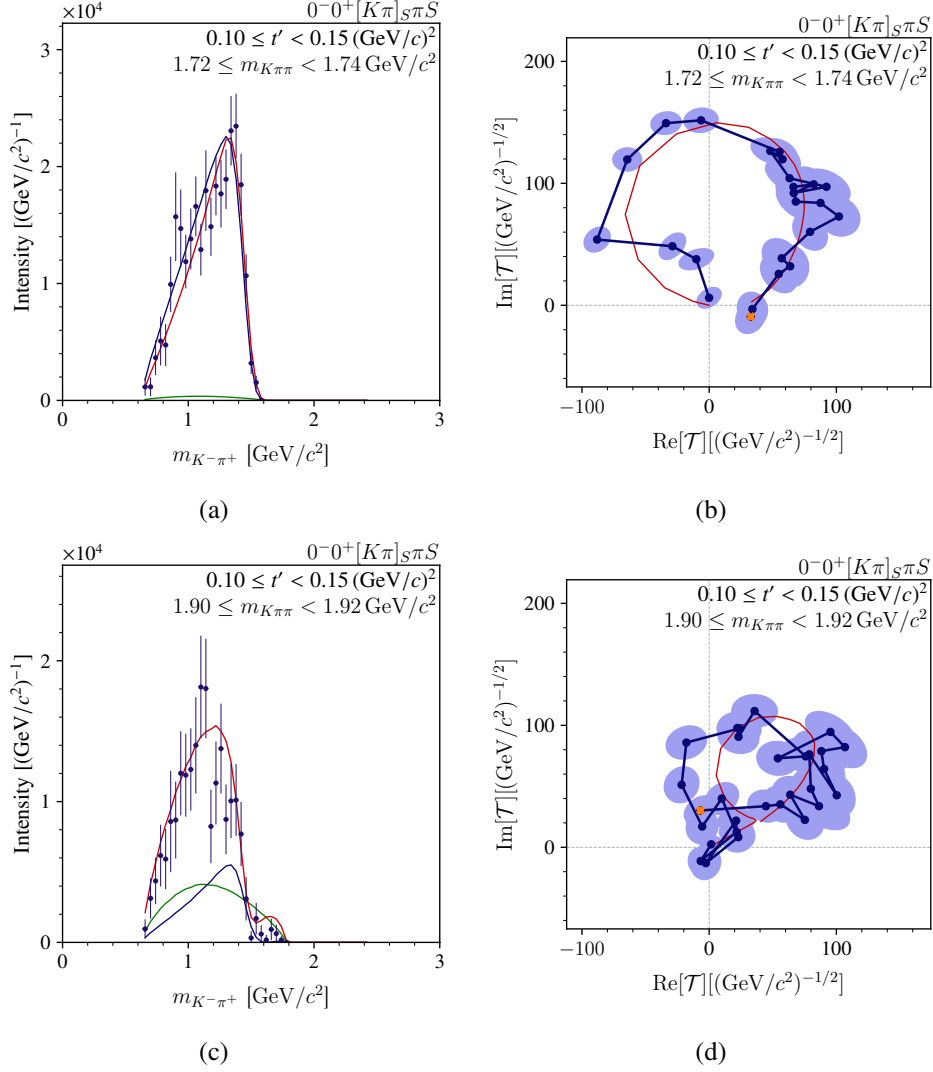
Figure 6.26: Same as in fig. 6.9, but for the intensity (left) and Argand (right) of study 4.j of the $[K\pi]_S$ amplitude. The top row shows the results at $m_{K\pi\pi} \approx 1.73\,\text{GeV}/c^2$ in the lowest t' bin. The bottom row shows the results at $m_{K\pi\pi} \approx 1.91\,\text{GeV}/c^2$ in the lowest t' bin.

with fixed parameters, was repeated with an additional nonresonant component. This study yielded results similar to study 4.j. The intensity spectra in ($m_{K\pi\pi}$, t') cells that do not exhibit the bulgy amplitude, exhibit a small nonresonant contribution. In the ($m_{K\pi\pi}$, t') cells that exhibit the bulgy amplitude, the intensity spectra show a large nonresonant contribution to the total model curve.

Overall, the LASS parameterization yields a shape similar to the measured amplitude. Exceptions are the approximately 30 ($m_{K\pi\pi}$, t') cells that exhibit the bulgy amplitude, where the RMF
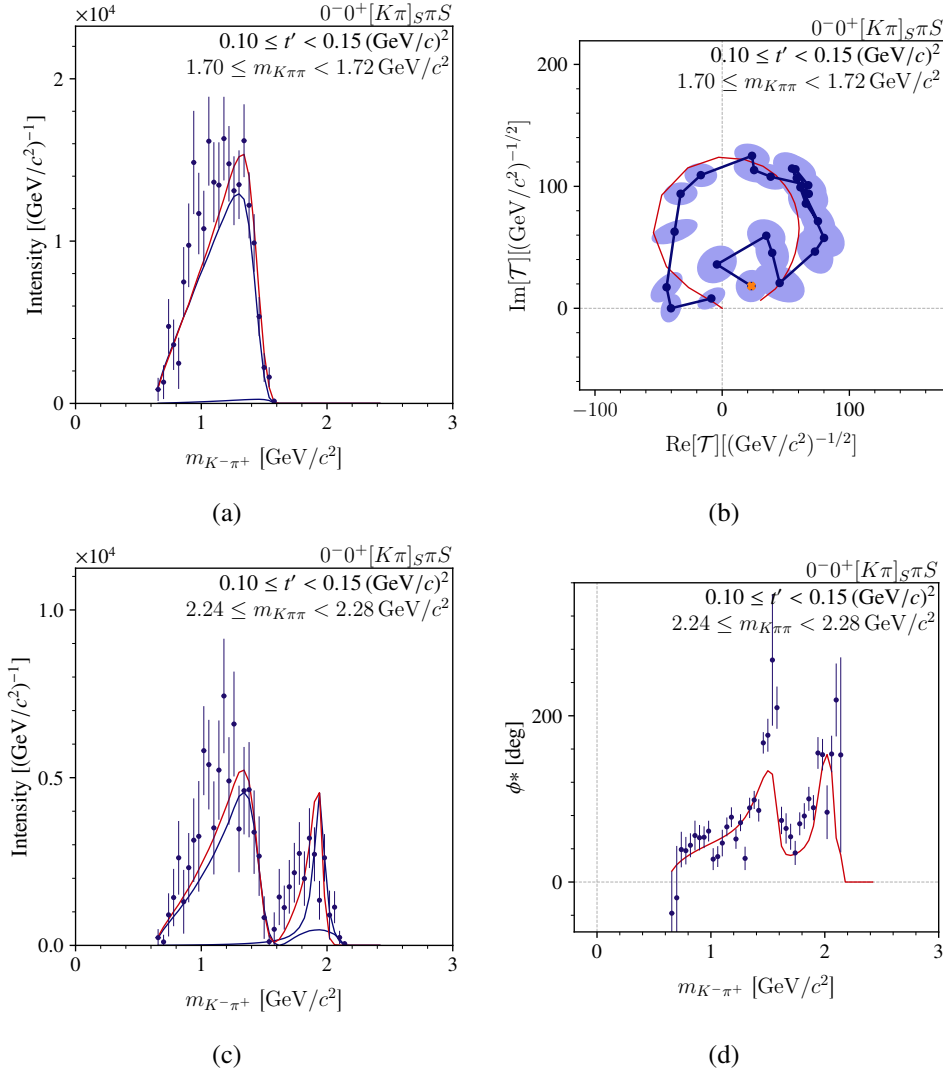
Figure 6.27: Same as fig. 6.9, but for the intensity (left), Argand (top right) and phase (bottom right) of study 4.k of the $[K\pi]_S$ amplitude. The top row shows the results at $m_{K\pi\pi} \approx 1.71\,\text{GeV}/c^2$ in the lowest t' bins. The bottom row shows the results at $m_{K\pi\pi} \approx 2.26\,\text{GeV}/c^2$ in the lowest t' bin.

cannot reproduce the bulge without an additional nonresonant component. The addition of a nonresonant component results in a better described amplitude, but the nonresonant component is only used to correct for the effects by the bulgy amplitude. We do not think that the nonresonant component has any physical meaning, since it has a non-continuous shape in different ($m_{K\pi\pi}$, t') cells and almost no contribution from the nonresonant component is seen in ($m_{K\pi\pi}$, t') cells that do not exhibit the bulgy amplitude. Due to the nonphysicality of the nonresonant component and the bulgy amplitude that is non continuous in t' and $m_{K\pi\pi}$, we

assume that the bulgy amplitude results from an analysis artifact.

6.4.2.2 Free Parameters

All the RMFs discussed in section 6.4.2.1 used the LASS parameterization with fixed parameters from ref. [38]. With these fixed parameters, the LASS parameterization showed a similar shape to the measured amplitude. In studies 4.m to 4.p, some parameters of the LASS parameterization were freed to see if we can measure the parameters as a consistency check. All these studies showed agreement with the data and to their corresponding studies 4.i to 4.l. We have not performed a full set of systematic studies of the parameters of the LASS parameterization, so we will only report the maximum and minimum values we obtained for the parameters. We measured the following values: $1438 \, \text{MeV}/c^2 < m_0 < 1463 \, \text{MeV}/c^2$, $253 \, \text{MeV}/c^2 < \Gamma_0 < 404 \, \text{MeV}/c^2$, $2.05 \, \text{MeV}/c^2 < a < 2.96 \, \text{MeV}/c^2$ and $1.05 \, \text{MeV}/c^2 < r < 1.38 \, \text{MeV}/c^2$. The values we obtained are similar to those obtained in [38]. This confirms the good description of the measured $[K\pi]_S$ amplitude by the LASS parameterization. In order to fully determine the parameters of the LASS parameterization with our data, we must perform a full set of systematic studies of the freed-isobar PWD and the RMFs.

6.4.3 Palano-Pennington Parameterization

Another parameterization to describe the $[K\pi]_S$ amplitude was developed by Palano and Pennington [40]. They determined the parameters of the parameterization from a fit to scattering data from LASS [39], a spectroscpoy experiment at SLAC [41] and BaBar [42]. Due well known typos in the formulas in ref. [40], the corrected formulas from ref. [5] are used. This parameterization accounts for the $K_0^*(700)$, $K_0^*(1430)$ and $K_0^*(1950)$ resonances by describing the scattering amplitudes for the processes $K\pi \rightarrow K\pi$ and $K\eta \rightarrow K\pi$ in terms of a T-matrix. The T-matrix from a two-channel parameterization, with channels $1 = K\pi$ and $2 = K\eta$, is taken from ref. [40]. The T-matrix is parameterized in terms of a K-matrix with elements K_{ij}. The T-matrix elements read:

$$T_{11} = \frac{K_{11} - i\varphi_2^2 \det K}{\delta}, \quad \text{and} \quad T_{21} = T_{12} = \frac{K_{12}}{\delta}. \tag{6.6}$$

Here, $\det K = K_{11}K_{22} - K_{12}^2$, φ_2^i is the two-body phase space for the channel i and

$$\delta = 1 - i\varphi_2^1 K_{11} - i\varphi_2^2 K_{22} - \varphi_2^1 \varphi_2^2 \det K. \tag{6.7}$$

The K-matrix is given by

$$K_{ij} = \frac{(m_{K^-\pi^+}^2 - s_A)}{s_{K\pi}} \left[\sum_{\alpha=a,b} \frac{g_i^\alpha g_j^\alpha}{s_\alpha - m_{K^-\pi^+}^2} + \sum_{n=0}^{3} C_{ij,n} X^n \right], \tag{6.8}$$

which is a sum of the two poles at s_a, s_b and a third-order polynomial in

$$X = \frac{2m_{K^-\pi^+} - (s_{\text{top}} + s_{\text{bot}})}{s_{\text{top}} - s_{\text{bot}}}, \tag{6.9}$$

where $s_A = 0.87753 s_{K\pi}$, $s_{\text{top}} = 5.832\,\text{GeV}^2$ and $s_{\text{bot}} = 0.36\,\text{GeV}^2$ are fixed. The parameter $s_{K\pi} = m_K^2 + m_\pi^2$ is fixed. The amplitudes used in the RMF are:

$$\mathcal{D}_{K\pi \to K\pi}(m_{K^-\pi^+}) = T_{11}(m_{K^-\pi^+}^2) \tag{6.10}$$

$$\mathcal{D}_{K\eta \to K\pi}(m_{K^-\pi^+}) = T_{12}(m_{K^-\pi^+}^2) \tag{6.11}$$

Figure 6.28 illustrates the intensity and real and imaginary part of the Palano-Pennington amplitude.
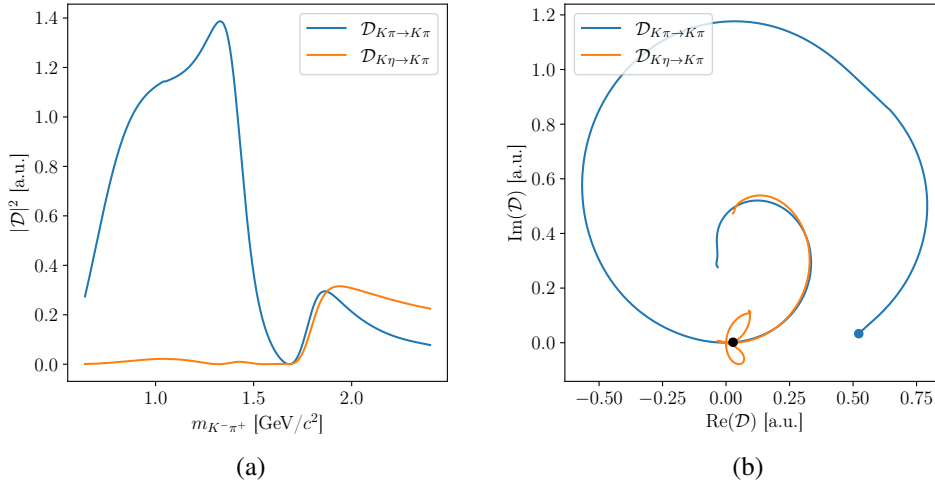
Figure 6.28: Dynamic amplitude of the Palano-Pennington parameterization. (a) shows the intensity as a function of $m_{K^-\pi^+}$. (b) shows the Argand diagram, i.e. real vs. imaginary part of the amplitude. The blue dot corresponds to the point of the $K\pi \to K\pi$ amplitude with the lowest $m_{K^-\pi^+}$ in the intensity plot. The black dot corresponds to the same point of the $K\eta \to K\pi$ amplitude.

Table 6.10: Same as table 6.1 for RMFs with the Palano Pennington parameterization in the $[K\pi]_S$ amplitude. In the fourth row $K\pi$ stands for the component describing $K\pi$ scattering and $K\eta$ stands for the component describing $K\eta$ scattering. Note that in studies 4.t and 4.u, all availabe $m_{K^-\pi^+}$ bins in a $m_{K\pi\pi}$ cell are fitted.

	$m_{K\pi\pi}$ range [GeV/c^2]	$m_{K^-\pi^+}$ range [GeV/c^2]	Resonant component	Nonres component	Convergence behavior
study 4.q	{1.6; 2.32}	{0.0; 1.4}	$K\pi$	None	converged
study 4.r	{1.6; 2.32}	{0.0; 1.4}	$K\pi$ & $K\eta$	None	converged
study 4.s	{1.6; 2.32}	{0.0; 1.4}	$K\pi$	free	converged
study 4.t	{1.6; 2.32}	{0.0; 2.4}	$K\pi$ & $K\eta$	None	converged
study 4.u	{1.6; 2.32}	{0.0; 2.4}	$K\pi$ & $K\eta$	free	converged
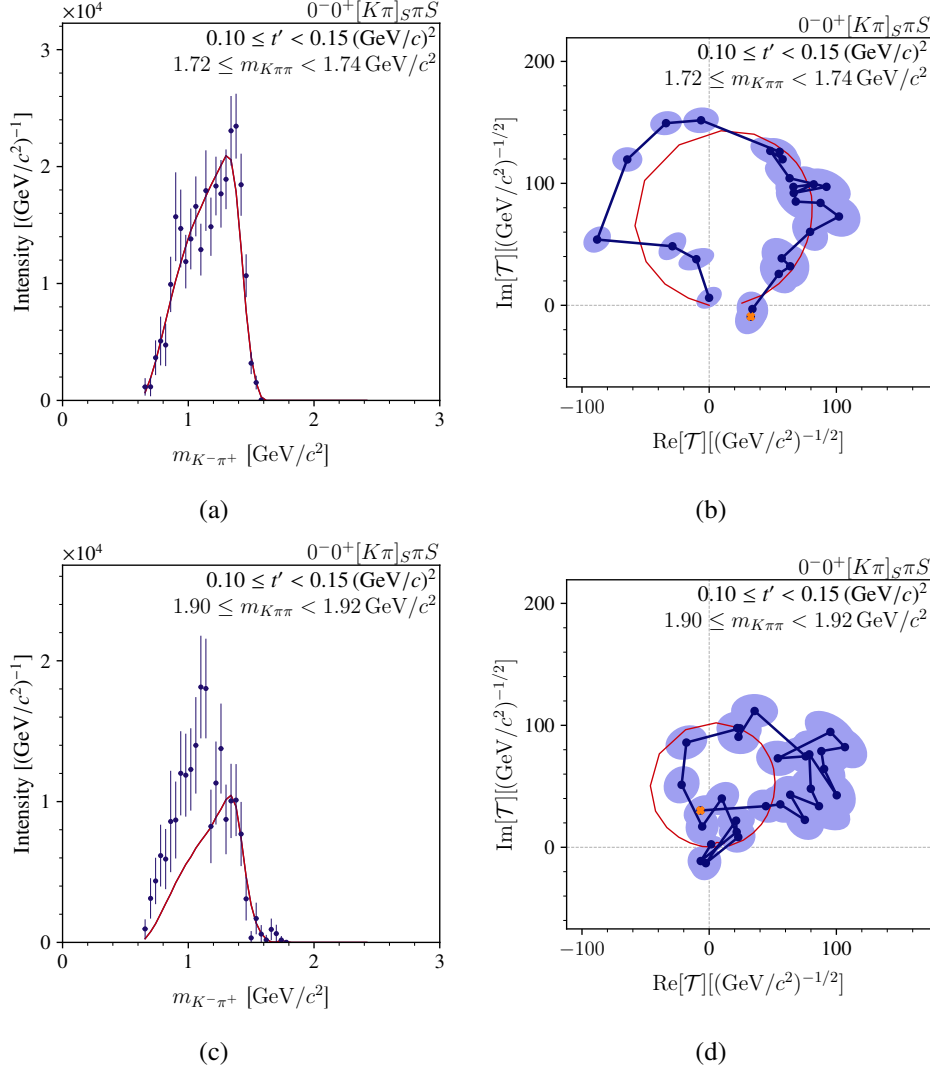
Figure 6.29: Same as fig. 6.9, but for intensity (left) and Argand (right) of the study 4.q of the $[K\pi]_S$ amplitude. The top row shows the results at $m_{K\pi\pi} \approx 1.73\,\text{GeV}/c^2$ in the lowest t' bin. The bottom row shows the results at $m_{K\pi\pi} \approx 1.91\,\text{GeV}/c^2$ in the lowest t' bin.

To better compare the different parameterizations, the same fit ranges are used as in studies 4.i to 4.l (see table 6.8). First, we fitted the mass region $m_{K^-\pi^+} \leq 1.4\,\text{GeV}/c^2$ and used only the $\mathcal{D}_{K\pi\to K\pi}$ amplitude (study 4.q in table 6.10). This RMF shows a similar amplitude shape to the LASS parameterization in study 4.i (c.f. figs. 6.25 and 6.29). Also the Palano-Pennington parameterization cannot describe the bulgy amplitude exhibited in some $(m_{K\pi\pi}, t')$ cells. This indicates again an analysis artifact in the data. In study 4.r, both the $\mathcal{D}_{K\pi\to K\pi}$ and $\mathcal{D}_{K\eta\to K\pi}$ amplitudes are included in an RMF. In intensity spectra of $(m_{K\pi\pi}, t')$ cells that do not exhibit
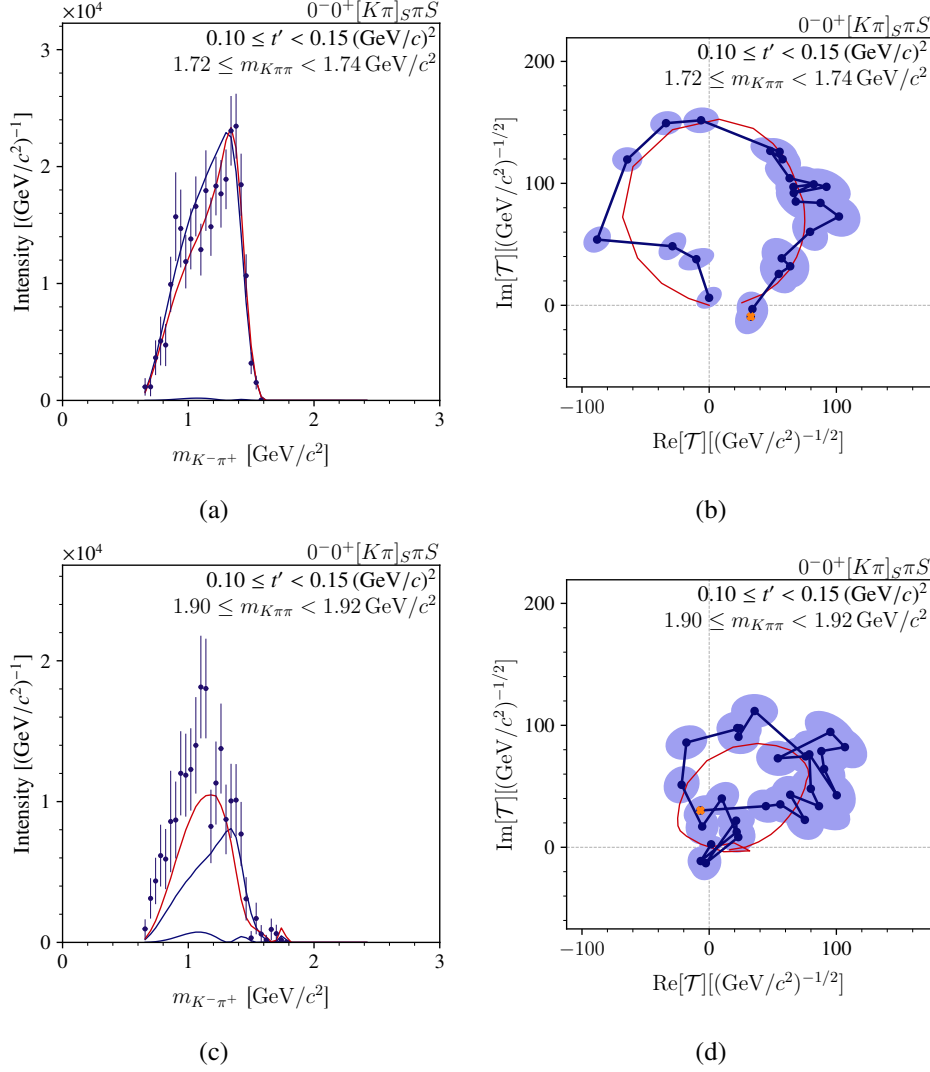
Figure 6.30: Same as fig. 6.9, but for the intensity (left) and Argand (right) of study 4.r in the $[K\pi]_S$ amplitude. The top row shows the results at $m_{K\pi\pi} \approx 1.73\,\text{GeV}/c^2$ in the lowest t' bin. The bottom row shows the results at $m_{K\pi\pi} \approx 1.91\,\text{GeV}/c^2$ in the lowest t' bin.

the bulgy amplitude, the total model curve is similar to that with only the $\mathcal{D}_{K\pi \to K\pi}$ amplitude component (see fig. 6.30(a)). The $\mathcal{D}_{K\eta \to K\pi}$ amplitude contributes only little to the total model curve. The same is true for the Argand diagram (see fig. 6.30(b)). The intensity spectra in $(m_{K\pi\pi}, t')$ cells that exhibit the bulgy amplitude, the total model curve better reproduces the bulge than the RMF without the $\mathcal{D}_{K\eta \to K\pi}$ amplitude (see fig. 6.30(c)). This RMF also shows a very small $\mathcal{D}_{K\eta \to K\pi}$ contribution. The Argand diagram is also better described than in the RMF without the $\mathcal{D}_{K\eta \to K\pi}$ amplitude, since the RMF can now model the oval shape of
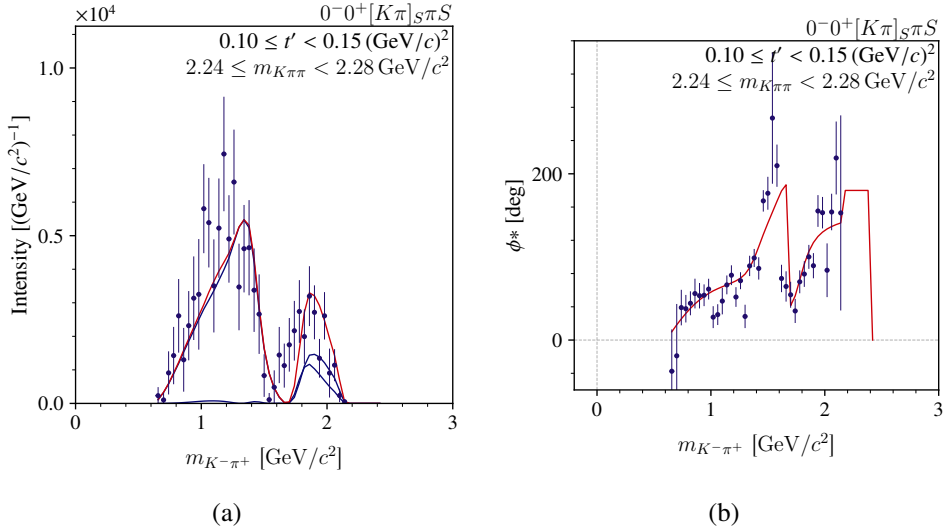
Figure 6.31: Same as fig. 6.1, but for intensity (left) and phase (right) of the $[K\pi]_S$ amplitude at $m_{K\pi\pi} \approx 2.26\,\text{GeV}/c^2$ in the lowest t' bin of study 4.t.

the measured amplitude (see fig. 6.30(d)). The addition of a nonresonant component instead of $\mathcal{D}_{K\eta\to K\pi}$ in study 4.s results in a total model curve similar to that in study 4.j with the LASS parameterization and a nonresonant component (c.f. fig. 6.26). Again, the nonresonant component is used to compensate for effects by the bulgy amplitude. In terms of their reduced χ^2-values, the study 4.s performs the best of the studies 4.q to 4.s.

To check for a possible $K_0^*(1950)$ state, the entire $m_{K^-\pi^+}$ range of the $[K\pi]_S$ amplitude was fit in an RMF with both the $\mathcal{D}_{K\pi\to K\pi}$ and $\mathcal{D}_{K\eta\to K\pi}$ amplitudes (study 4.t). For $m_{K\pi\pi} \lesssim 2.0\,\text{GeV}/c^2$, the intensity spectra and Argand diagram look similar to fig. 6.30, with a small $\mathcal{D}_{K\eta\to K\pi}$ amplitude component contribution. Also study 4.t is unable to describe the bulgy amplitude. For $m_{K\pi\pi} \gtrsim 2.0\,\text{GeV}/c^2$, the data exhibit a peak at about $1.9\,\text{GeV}/c^2$ (see fig. 6.31(a)). Both amplitudes contribute strongly to this region. The measured intensity spectrum is well reproduced by the RMF. The corresponding phase exhibits two rising phase motions at about $1.1\,\text{GeV}/c^2$ and at about $2\,\text{GeV}/c^2$, both well described by the RMF (see fig. 6.31(b)). Overall, the Palano-Pennington parameterization reproduces well the measured $[K\pi]_S$ amplitude.

6.4.4 Pelaez-Rodas Parameterization

The last parameterization we used is taken from an analysis of Pelaez and Rodas [43]. This Pelaez-Rodas parameterization uses conformal mapping functions that parameterizes the data without explicitly modeling the resonance content. Additional constraints were taken into account, such as isospin conservation or elastic unitarity on partial waves. The data used to determine the conformal mapping parameters are measured with scattering data from refs. [39, 41, 44–51], in addition J.R.Pelaez et.al. excluded data points that they consider to be outliers.
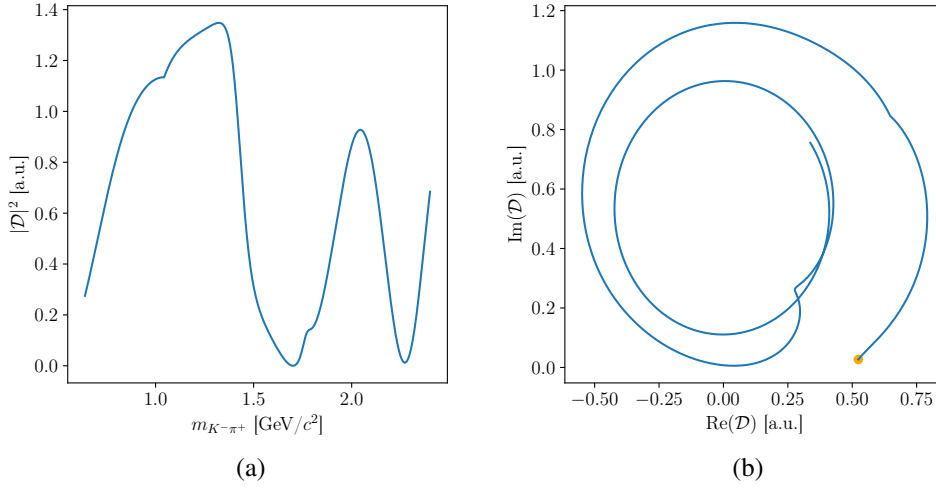
Figure 6.32: Dynamic amplitude of Pelaez-Rodas parameterization. (a) shows the intensity as a function of $m_{K^-\pi^+}$. (b) shows the Argand diagram, i.e. real vs. imaginary part of the amplitude. The orange dot corresponds to the point of the amplitude with the lowest $m_{K^-\pi^+}$ in the intensity plot.

Table 6.11: Same as table 6.1 for RMFs with the Pelaez-Rodas parameterization in the $[K\pi]_S$ amplitude. Note that in studies 4.x to 4.z, all availabe $m_{K^-\pi^+}$ bins in a $m_{K\pi\pi}$ cell are fitted.

	$m_{K\pi\pi}$ range [GeV/c^2]	$m_{K^-\pi^+}$ range [GeV/c^2]	Resonant component	Nonres component	Convergence behavior
study 4.v	{1.6; 2.32}	{0.0; 1.4}	Pelaez-Rodas	None	converged
study 4.w	{1.6; 2.32}	{0.0; 1.4}	Pelaez-Rodas	free	converged
study 4.x	{1.6; 2.32}	{0.0; 2.4}	Pelaez-Rodas 1 Breit-Wigner	None	converged
study 4.y	{1.6; 2.32}	{0.0; 2.4}	Pelaez-Rodas 1 Breit-Wigner	free	converged
study 4.z	{1.6; 2.32}	{0.0; 2.4}	Pelaez-Rodas	None	converged

In our models, we used the Pelaez-Rodas parameterization with parameters from their so-called constraint fit to data (CFD). The amplitude was taken from a look-up table kindly provided by Arkeitz Rodas [52]. Figure 6.32 illustrates the intensity and the real and imaginary parts of the Pelaez-Rodas amplitude.

We conducted a total of five studies that differ in their components and fit ranges (see table 6.11). Overall, the Pelaez-Rodas parameterization gives results very similar to the studies with the LASS and Palano-Pennington parameterization. Hence, we do not give as detailed descriptions
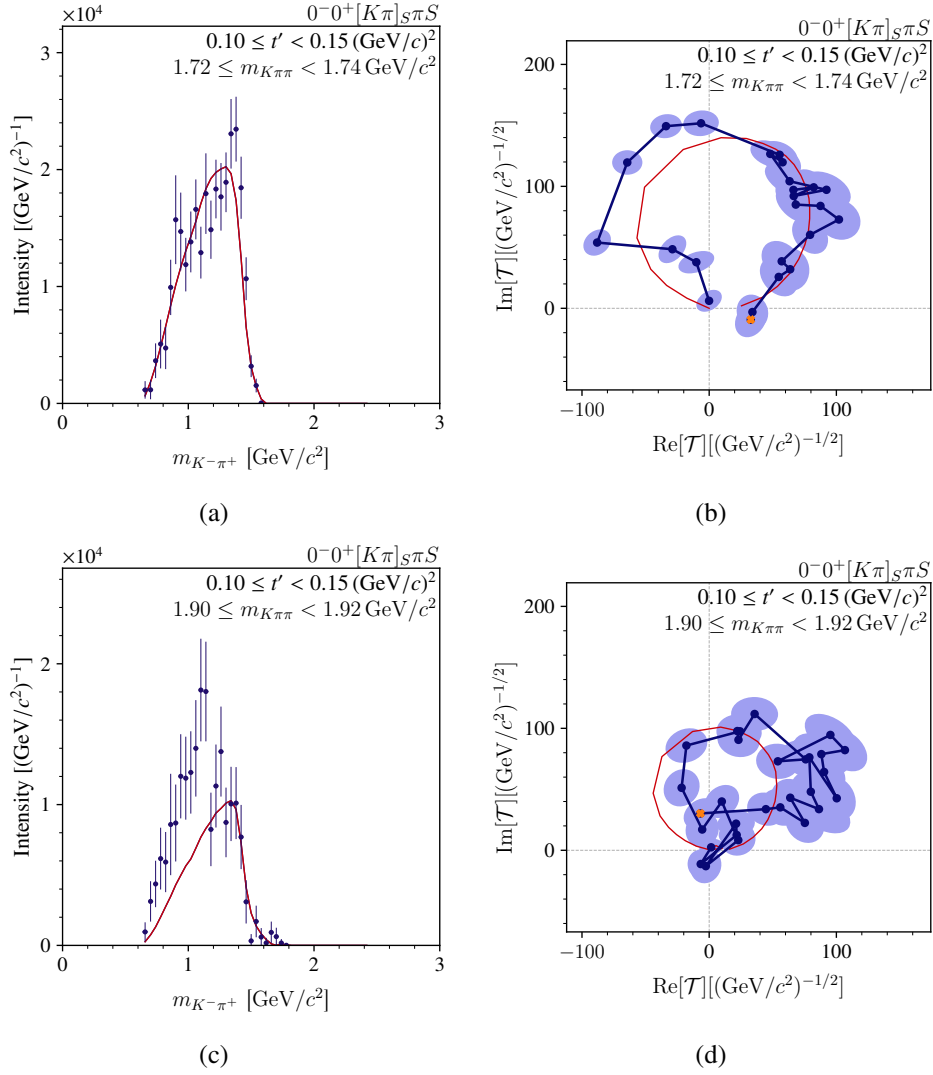
Figure 6.33: Same as fig. 6.9, but for intensity (left) and phase (right) of study 4.v in the $[K\pi]_S$ amplitude. The top row shows the results at $m_{K\pi\pi} \approx 1.73\,\text{GeV}/c^2$ in the lowest t' bin. The bottom row shows the results at $m_{K\pi\pi} \approx 1.91\,\text{GeV}/c^2$ in the lowest t' bin.

as in sections 6.4.2 and 6.4.3, but in study 4.v we test if the Pelaez-Rodas parameterization can describe our measured amplitude. The Pelaez-Rodas parameterization yields a good description of the measured $[K\pi]_S$ amplitude (see fig. 6.33). Also the Pelaez-Rodas parameterization is unable to reproduce well the ($m_{K\pi\pi}$, t') cells that exhibit the bulgy amplitude. Including a nonresonant component in study 4.w yields results similar to studies 4.j and 4.s. In all three studies, the nonresonant component contributes stongly only in ($m_{K\pi\pi}$, t') cells that exhibit the bulgy amplitude and is always used to describe the bulge.
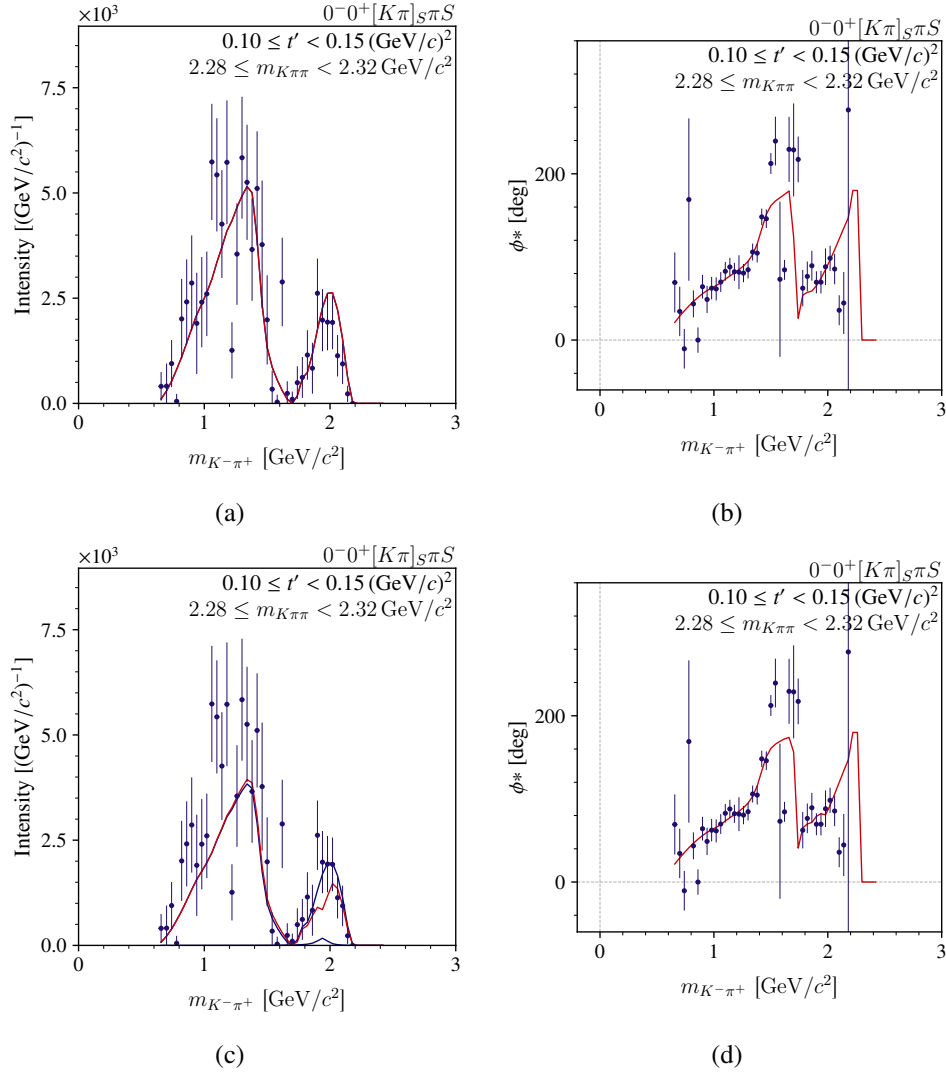
Figure 6.34: Same as fig. 6.9, but for the intensity (left) and Agrand (right) of the $[K\pi]_S$ amplitude at $m_{K\pi\pi} \approx 2.30\,\text{GeV}/c^2$ in the lowest t' bin. The top row shows the results of study 4.z. The bottom row shows the results of study 4.x.

To also study a potential $K_0^*(1950)$ signal in our data, a larger $m_{K^-\pi^+}$ fit range was used in studies 4.x to 4.z. In study 4.z, only the Pelaez-Rodas parameterization is used to model the entire measured amplitude including a possible $K_0^*(1950)$ signal. This study reproduces the structure with the two peaks well (see fig. 6.34(a)). The main features of the two rising phase motions are also reproduced (see fig. 6.34(b)). In study 4.x, where an additional Breit-Wigner component with fixed parameters is added, the intensity spectrum at the $1.9\,\text{GeV}/c^2$ peak is slightly worse reproduced than that without the additonal Breit-Wigner component (see fig. 6.34(c)). The RMF underestimates the intensity in the whole $m_{K^-\pi^+}$ range. The Breit-Wigner component has

a very small overall contribution to the total model. It only appears to make a small contribution to the peak at about $1.9\,\text{GeV}/c^2$. The corresponding phase is modeled similar to the RMF without additional Breit-Wigner component (see fig. 6.34(d)).

6.4.5 Discussion

In total, four different parameterizations of the $[K\pi]_S$ amplitude were tested. The attempts to fit the $[K\pi]_S$ amplitude with the two/three Breit-Wigner components approach failed. Not a single RMF converged, which emphasizes the non-Breit-Wigner like shape of the resonances in the $[K\pi]_S$ amplitude. Therefore, special parameterization for the $[K\pi]_S$ amplitude have been tested. The LASS, Palano-Pennington, and Pelaez-Rodas parameterization all showed similar properties. The $(m_{K\pi\pi}, t')$ cells that exhibit the bulgy amplitude were not well described due to the oval shape of the amplitude. $(m_{K\pi\pi}, t')$ cells that do not exhibit the bulgy amplitude were all well described by the RMFs. When an RMF included a nonresonant component, it was always used to model the bulge in the corresponding $(m_{K\pi\pi}, t')$ cells. $(m_{K\pi\pi}, t')$ cells that do not exhibit the bulgy amplitude, always showed a small nonresonant component contribution. Because of the non-continuous nature of the bulgy amplitude and shape of the nonresonant component, we do not assume that they result from a physical process. Rather, they are remnants of the analysis, i.e. analysis artifacts.

We assume that the analysis artifact is due to a poor description of the $[\pi\pi]_S$ amplitude, similar to the enhanced intensity in section 6.2. The $[\pi\pi]_S$ amplitude contains the $f_0(500)$ resonance, which has similar properties as the $K_0^*(700)$, making it difficult to parameterize. Since the $[\pi\pi]_S$ amplitude may not be very well parameterized in the freed-isobar PWD fit, ambiguities in the $[K\pi]_S$ amplitude may arise from zero-mode-like effects discussed in section 3.3. This is only an assumption and has yet to be confirmed by systematic studies within the freed-isobar PWD fit. If this is the cause of the discontinuous amplitude, then a better parameterization of the $[\pi\pi]_S$ amplitude has to be determined, e.g. by freeing both waves. So far, the three-body analysis parameterizes the $[\pi\pi]_S$ amplitude using the approach of the VES collaboration [21]. With an RMF in the freed-isobar $[\pi\pi]_S$ amplitude potential excited resonances contributing to the $[\pi\pi]_S$ amplitude could be determined. With this information, better parameterizations for the $[\pi\pi]_S$ amplitude could be determined and tested in the RMFs.

Table 6.12 lists a comparison of studies that have the same fit ranges and number of free parameters. This enables a comparison of the χ^2-value within a group of three, because they have the same fit ranges and number of free parameters. For a comparison between the groups, the reduced χ^2-value must be considered as this value is independent of the number of degrees of freedom. Except for the first group, the Palano-Pennington parameterization always performs best. In the first group, where the lower $m_{K^-\pi^+}$ range without an additional nonresonant component was fit, the Pelaez-Rodas amplitude performs slightly better than the Palano-Pennington parameterization. The study that performed best overall is the study 4.s, which consists of the $\mathcal{D}_{K\pi \to K\pi}$ amplitude component of the Palano-Pennington parameterization and a nonresonant component. For a higher range of $m_{K^-\pi^+}$, both the $\mathcal{D}_{K\pi \to K\pi}$ and $\mathcal{D}_{K\eta \to K\pi}$

Table 6.12: Summary of the χ^2-values (third column), reduced χ^2-values (fourth column) and the number of degrees of freedom (fifth column) for specially selected studies (first column) of the $[K\pi]_S$ amplitude. The studies are arranged in groups of three. Each study in the group has the same fit ranges and the same number of free parameters, but different parameterizations, i.e. LASS (see table 6.9), Palano-Pennington (see table 6.10) and Pelaez-Rodas (see table 6.11) parameterization (second column). The last column indicates the used fit range and the whether a nonresonant component was included in the RMF.

	Parameterization	χ^2	reduced χ^2	ndf	Commonality
study 4.i	LASS	8303.99	2.061	4032	
study 4.q	Palano-Pennington	8005.11	1.985	4032	$m_{K^-\pi^+} \leq 1.4\,\text{GeV}/c^2$
study 4.v	Pelaez-Rodas	7984.65	1.980	4032	
study 4.j	LASS	7221.46	1.897	3807	
study 4.s	Palano-Pennington	6891.06	1.810	3807	$m_{K^-\pi^+} \leq 1.4\,\text{GeV}/c^2$, +nonres
study 4.w	Pelaez-Rodas	6892.78	1.811	3807	
study 4.k	LASS	12529.20	2.094	5984	
study 4.t	Palano-Pennington	12505.42	2.090	5984	$m_{K^-\pi^+} \leq 2.4\,\text{GeV}/c^2$
study 4.x	Pelaez-Rodas	12720.46	2.126	5984	
study 4.l	LASS	11377.46	1.976	5759	
study 4.u	Palano-Pennington	11196.24	1.944	5759	$m_{K^-\pi^+} \leq 2.4\,\text{GeV}/c^2$, +nonres
study 4.y	Pelaez-Rodas	11528.54	2.061	5759	

components of the Palano-Pennington parameterization should be considered since it performs best, i.e. has the lowest reduced χ^2-value. This confirms the approch taken in the three-body analysis of this data set, where the Palano-Pennington parameterization was used to model the entire $[K\pi]_S$ amplitude [5].

The goal of the RMFs in the $[K\pi]_S$ amplitude was to test, whether our measurement agrees with previous measurements. Therefore, we tested different parameterizations and determined that the Palano-Pennington performs best in our $[K\pi]_S$ amplitude. However there is another parameterization that decomposes the $K\pi$ Scalar Form Factor (SFF) into individual components, which can be fit to the data, allowing for more flexibility especially in the inelastic region [53]. The first attemps to fit these SFF-basefunctions to our data did not give reliable results. This parameterization will be further investigated.

7 Conclusion and Outlook

In this work, we have analyzed the $[K\pi]_P$, $[\pi\pi]_P$, $[K\pi]_D$ and $[K\pi]_S$ amplitudes measured in the diffractive scattering reaction $K^- + p \rightarrow K^- \pi^- \pi^+ + p$ at the COMPASS experiment.

To this end, we first studied the applicability of Wilks' theorem to the calculation of the significance of a certain RMF component [9]. Formally, the RMFs violate a regularity condition of Wilks' theorem, which makes it inapplicable in principle [28]. We investigated the effect of the violated regularity condition based on the significance calculation. Therefore, we performed Monte Carlo toy studies. The true distributions we obtained from the Monte Carlo toy studies showed shapes similar to the χ^2-distribution assumed using Wilks' theorem. The significance slightly underestimates the true significance. We conclude that Wilks' theorem is a sufficiently good approximation for calculating the significance of components in RMFs. We recommend that Wilks' significance gives about 4σ for an observation and about 6σ for a discovery. We assumed perfectly normally distributed data points, which in nature does not have to be the case. In addition, we only performed toy studies with four t' bins and not with a complete set of $(m_{K\pi\pi}, t')$ cells as in the analysis of the $K^-\pi^+$ and $\pi^-\pi^+$ subsystems. Thus, we cannot give a more definitive answer on the size of the buffer, due to the limitations from our toy studies.

In the $[K\pi]_P$ and $[\pi\pi]_P$ amplitudes, we have found clear peaks of the $K^*(892)$ and $\rho(770)$, respectively. The resonance parameters obtained for the $K^*(892)$ and $\rho(770)$ in our data sample are consistent with previous measurements. Thus, we conclude that the $[K\pi]_P$ and $[\pi\pi]_P$ amplitudes contain a significant $K^*(892)$ and $\rho(770)$ signal, respectively. This also verifies the freed-isobar approach in the $K^-\pi^-\pi^+$ data sample.

In the $[\pi\pi]_P$ amplitude, we compared the Breit-Wigner component with the Gounaris-Sakurai component. Both parameterizations yielded similar shapes and described the $[\pi\pi]_P$ amplitude equally well in terms of their reduced χ^2-values. The resonance parameters obtained with both parameterizations are also very close. We therefore conclude that both parameterizations describe the $[\pi\pi]_P$ amplitude equally well.

The $[K\pi]_D$ amplitude showed a clear peak of the $K_2^*(1430)$. Its measured resonance parameters were very stable and consistent with previous measurements. Thus, we conclude that the $[K\pi]_D$ contains a clear $K_2^*(1430)$ signal. We compared our neutral $K_2^*(1430)^0$ measurement with the charged $K_2^*(1430)^\pm$ measurement of the three-body analysis of the same data sample [35]. Both yielded agreeing masses for the $K_2^*(1430)$ signal. We do not observe the mass difference between the charged and uncharged $K_2^*(1430)$ that the PDG states [2].

In the $[K\pi]_S$ amplitude we tested four different parameterizations. The parameterization with two or three Breit-Wigner components failed to describe the measured $[K\pi]_S$ amplitude. The LASS [37], Palano-Pennington [40], and Pelaez-Rodas [43] parameterizations all showed similar shapes and described the $[K\pi]_S$ amplitude well. We also compared the parameterizations in terms of their reduced χ^2-values. Overall, the Palano-Pennington parameterization performed the best in describing the entire $m_{K^-\pi^+}$ range and the $m_{K^-\pi^+} \leq 1.4\,\text{GeV}/c^2$ range of the $[K\pi]_S$ amplitude. Thus, we conclude that the Palano-Pennington parameterization is the best parameterization for our data sample to model the $[K\pi]_S$ amplitude. This verifies the approach taken in the three-body analysis, where the $[K\pi]_S$ amplitude was modeled by a Palano-Pennington.

In both the $[K\pi]_P$ and $[K\pi]_D$ amplitudes we observed peaks at higher $m_{K^-\pi^+}$ beyond the corresponding ground state. The significance for the components describing these peaks gave values above $20\,\sigma$. Therefore, they are statistically significant. The peak in the $[K\pi]_P$ amplitude could correspond to either the $K^*(1410)$ or $K^*(1680)$. Due to the instability of the results in the performed studies, we cannot assign the peak to either state. The peak in the $[K\pi]_D$ amplitude could correspond to the $n^{2S+1}L_J = 2^3P_2\ K_2^*$ state predicted by quark-model calculations [34]. However, our mass estimate is much smaller than the predicted value. As the systematic uncertainties of the freed-isobar PWD have not yet been determined, we cannot make a definitive statement about the origin of the peaks that do not correspond to the ground states in the $[K\pi]_P$ and $[K\pi]_D$ amplitudes.

Both the $[\pi\pi]_P$ and $[K\pi]_S$ amplitudes showed structures in some $(m_{K\pi\pi}\,,\,t')$ cells that do not have the characteristics of a resonant signal. First of all, these structures do not appear in each $(m_{K\pi\pi}\,,\,t')$ cell and are not continuous in $m_{K\pi\pi}$ and t', i.e. the structures can be observed in one $(m_{K\pi\pi}\,,\,t')$ cell and not in the next one. Second, the shape of the measured amplitude in these $(m_{K\pi\pi}\,,\,t')$ cells is different from the shape of the resonance model. In $(m_{K\pi\pi}\,,\,t')$ cells that do not exhibit these structures, the measured amplitude and the resonance model shape match. This leads us to conclude that this structure appears due to analysis artifacts. The amplitude in the affected $(m_{K\pi\pi}\,,\,t')$ cells show similar deformations as known from zero-modes appearing in other freed-isobar PWDs. An imperfect description of the $[\pi\pi]_S$ amplitude could potentially lead to this type of deformation. Another possible explanation are artifacts due to RICH acceptance effects, which could also lead to these kind of deformations in the amplitudes. We can neither verify nor falsify contributions from either source, so further systematic studies of the freed-isobar PWD are needed to determine the origin of the deformed amplitudes.

Finally, we studied the contributions of nonresonant processes to the amplitude. Around the ground states, the nonresonant component did not contribute strongly to the intensity. We only observed contributions from the nonresonant component that compensated for the potential analysis artifacts discussed above or RMF model imperfections such as the inability of the second Breit-Wigner component to describe the peak of the potential excited resonant state. Thus, we conclude that nonresonant processes do not contribute significantly to the measured

freed-isobar amplitudes.

In summary, the freed-isobar method works in the strange-meson scattering data, as demonstrated by the consistent observation of well-known resonances in the $[K\pi]_P$ and $[\pi\pi]_P$ amplitudes. In the $[K\pi]_P$ and $[K\pi]_D$ amplitudes, we observe indications for excited strange-mesons which are statistically significant. However, it is unclear from which resonance they originate, since the RMFs are not very stable and the systematic uncertainties of the analysis have not yet been determined. The $[\pi\pi]_P$ and $[K\pi]_S$ both showed structures that we attribute to analysis artifacts. We observed only small contributions from nonresonant processes to our data sample.

To determine final results for the freed-isobar amplitudes, systematic uncertainties of the measured resonances must be determined. For this work we just performed a limited amount of systematic studies, thus to determine the full systematic uncertainties of the resonance, a full set of systematic studies of the freed-isobar PWD and the RMFs have to be performed.

To further improve this analysis, methods to handle the analysis artifacts need to be developed. To handle the zero-mode-like effects in the $[\pi\pi]_P$ and $[K\pi]_S$ amplitudes, both the subsystem for the $[\pi\pi]_P$ or $[K\pi]_S$ and the $[\pi\pi]_S$ could be freed simultaneously, which would allow the simultaneous measurement of both amplitudes. In an RMF, an additional parameter could model the possible zero-mode, thus allowing to take into account zero-mode-like effects. The problems caused by RICH acceptance effects could be solved by an approach similar to the one used for the three-body analysis of our data sample, where additional parameters in the PWD modeled these caveats [5].

The successor to the COMPASS experiment at CERN, called AMBER, has started its data-taking campaign in 2023 [54]. Part of a possible upcoming phase-2 of the AMBER experiment will be a high-precision measurement of the strange-meson spectrum. The aim is to obtain about 10 times more strange-meson scattering events than measured by COMPASS. More scattering events will allow further improvement of the analysis techniques used, e.g. more than a single wave could be freed in the freed-isobar analysis. The results will then be less biased by the parameterizations employed for the dynamic amplitudes. Another goal is to improve the final-state particle identification, e.g. by implementing a second RICH detector, which would lead to lower backgrounds. This would allow a much more refined analysis of the strange-meson sector. We have laid the foundation for the analysis of such a data sample from AMBER to improve the understanding of the strange-meson sector, similar to how the results of the $\pi^-\pi^-\pi^+$ data sample have improved the understanding of the non-strange light meson sector [12, 25].

List of Figures

List of Tables

Bibliography

[1] M. Gell-Mann. "A Schematic Model of Baryons and Mesons." In: *Phys. Lett.* 8 (1964), p. 214. DOI: 10.1016/S0031-9163(64)92001-3.

[2] R. L. Workman et al. "Review of Particle Physics." In: *PTEP* 2022 (2022), p. 083C01. DOI: 10.1093/ptep/ptac097.

[3] G. F. Chew and S. C. Frautschi. "Principle of Equivalence for All Strongly Interacting Particles Within the *S* Matrix Framework." In: *Phys. Rev. Lett.* 7 (1961), p. 394. DOI: 10.1103/PhysRevLett.7.394.

[4] M. L. Perl. *High energy hadron physics*. Wiley, 1974. ISBN: 0-471-68049-4.

[5] S. Wallner. "Exploring the Strange-Meson spectrum with COMPASS in the reaction $K^- + p \rightarrow K^- \pi^- \pi^+ + p$." PhD thesis. Munich, Tech. U., 2022.

[6] F. Krinner. "Freed-Isobar Partial-Wave Analysis." Ph.D. thesis. TU München, 2018. URL: https://cds.cern.ch/record/2783415.

[7] F. Krinner, D. Greenwald, D. Ryabchikov, et al. "Ambiguities in model-independent partial-wave analysis." In: *Phys. Rev. D* 97 (2018), p. 114008. DOI: 10.1103/PhysRevD.97.114008.

[8] M. G. Alexeev, G. D. Alexeev, A. Amoroso, et al. "The exotic meson $\pi_1(1600)$ with $J^{PC} = 1^{-+}$ and its decay into $\rho(770)\pi$." In: (2021). arXiv: 2108.01744.

[9] S. S. Wilks. "The Large-Sample Distribution of the Likelihood Ratio for Testing Composite Hypotheses." In: *The Annals of Mathematical Statistics* 9.1 (1938), pp. 60–62. DOI: 10.1214/aoms/1177732360. URL: https://doi.org/10.1214/aoms/1177732360.

[10] P. Abbon, C. Adolph, R. Akhunzyanov, et al. "The COMPASS setup for physics with hadron beams." In: *Nucl. Instrum. Meth. A* 779 (2015), p. 69. DOI: 10.1016/j.nima.2015.01.035.

[11] P. Abbon, E. Albrecht, V. Alexakhin, et al. "The COMPASS experiment at CERN." In: *Nucl. Instrum. Meth. A* 577 (2007), p. 455. DOI: 10.1016/j.nima.2007.03.026.

[12] C. Adolph, R. Akhunzyanov, M. G. Alexeev, et al. "Resonance production and $\pi\pi$ *S*-wave in $\pi^- + p \rightarrow \pi^- \pi^- \pi^+ + p_{\text{recoil}}$ at $190\,\text{GeV}/c$." In: *Phys. Rev. D* 95 (2017), p. 032004. DOI: 10.1103/PhysRevD.95.032004.

[13] P. K. Jasinski. "Analysis of Diffractive Dissociation of K^- into $K^-\pi^+\pi^-$ on a Liquid Hydrogen Target at the COMPASS Spectrometer." Ph.D. thesis. Johannes Gutenberg Universität Mainz, 2012. URL: https://cds.cern.ch/record/1493570.

[14] J. D. Hansen, G. T. Jones, G. Otter, and G. Rudolph. "Formalism and assumptions involved in partial-wave analysis of three-meson systems." In: *Nucl. Phys.* B81 (1974), p. 403. DOI: 10.1016/0550-3213(74)90241-7.

[15] D. Herndon, P. Söding, and R. J. Cashmore. "Generalized isobar model formalism." In: *Phys. Rev. D* 11 (1975), p. 3165. DOI: 10.1103/PhysRevD.11.3165.

[16] B. Ketzer, B. Grube, and D. Ryabchikov. "Light-meson spectroscopy with COMPASS." In: *Prog. Part. Nucl. Phys.* 113 (2020), p. 103755. DOI: 10.1016/j.ppnp.2020.103755.

[17] F. Von Hippel and C. Quigg. "Centrifugal-Barrier Effects in Resonance Partial Decay Widths, Shapes, and Production Amplitudes." In: *Phys. Rev. D* 5 (1972), p. 624. DOI: 10.1103/PhysRevD.5.624.

[18] G. Breit and E. Wigner. "Capture of Slow Neutrons." In: *Phys. Rev.* 49 (1936), p. 519. DOI: 10.1103/PhysRev.49.519.

[19] S. M. Flatté. "On the nature of 0^+ mesons." In: *Phys. Lett. B* 63 (1976), p. 228. DOI: 10.1016/0370-2693(76)90655-9.

[20] M. Ablikim, J. Z. Bai, Y. Ban, et al. "Resonances in $J/\psi \rightarrow \phi\pi^+\pi^-$ and $\phi K^+ K^-$." In: *Phys. Lett. B* 607 (2005), p. 243. DOI: 10.1016/j.physletb.2004.12.041.

[21] Igor A. Kachaev. "Structure of $\pi\pi$ S-wave in $\pi^+\pi^-\pi^-$ system." In: *3rd International Conference on Quarks and Nuclear Physics QNP*. Bloomington, IN, U.S.A., 2004.

[22] K. L. Au, D. Morgan, and M. R. Pennington. "Meson dynamics beyond the quark model: Study of final-state interactions." In: *Phys. Rev. D* 35 (1987), p. 1633. DOI: 10.1103/PhysRevD.35.1633.

[23] N. A. Törnqvist. "Understanding the scalar meson $q\bar{q}$ nonet." In: *Z. Phys. C* 68 (1995), p. 35. DOI: 10.1007/BF01565264.

[24] S. Wallner. "Extraction of Resonance Parameters of Light Meson Resonances in the Charged Three-Pion Final State at the COMPASS Experiment (CERN)." Master thesis. TU München, 2015. URL: https://wwwcompass.cern.ch/compass/publications/theses/2015_dpl_wallner.pdf.

[25] M. Aghasyan, M. G. Alexeev, G. D. Alexeev, et al. "Light isovector resonances in $\pi^- p \rightarrow \pi^-\pi^-\pi^+ p$ at 190 GeV/c." In: *Phys. Rev. D* 98 (2018), p. 092003. DOI: 10.1103/PhysRevD.98.092003.

[26] G. D. Cowan. *Statistical data analysis*. Oxford: Clarendon Press, 1998. ISBN: 0-19-850156-0.

[27] G. Kurten. "Summary of freed-isobar RMF parameter bounds." In: (2023). URL: https://gitlab.cern.ch/compass/hadron/analyses/K_pi_pi/freed_isobar_resonance_model_fits.

[28] R. V. Hogg, J. W. McKean, and A. T. Craig. *Introduction to Mathematical Statistics*. Page 356. Pearson, 2019. ISBN: 9780134686998.

[29] L. Lyons. "Discovering the Significance of 5 sigma." In: (Oct. 2013). arXiv: 1310.1284 [physics.data-an].

[30] G. J. Gounaris and J. J. Sakurai. "Finite width corrections to the vector meson dominance prediction for $\rho \to e^+ e^-$." In: *Phys. Rev. Lett.* 21 (1968), pp. 244–247. DOI: 10.1103/PhysRevLett.21.244.

[31] J. P. Lees et al. "Amplitude Analysis of $B^0 \to K^+ \pi^- \pi^0$ and Evidence of Direct CP Violation in $B \to K^* \pi$ decays." In: *Phys. Rev. D* 83 (2011), p. 112010. DOI: 10.1103/PhysRevD.83.112010. arXiv: 1105.0125 [hep-ex].

[32] R. Barate et al. "Measurement of the spectral functions of vector current hadronic tau decays." In: *Z. Phys. C* 76 (1997), pp. 15–33. DOI: 10.1007/s002880050523.

[33] M. Bartl. *Discussion on zero modes*. Private communication. 2023.

[34] D. Ebert, R. N. Faustov, and V. O. Galkin. "Mass spectra and Regge trajectories of light mesons in the relativistic quark model." In: *Phys. Rev. D* 79 (2009), p. 114029. DOI: 10.1103/PhysRevD.79.114029.

[35] S. Wallner. "Partial-Wave Analysis of the Reaction $K^- + p \to K^- \pi^- \pi^+ + p$." In: *COMPASS Release Note* (2023).

[36] J. R. Pelaez and A. Rodas. "Dispersive $\pi K \to \pi K$ and $\pi \pi \to K \bar{K}$ amplitudes from scattering data, threshold parameters, and the lightest strange resonance κ or $K_0^*(700)$." In: *Phys. Rept.* 969 (2022), pp. 1–126. DOI: 10.1016/j.physrep.2022.03.004. arXiv: 2010.11222 [hep-ph].

[37] A. J. Bevan, B. Golob, T. Mannel, et al. "The Physics of the B Factories." In: *Eur. Phys. J. C* 74 (2014), p. 3026. DOI: 10.1140/epjc/s10052-014-3026-9.

[38] W. M. Dunwoodie. "Fits to K pi I=1/2 S-wave Amplitude and Phase Data." In: (2013). (visited on November 14, 2023). URL: https://www.slac.stanford.edu/~wmd/kpi_swave/kpi_swave_fit.note.

[39] D. Aston, N. Awaji, T. Bienz, et al. "A study of $K^- \pi^+$ scattering in the reaction $K^- p \to K^- \pi^+ n$ at 11 GeV/c." In: *Nucl. Phys. B* 296 (1988), p. 493. DOI: 10.1016/0550-3213(88)90028-4.

[40] A. Palano and M. R. Pennington. "$K\pi$ $I = 1/2$ S-wave from η_c decay data at BaBar and classic Meson-Meson scattering from LASS." In: (2017). arXiv: 1701.04881.

[41] P. Estabrooks, R. Carnegie, A. Martin, et al. "Study of $K\pi$ scattering using the reactions $K^\pm p \to K^\pm \pi^+ n$ and $K^\pm p \to K^\pm \pi^- \Delta^{++}$ at 13 GeV/c." In: *Nucl. Phys. B* 133 (1978), p. 490. DOI: 10.1016/0550-3213(78)90238-9.

[42] J. P. Lees, V. Poireau, V. Tisserand, et al. "Measurement of the $I = 1/2$ $K\pi$ S-wave amplitude from Dalitz plot analysis of $\eta_c \to K \bar{K} \pi$ in two-photon interaction." In: *Phys. Rev. D* 93 (2016), p. 012005. DOI: 10.1103/PhysRevD.93.012005.

[43] J. R. Peláez and A. Rodas. "Determination of the Lightest Strange Resonance $K_0^*(700)$ or κ, from a Dispersive Data Analysis." In: *Phys. Rev. Lett.* 124 (2020), p. 172001. DOI: 10.1103/PhysRevLett.124.172001.

[44] E. M. Aitala et al. "Model independent measurement of S-wave $K^-\pi^+$ systems using $D^+ \rightarrow K\pi\pi$ decays from Fermilab E791." In: *Phys. Rev. D* 73 (2006). [Erratum: Phys.Rev.D 74, 059901 (2006)], p. 032004. DOI: 10.1103/PhysRevD.73.032004. arXiv: hep-ex/0507099.

[45] J. M. Link et al. "The $K^-\pi^+$ S-wave from the $D^+ \rightarrow K^-\pi^+\pi^+$ decay." In: *Phys. Lett. B* 681 (2009), pp. 14–21. DOI: 10.1016/j.physletb.2009.09.057. arXiv: 0905.4846 [hep-ex].

[46] O. Dumbrajs, R. Koch, H. Pilkuhn, et al. "Compilation of Coupling Constants and Low-Energy Parameters. 1982 Edition." In: *Nucl. Phys. B* 216 (1983), pp. 277–335. DOI: 10.1016/0550-3213(83)90288-2.

[47] M. Ablikim et al. "Study of $D^+ \rightarrow K^-\pi^+e^+\nu_e$." In: *Phys. Rev. D* 94.3 (2016), p. 032001. DOI: 10.1103/PhysRevD.94.032001. arXiv: 1512.08627 [hep-ex].

[48] P. del Amo Sanchez et al. "Analysis of the $D^+ \rightarrow K^-\pi^+e^+\nu_e$ decay channel." In: *Phys. Rev. D* 83 (2011), p. 072001. DOI: 10.1103/PhysRevD.83.072001. arXiv: 1012.1810 [hep-ex].

[49] J. M. Link et al. "Dalitz plot analysis of the $D^+ \rightarrow K^-\pi^+\pi^+$ decay in the FOCUS experiment." In: *Phys. Lett. B* 653 (2007), pp. 1–11. DOI: 10.1016/j.physletb.2007.06.070. arXiv: 0705.2248 [hep-ex].

[50] G. Bonvicini, D. Cinabro, M. Dubrovin, et al. "Dalitz plot analysis of the $D^+ \rightarrow K^-\pi^+\pi^+$ decay." In: *Phys. Rev. D* 78 (2008), p. 052001. DOI: 10.1103/PhysRevD.78.052001.

[51] J. P. Lees et al. "Measurement of the I=1/2 $K\pi$ $\mathcal{S}$-wave amplitude from Dalitz plot analyses of $\eta_c \rightarrow K\bar{K}\pi$ in two-photon interactions." In: *Phys. Rev. D* 93 (2016), p. 012005. DOI: 10.1103/PhysRevD.93.012005. arXiv: 1511.02310 [hep-ex].

[52] A. Rodas. *Look-up table for Pelaez-Rodas parameterization*. Private communication. 2023.

[53] L. Von Detten, F. Noël, C. Hanhart, et al. "On the scalar πK form factor beyond the elastic region." In: *Eur. Phys. J. C* 81.5 (2021), p. 420. DOI: 10.1140/epjc/s10052-021-09169-7. arXiv: 2103.01966 [hep-ph].

[54] B. Adams, C. A. Aidala, G. D. Alexeev, et al. "COMPASS++/AMBER: Proposal for Measurements at the M2 beam line of the CERN SPS Phase-1: 2022-2024." In: (2019). URL: https://cds.cern.ch/record/2676885.